Fundamentals of nonlinear interferometers and its use for optical coherence tomography

by

Gerard Jiménez Machado

submitted for the degree of
Doctor of Philosophy

Thesis Advisor: Prof. Dr. Juan P. Torres

ICFO - THE INSTITUTE OF PHOTONIC SCIENCES
UPC - UNIVERSITAT POLITÈCNICA DE CATALUNYA

Barcelona, September 2022

To my family

ACKNOWLEDGMENTS

I would like to thank the following people:

To begin with, let me express my sincere gratitude to Juan. Since he gave me the chance to complete my bachelor thesis in his laboratory at ICFO six years ago, he has been somewhat akin to my scientist father. Since then, with his help, my professional career has been characterized by a continuous process in which I was able to finish the master's degree while working in the lab and now the PhD. Beyond the professional, however, what I am left with is the personal development and education that have been provided to me every day by one of the most modest and cultured people I have ever met.

Secondly, I would like to thank my colleagues and friends at ICFO for all the conversations, discussions, help, laughter and shared moments. I had the good fortune to be surrounded by some of the smartest and nicest people I've ever met, each with their own unique background and life story. Special thanks to Adam, for passing on his endless experimental knowledge to me in my early days and months at ICFO. Without a doubt, that know-how and method have accompanied me and will accompany me in any laboratory I step on. I also want to dedicate a special mention to all ICFO departments, from maintenance, logistics, human resources, mechanical and electronic workshops, purchasing, cafeteria to reception staff, for selflessly making this institution great and making life so much easier.

I also want to dedicate a few words to the colleagues of the Max Planck Institute in Erlangen, who welcomed me as one more from the first day and during the three months that I shared with them. Particularly to Masha, for giving me the opportunity to work and learn in her laboratory, and to Gaetano for his tireless support, help and knowledge that he gave me during my stay. Also a special thanks to Tomás, Andrea, Tobias and Cameron for the shared moments and for making me feel at home despite being away from it.

For the end I want to reserve my thanks to my family and friends. His existence and affection has been key to disconnect and recharge batteries when I have needed it most. Thanks to my parents for all the love and advice they have given me, they are without a doubt my greatest source of inspiration on how to live happily, be grateful for the positive aspects of life and learn from the not so good ones. Also thanks to those who are not here, because I keep you very present and remind me that there is only one life. And finally, my thanks to the most special and brilliant person I know. Mireia, I am very clear that all this would not have been possible without you, you have been my support and life advisor in the most complicated moments. *T'estimo molt, gràcies!*

ABSTRACT

This thesis, mostly experimental, is based on two fundamental pillars: nonlinear interferometers and Optical Coherence Tomography (OCT). Nonlinear interferometers are a class of interferometers that exhibit nonclassical phenomena brought on by nonlinear elements, such as optical parametric amplifiers and parametric down-conversion (PDC) nonlinear crystals. OCT is a non-invasive imaging technique that allows to obtain images with high axial and cross-sectional resolution of a wide variety of samples.

The first novel contribution of this thesis is an experimental scheme that combines the two ideas: an OCT scheme based on a nonlinear interferometer. In these new approach the reflectivity of the sample translates in a loss of first-order coherence between two beams, that is the variable that is measured. In addition, it allows probing the sample with a wavelength different from the one that is measured. In this way, the penetration depth in the sample can be enhanced using longer wavelengths while using light at the optimal wavelength for detection.

We present and implement two different experimental configurations. The first is a nonlinear interferometer based on induced coherence, or *Mandel-type* interferometer, that works in the low parametric gain regime of parametric down-conversion (PDC). The results presented here are a proof-of-concept, that can potentially offer new ap-

plications for OCT, but that are not meant to substitute traditional OCT systems.

The second OCT scheme overcomes some of the limitations of the first scheme discussed above. It is an SU(1,1), or *Yurke-type* interferometer, that operates in the high parametric gain regime of parametric down-conversion. In addition to taking advantage of the salutary features of this new approach, it also enables obtaining values of power and axial resolution comparable to those of conventional OCT.

The second novel contribution of this thesis is related to fundamental aspects at the heart of nonlinear interferometers. We discuss two experiments that study two important concepts behind the idea of induced coherence: quantum distinguishability and parametric amplification (stimulated emission). In the first experiment we propose a new experimental measure of quantum distinguishability and derive a complementarity relation between distinguishability and first-order coherence. In the second experiment, we contribute to the ongoing debate about the *true* role of quantum distinguishability and stimulated emission in explaining the induced coherence effect.

Finally, we put forward theoretically a new scheme to retrieve transverse spatial information of a sample using a nonlinear interferometer, based on projecting the outgoing photons in selected spatial modes. We call this new proposal *spatial spectroscopy*, and it does not require a physical mechanical scan of the sample. We demonstrate the feasibility of the technique with a simple example. This last contribution constitutes a future proposal to be carried out with nonlinear interferometers, evidencing their great versatility and potential applications in new areas.

RESUM

Aquesta tesi, majoritàriament experimental, està basada en dos pilars fonamentals: els interferòmetres nolineals i la Tomografia de Coherència Òptica (OCT). Els interferòmetres nolineals són un tipus d'interferòmetres en els que tenen lloc fenòmens no-clàssics generats per la presència d'elements nolineals, com amplificadors òptics paramètrics i cristalls de conversió paramètrica descendent. OCT és una tècnica interferomètrica no-invasiva per obtenir imatges 3D amb alta resolució axial d'una gran varietat de mostres.

La primera contribució original d'aquesta tesi és un esquema experimental que combina dues idees: un esquema d'OCT basat en un interferòmetre nolineal. En aquesta nova proposta, la reflectivitat de la mostra es tradueix en una pèrdua de coherència entre dos feixos de llum, que és la quantitat mesurada. A més a més, permet il·luminar la mostra amb una longitud d'ona diferent a la mesurada. D'aquesta manera, podem guanyar penetració a la mostra mentre utilitzem llum a la longitud d'ona òptima per la detecció.

En aquest sentit, presentem i implementem dues configuracions experimentals diferents. La primera es tracta d'un interferòmetre nolineal basat en el concepte de coherència induïda, o també anomenat interferòmetre de Mandel, que opera en el règim de baix guany de conversió paramètrica descendent. Els resultats presentats constitueixen una prova del principi de funcionament, que poden su-

posar noves aplicacions per OCT, però no estan enfocats a substituir els sistemes convencionals d'OCT.

El segon esquema d'OCT que proposem millora algunes de les limitacions de l'anterior proposta. Es tracta d'un SU(1,1), o interferòmetre de Yurke, que opera en el règim d'alt guany de conversió paramètrica descendent. A més d'aprofitar les característiques beneficioses d'aquests nous esquemes, també permet obtenir valors de potència i resolució axial comparables als dels sistemes d'OCT tradicionals.

La segona contribució original d'aquesta tesi està relacionada amb aspectes fonamentals que estan rere els interferòmetres nolineals. Presentem dos experiments que estudien dos conceptes importants que expliquen la idea de coherència induïda: la distingibilitat quàntica i l'amplificació paramètrica (o emissió estimulada). En el primer experiment proposem una nova mesura de la distingibilitat quàntica i derivem una relació entre la distingibilitat i la coherència. En el segon experiment, contribuïm al debat vigent sobre el rol de la distingibilitat quàntica i l'emissió estimulada per explicar el concepte de la coherència induïda.

Finalment, presentem les bases teòriques d'un nou esquema per obtenir informació espacial d'una mostra utilitzant un interferòmetre nolineal, basat en la projecció dels fotons en uns modes espacials de llum concrets. Anomenen aquesta nova proposta *espectroscòpia espacial*, i no requereix un escaneig físic-mecànic de la mostra. Demostrem la viabilitat de la tècnica amb un exemple senzill. Aquesta última contribució constitueix una proposta de futur a realitzar amb els interferòmetres nolineals, evidenciant la seva gran versatilitat i potencials aplicacions en noves àrees.

LIST OF PUBLICATIONS

Here it follows a list of publications made during my PhD. Most of the topics covered in this thesis can be found in these papers:

- A. Vallés, **G. J. Machado**, L. J. Salazar-Serrano, and J. P. Torres, "Optical sectioning in induced coherence tomography with frequency-entangled photons", *Phys. Rev. A* ***97***, p. 023824, 2018.

- E. Pisanty, **G. J. Machado**, V. Vicuña-Hernández, A. Picón, A. Celi, J. P. Torres and M. Lewenstein, "Knotting fractional-order knots with the polarization state of light", *Nature Photonics* ***13***, p. 569, 2019.

- **G. J. Machado**, G. Frascella, J. P. Torres and M. V. Chekhova, "Optical Coherence Tomography with a nonlinear interferometer in the high parametric gain regime", *Appl. Phys. Lett.* ***117***, p. 094002, 2020.

- A. Rojas-Santana, **G. J. Machado**, D. Lopez-Mago and J. P. Torres, "Frequency-correlation requirements on the biphoton wave function in an induced coherence experiment between separate sources", *Phys. Rev. A* ***102***, p. 053711, 2020.

- A. Rojas-Santana, **G. J. Machado**, M. V. Chekhova, D. Lopez-Mago and J. P. Torres, "Analysis of the signal measured in spectral-domain optical coherence tomography based on nonlinear interferometers", *Phys. Rev. A* ***106***, p. 033702, 2022.

- **G. J. Machado**, L. Sendra and J. P. Torres, "Complementarity relationship between distinguishability and first-order coherence in a nonlinear interferometer based on induced coherence", *in preparation*, 2022.

- **G. J. Machado**, D. F. Urrego and J. P. Torres, "Revisiting different explanations of the origin of induced coherence in a nonlinear interferometer", *in preparation*, 2022.

- D. F. Urrego, **G. J. Machado**, and J. P. Torres, "Mechanical-scan free optical coherence tomography based on the use of spatial light modulators", *in preparation*, 2022.

- **G. J. Machado** and J. P. Torres, "Spatial spectrosocopy based on a nonlinear interferometer", *in preparation*, 2022.

CONTENTS

CONTENTS

CONTENTS

LIST OF FIGURES

List of Figures

CHAPTER

ONE

INTRODUCTION

Optical interferometers superimpose two light beams in order to measure a phase shift. In many cases, the sought-after phase shift can be retrieved measuring the intensity at one output port of the interferometer, or the difference of intensities between the two output ports of the interferometer. In this way we can estimate the value of a variable of interest, such as path difference, refractive index of a medium or surface irregularities, since the phase shift generated depends on any of these variables.

One interferometer of paramount importance was built by Michelson and Morley in 1887 [1], giving its name to what is now known as the Michelson interferometer. Since its invention, it has become a powerful tool that have found numerous applications in metrology, sensing, spectroscopy and gravitational wave detection. The Michelson interferometer is of special relevance for this thesis, since it is at the heart of Optical Coherence Tomography (OCT). Introduced in 1991 [2, 3], OCT is a widely-used 3D imaging technique that allows cross-sectional and high-resolution tomographic imaging of samples by measuring light reflected back from it. It is a mature technique that finds applications in many areas of science and technology, from

medicine [4] to art conservation studies [5, 6].

The object of study of this thesis are the so-called *nonlinear interferometers*: interferometers that contain light-generating nonlinear elements, such as optical parametric amplifiers and parametric down-conversion (PDC) nonlinear crystals [7]. These schemes were first devised in the late 1980s and were shown to improve phase sensitivity below the shot-noise limit [8].

The novelty of the work presented in this thesis is twofold. First, we demonstrate that nonlinear interferometers can be used to perform OCT measurements. Two experimental OCT realizations are presented, which differ in their basic geometry, and most important, they operate in different gain regimes of parametric down-conversion (PDC). It should be said that the results presented in this thesis do not compete in terms of performance with conventional OCT systems. The objective is to explore and lay the foundations for this novel proposal, and highlight potential advantages and disadvantages of using nonlinear interferometers when compared with OCT schemes based on standard Michelson interferometers.

Secondly, we study some fundamental physical concepts that are at the heart of the nonlinear interferometers explored in this thesis. Specifically, we revisit with new experiments and ideas the concept of *induced coherence*, which was introduced the same year as OCT [9]. Thus, experimental results are presented that shed light on the concepts of path distinguishability and parametric amplification in schemes of this type.

In the final chapter, we present the theoretical foundation for performing spatial spectroscopy with nonlinear interferometers as a potential future application. We call *spatial spectroscopy* a scheme aimed at obtaining spatial information of a sample, spatial features of its shape. The key ingredient is the projection in conveniently selected spatial modes of light, which avoid the need to physically scan the sample transversely. Furthermore, this scheme benefits from the salutary features of nonlinear interferometers: retrieving information by detecting photons that never interacted with the sample.

The use of nonlinear interferometers for imaging, sensing, spectroscopy and microscopy have had a revival during the last decade. The main advantage of these schemes from a practical standpoint is that they allow to select a wavelength for the idler beam, which interacts with the sample but is never detected, and a different wavelength for the signal beam, which can be detected with high efficiency. This is why such systems are referred sometimes to as *imaging/sensing with undetected photons*.

Recent experimental applications of nonlinear interferometers

Here we give an overview of recent experimental applications involving nonlinear interferometers in imaging, sensing, spectroscopy and microscopy:

- **Imaging**.

  Lemos *et al.* demonstrated in 2014 [10] a 2D imaging scheme that used a nonlinear interferometer based on induced coherence. They probed objects that modulate the phase and intensity of reflected light. The object was illuminated with infrared light, while the detection used visible light. The object was placed in the idler i_1 path between the two nonlinear crystals. The presence of the object modifies the interference of the signal photons, that is measured. Thus the object is imaged with photons that never interacted with it.

  Cardoso *et al.* demonstrated in 2018 [11] a 2D imaging scheme that they describe as the classical analog of Barreto *et al.* experiment. They defined its scheme as *classical* because they used stimulated parametric down-conversion instead of spontaneous parametric down-conversion. The first nonlinear crystal is illuminated by a pump beam and with a strong laser beam at the idler frequency.

Gilaberte *et al.* [12] demonstrated a quantum imaging scheme based on the use of nonlinear interferometers that allows imaging with minimal photo dose, while still capable of recording at video rate in the visible frequency range. The same group led by Markus Gräfe [13] demonstrated phase shifting digital holography with an SU(1,1) nonlinear interferometer.

- **Sensing**.

  Kutas *et al.* [14] made use of an SU(1,1) nonlinear interferometer to perform terahertz sensing of a sample while detecting only visible photons. They measured the layer thickness of an object placed in the idler arm. This work might be important for the terahertz industry, since there are no good semiconductor detectors for this frequency range and one can avoid the use of cryogenically cooled bolometers.

- **Spectroscopy**.

  Krivitsky *et al.* [15,16] used an SU(1,1) nonlinear interferometer to measure the real and imaginary part of the complex refractive index, the transmittance, the reflection and absorption of a medium in the infrared range by detecting only visible photons. The experiments worked in the low parametric gain regime of down-conversion and claim to be relevant for applications in material analysis, IR-photonics and telecommunications.

- **Microscopy**.

  The research groups of Ramelow [17] and Krivitsky [18] demonstrated experimentally hyperspectral mid-IR microscopy using an SU(1,1) nonlinear interferometer by detecting only near-IR radiation with a silicon-based camera. They imaged a biological sample with high spatial resolution (10 μm). The results showed a wide field of view, fast readout and negligible heat transfer to the sample.

Goals of this thesis

Nonlinear interferometers are at the heart of this thesis. The main results presented here are intended i) to investigate its use in optical coherence tomography schemes as well as ii) to explore fundamental concepts behind these types of schemes. As a final step we also explore the feasibility of doing imaging based on spatial modes of light. Our results are experimental results as well as theoretical analysis. The thesis key goals are:

- To demonstrate and characterize, experimentally and theoretically, the feasibility of doing optical coherence tomography (OCT) based on the use of nonlinear interferometers. We implement two experimental OCT schemes, one that works in the low parametric gain regime of parametric amplifiers (see Chapter 3) and another one that works in the high parametric gain regime (see Chapter 4).

- To study, and experimentally measure, signal-idler correlations in an induced coherence scheme to introduce a new measurement of quantum distinguishability (see Chapter 5). We also address the concepts of parametric amplification and quantum distinguishability in an induced coherence scheme (see Chapter 6) with the aim at trying to unveil the role and importance of each phenomena to explain why induced coherence is observed. There is an ongoing *dispute* on this topic that has not been clearly resolved yet [19, 20].

- To introduce a scheme to obtain transverse spatial information of a phase object (spatial spectroscopy) based on the use of nonlinear interferometers (see Chapter 7). The basic ingredient is the use of projection onto selected spatial modes in the detection stage, avoiding in this way the need to do spatial scans of the sample.

Outline of this thesis

The contents of this thesis are organized as follows.

Chapter 2 presents and sets the theoretical quantum formalism that describes how nonlinear interferometers work. We consider the two fundamental types of nonlinear interferometers that constitute the basis of this thesis: the SU(1,1) or *Yurke-type* interferometer, and the *Mandel-type* interferometer, based on the idea of induced coherence. Since nonlinear interferometers are formed by parametric amplifiers, the phenomenon of parametric down-conversion (PDC) is theoretically described in the Heisenberg and the Schrödinger pictures. We expand upon this formalism to the signal measured in different optical coherence tomography schemes. The last part of this chapter is devoted to summarize the main applications that these types of interferometers based on nonlinear parametric amplifiers have found in the last decade.

Chapter 3 is dedicated to present and describe the experimental implementation of an optical coherence tomography scheme based on induced coherence (*Mandel-type* interferometer). This system works in the low parametric gain regime of down-conversion. For the sake of comparison, we first do a brief review of the fundamental characteristics of conventional OCT systems, as well as the main equations that describe its functioning. Next we introduce the novel scheme proposed in this thesis and describe its basic operating principles. The experimental results obtained in the laboratory that demonstrate its feasibility are shown. The last part of the chapter is devoted to present the main advantages and limitations of this novel OCT scheme over its standard counterpart.

Chapter 4 begins by introducing a new optical coherence tomography scheme that solves some of the limitations presented in the previous chapter. We present a new experimental OCT scheme based on an SU(1,1) nonlinear interferometer operating in the high parametric gain regime of down-conversion (*Yurke-type* interferometer). This novel OCT proposal constitutes the core of this chapter,

in which the experimental setup and the main experimental results are described in detail.

Chapter 5 begins a series of two chapters devoted to studying fundamental quantum concepts of nonlinear interferometers based on the induced coherence effect. We discuss the concept of quantum distinguishability and its role in explaining induced coherence. We implement experimentally a measure of quantum distinguishability that is based on second-order correlation functions between the signal and idler photons generated in parametric down-conversion. To measure such correlations experimentally, coincidence measurements between single photons must be made. For that reason, the method used to measure coincidences between photons is described in detail. The new distinguishability measure introduced allows us to derive and demonstrate a complementarity inequality that relates two fundamental concepts of a quantum interferometer: quantum distinguishability and interference visibility.

Chapter 6 discusses the roles of parametric amplification and quantum distinguishability for explaining the phenomenon of induced coherence. There is an ongoing debate about whether, or how, quantum distinguishability, and the stimulated emission associated to parametric amplification are the *real* reasons for the induced coherence effect. The objective of this chapter is not to state categorically which of these explanations plays a more transcendental role, but to revisit a variant of usual experiments where the possibility of parametric amplification is eliminated, so only quantum distinguishability remains as possible explanation. However we need to move from measuring singles to measuring coincidences, which is a drawback for *interpreting* certain aspects of the experimental results.

Chapter 7 introduces and describes theoretically a new application of nonlinear interferometers: spatial spectroscopy, or imaging based on projection onto spatial modes. The experimental realization of this new scheme has not been carried out in this thesis. The idea of the proposal is to explore the possibility of obtaining transverse spatial information of a sample by means of projection into selected

spatial modes of light. We derive the main equations, and a simple example is shown to demonstrate the feasibility of the technique. This last chapter can be considered as a proposal for possible future work to be done with nonlinear interferometers.

CHAPTER

TWO

THE QUANTUM DESCRIPTION OF NONLINEAR INTERFEROMETERS

This chapter describes in detail the main characteristics of nonlinear interferometers, which are the experimental schemes implemented in this thesis. We first present a brief historical overview and a qualitative description of the different schemes generally used. Our attention shifts to present the theoretical basis of the two nonlinear interferometers considered in this work: the SU(1,1) interferometer (*Yurke-type*) and the interferometer based on induced coherence (*Mandel-type*). The physical phenomena of parametric down-conversion and parametric amplification is characterized quantum-mechanically using two different approaches: the Heisenberg and the Scrödinger pictures.

2.1 What is a Nonlinear Interferometer?

A *nonlinear interferometer* [7] is an interferometric scheme where nonlinear crystals or atomic systems generating light through nonlinear effects are placed inside the interferometer. In these schemes, two or more nonlinear sources are spatially separated and pumped coherently. Under various conditions, the radiation emitted from the sources may exhibit full or partial interference, or even no interference at all. The degree of interference is measured. Different factors affect the degree of coherence and, consequently, the degree of interference between various signals. We will analyze the conditions under which interference can be observed.

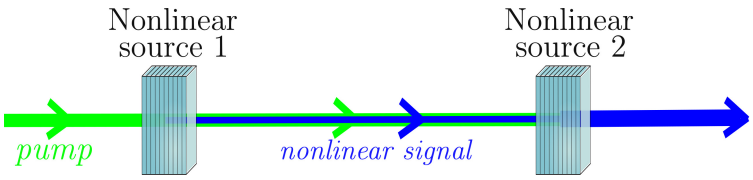

Figure 2.1: General scheme of a nonlinear interferometer. A pump beam illuminates coherently two spatially separated nonlinear optical sources. In the first nonlinear crystal the input signal is in the vacuum state, so there is spontaneous parametric down-conversion. The second nonlinear crystal acts as a parametric amplifier of the signal generated in the first nonlinear crystal.

Figure 2.1 shows a general scheme of the kind of nonlinear interferometers considered in this thesis. The generation of light by using nonlinear optics sources dates back to the pioneering work of N. Bloembergen, among many others [21]. These pioneering results already showed some of the promising features of these schemes: the measurement of the amplitude and phase of the nonlinear signals can provide information about the phase delays acquired by the nonlinear radiation due to the propagation from the first to the second source. This constitutes the starting point for future applications aimed at

determining properties of samples of interest placed between the two nonlinear sources.

In this thesis, we are interested in the case in which the first nonlinear optics source acts as a spontaneous parametric down-converter (SPDC), generating pairs of photons known as *signal* and *idler* photons, while the second one acts as a parametric amplifier. Depending on the strength of the nonlinear interaction in each nonlinear crystal, characterized by the so-called parametric gain G, photon pairs or bright twin beams are generated. Moreover two main configurations are considered: the SU(1,1) interferometer [8] and the interferometer based on *induced coherence* [9, 22].

2.2 Types of Nonlinear Interferometers

2.2.1 SU(1,1) interferometer (*Yurke-type*)

The pump beam illuminates coherently the two nonlinear crystals. In the first down-converter crystal signal and idler photons are generated. If the signal and idler photons generated in the first nonlinear crystal are injected in the second nonlinear crystal, as shown in Fig. 2.1, we have an SU(1,1) nonlinear interferometer[1]. The signal and idler photons can experience delays and/or losses when travelling from the first to the second nonlinear crystal. The resulting signal after the second nonlinear crystal, that is measured, can show amplification or de-amplification, depending on the phases acquired by the travelling photons, and the presence of loss.

The very first works with this type of nonlinear schemes dates back to the late 80's, and were aimed at increasing the sensitivity of phase estimation by means of using two squeezers [8]. In this regard, the first experimental execution of an SU(1,1) nonlinear interferometer was realized in the low parametric-gain regime of down-conversion (weak pumping) [23, 24]. Due to technical reasons, the

[1]See Appendix A for an explanation of where the term *SU(1,1)* comes from.

high parametric-gain version (strong pumping) of an SU(1,1) interferometer was not implemented until very recently [25, 26].

The usual geometries considered for linear interferometers (Mach-Zehnder, Michelson, Young and Sagnac) can be easily translated to the SU(1,1) nonlinear version. We are mainly interested in the Mach-Zehnder and Michelson geometries, both shown in Fig. 2.2.

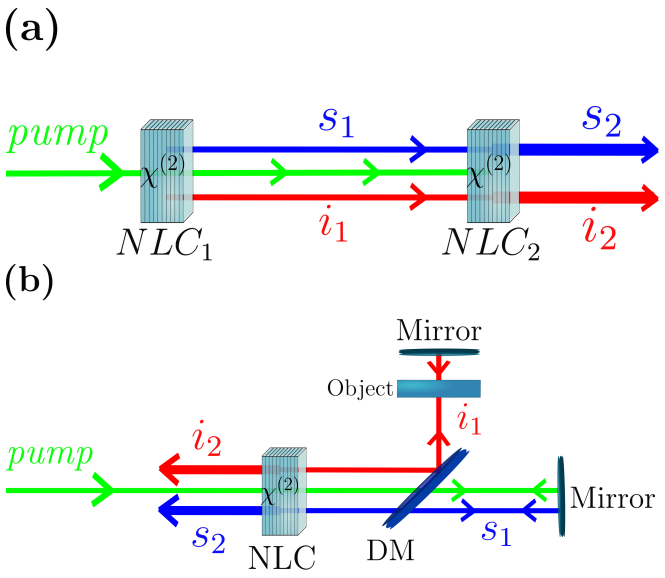

Figure 2.2: Different geometries of an SU(1,1) nonlinear interferometer. (a) Mach-Zehnder interferometer; (b) Michelson interferometer. NLC designate second-order nonlinear crystal, and $\chi^{(2)}$ is the nonlinear coefficient of the nonlinear crystals. DM designates a dichroic mirror.

In the Mach-Zehnder version [Fig. 2.2(a)] the pump illuminates the first nonlinear crystal, leading to the generation of the signal s_1 and the idler i_1 beams. The three beams impinge on the second nonlinear crystal, in which amplification or deamplification happens depending on the losses experienced and the phases acquired by each of the beams. The fact that the pump, the signal and the idler waves

propagate along the same path, makes this configuration more robust to the presence of random phase fluctuations.

A Michelson-type SU(1,1) configuration [Fig. 2.2(b)] can be implemented using an unique nonlinear crystal. In this case, the pump and the signal s_1 beams are separated from the idler i_1 by a dichroic mirror DM. All three beams are reflected back by mirrors and injected again in the nonlinear crystal, in which a parameric amplification process occurs. This geometry is more versatile than the Mach-Zehnder one since phase, delays or losses can be more easily introduced independently for each of the three beams.

Typically, the flux rate of signal photons s_2 or its spectrum are the quantities measured at the output of the interferometer. Depending on phase delays and losses, the interference fringes will show different amplitude, characterized by its visibility V. In Section 2.3.1 we derive the expressions for the signal spectrum and the visibility of the interference fringes for the low and high parametric gain regimes.

2.2.2 Interferometer based on the induced coherence effect (*Mandel-type*)

In 1991, Zou, Wang and Mandel [9] considered a nonlinear interferometer where only the idler beam generated in the first parametric down-conversion crystal passes through the second nonlinear optics source. This novel nonlinear interferometer is aimed at demonstrating the concept of *induced coherence*. They built an ingenious Mach-Zehnder type nonlinear interferometer where two second-order nonlinear crystals (NLC1 and NLC2) are optically pumped by two mutually coherent pump beams coming from the same laser [Fig. 2.3(a)].

Pairs of entangled photons might emerge from any of the crystals (signal s_1 and idler i_1 from NLC1, and signal s_2 and idler i_2 from NLC2) via PDC. The crystals are arranged such that idler i_1 from NLC1 passes through NLC2 and is perfectly aligned with idler i_2. The two signals s_1 and s_2 are mixed in a beam splitter BS and the output signal is detected. The key question is whether the two signal

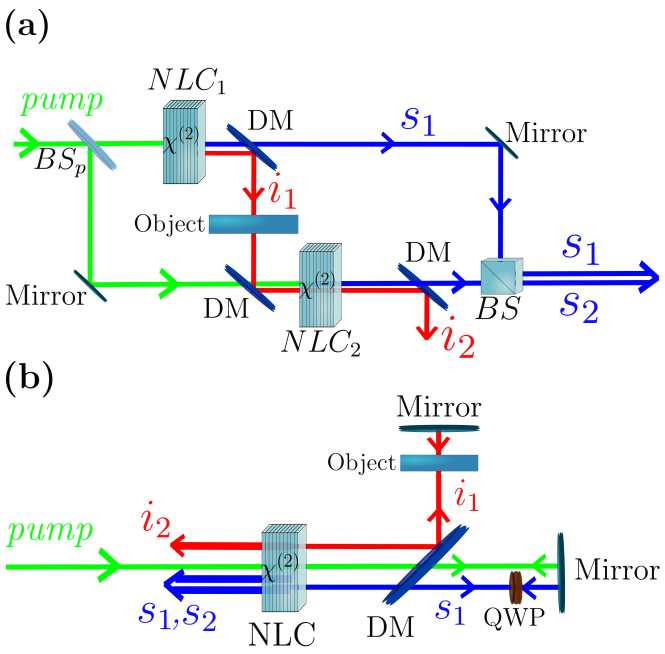

Figure 2.3: Different geometries of an interferometer based on the induced coherence effect. (a) Mach-Zehnder interferometer; (b) Michelson interferometer. NLC designate nonlinear crystals, and $\chi^{(2)}$ is the nonlinear coefficient of the nonlinear crystals. DM stands for dichroic mirror, and QWP stands for quarter-wave plate.

photons s_1 and s_2 will exhibit interference.

The effect of induced coherence can also be demonstrated using a Michelson type configuration [Fig. 2.3(b)]. In this case, the polarization of the signal beam s_1 is rotated 90° by using a quarter-wave plate (QWP). This prevents the signal beam from being amplified/deamplified on the second pass through the nonlinear crystal and allows to have three beams at the output of the interferometer: idler i_2 and signals s_1 and s_2 with orthogonal polarizations.

In the low parametric gain regime (weak pumping), paired photons are expected to be emitted from one or the other nonlinear crystal, being the probability of emission at both crystals simultaneously

negligible. Therefore any coherence induced between signal photons will not come from an induced emission process. In this scenario, if the idler beams i_1 and i_2 are indistinguishable, the signal photons s_1 and s_2 show first-order coherence [27]. If i_1 is partially blocked by a filter (NDF) with transmissivity τ, this results in a loss of first-order coherence between signal photons. In the extreme case that the idler i_1 is completely blocked by inserting a beam stop and prevented from reaching NLC2, the two signal beams show no first-order coherence and all interference disappears.

It was shown soon that the effect of induced coherence should still be present even in the high parametric gain regime (strong pumping) [28, 29], where signal photons can be generated simultaneously in both nonlinear crystals. The important point is that in all regimes the measurement of the degree of coherence between signal photons provides information about the value of the losses introduced in the idler i_1 path. For $|\tau| = 0$ (total blocking of idler i_1), there is no first-order coherence between signals s_1 and s_2. For $|\tau| = 1$ (no blocking), there is maximum first-order coherence. In Section 2.3.1 we present the expressions of first-order coherence for both gain regimes.

2.3 Quantum description

In this subsection, we provide a quantum description of an SU(1,1) nonlinear interferometer and an interferometer based on induced coherence. We first need to characterize theoretically the process of parametric down-conversion and extend this analysis for two spatially separated down-converters. We consider the two main approaches: the Heisenberg picture (Subsection 2.3.1) and the Schrödinger picture (Subsection 2.3.3).

2.3.1 Heisenberg picture

The first considerations about the phenomenon of parametric down-conversion (PDC) date back to the decade of 1960s [30–32]. The first

experimental realizations were done soon after [33–35]. Parametric down-conversion, also called in the early days of the field parametric fluorescence, is a nonlinear optical process in which a photon of higher frequency from a strong pump beam interacts with the molecules of a nonlinear medium that mediate the generation of a pair of photons at a lower frequency (see Fig. 2.4). These photons are called, for historical reasons, *signal* and *idler*. Key parameters that determine the efficiency of this process are the pump beam power, the second-order nonlinear susceptibility ($\chi^{(2)}$) of the medium and the length of the nonlinear crystal.

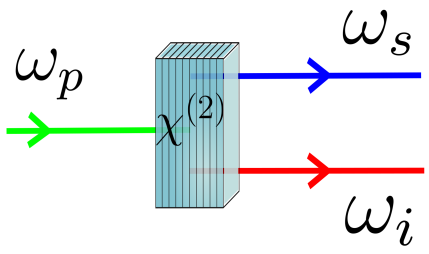

Figure 2.4: General scheme of parametric down-conversion. A pump photon with frequency ω_p interacts with the molecules of a nonlinear crystal with nonlinear susceptibility $\chi^{(2)}$, and two photons are generated: the signal (frequency, ω_s) and the idler (frequency, ω_i). The frequencies of all waves obey the relationship $\omega_p = \omega_s + \omega_i$, that reflects conservation of energy in a parametric process. The subscripts p, s, i refer to the pump, signal and idler waves, respectively.

Although certain models, based exclusively on the use of classical electromagnetism concepts, can describe particular aspects of parametric down-conversion, only a full quantum description can successfully describe all aspects of the process. For instance, a quantum description incorporates naturally the role of quantum vacuum fluctuations in the generation of two lower-frequency photons (signal and idler) in spontaneous parametric down-conversion, while classical modes might need to consider artificially the presence of *input*

2.3 Quantum description

classical noise. In a general scenario, we need to consider multiple properties of the waves involved: spatial and spectral shape, coherence, intensity, and type of quantum state of the pump beam...

In the Heisenberg picture, the quantum state of signal-idler photons is considered to be unchanged (not evolving) during the time evolution of the process. The field operators are the variables that evolve as a function of the propagation distance all along the nonlinear crystal. Therefore the aim in the Heisenberg picture is to derive the relation between the input field operators ($\hat{b}_{s,i}$ and $\hat{b}^{\dagger}_{s,i}$), and the output signal and idler operators ($\hat{a}_{s,i}$ and $\hat{a}^{\dagger}_{s,i}$). In all cases we assume that the pump beam is a strong classical pump beam undepleted at the end of the nonlinear crystal. Figure 2.5 shows a sketch of the parametric down-conversion process, with all the waves and operators considered in the Heisenberg picture.

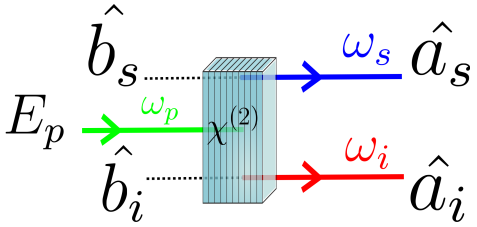

Figure 2.5: Parametric down-conversion scheme in the Heisenberg picture. A pump photon with frequency ω_p and electric field $E_p = E_p^+ + E_p^-$ interacts with a nonlinear medium with susceptibility $\chi^{(2)}$ that mediates the generation of two photons: signal (frequency, ω_s) and idler (frequency, ω_i). $\hat{b}_{s,i}$ are the input annihilation operators for the signal and idler modes. $\hat{a}_{s,i}$ are the output annihilation operators for the signal and idler modes, respectively.

We start from the classical wave equation that describes the propagation of the field amplitudes in the paraxial and narrowband regime. This equation relates the field amplitude with the nonlinear polarization induced by the nonlinear medium. The nonlinear polarization can be written as a function of the incident electric fields. The field

amplitudes are quantized by substituting them by field operators and the evolution equations are obtained for PDC. Finally, the solution to these equations are the desired input-output operators relations (so-called *Bogoliubov transformations*). In [36] you can find a detailed derivation of all expressions leading to the Bogoliubov transformations. Here we give a succinct summary of the mathematical derivations.

The first step is to write the wave equation in a nonlinear optical media that describes the spatial and temporal evolution of a classical electromagnetic field inside the medium. We consider the *nonresonant* case, in which the frequencies of the light beams are far from possible atomic or molecular transitions in the nonlinear crystal. In this scenario, the wave equation is written as [37]

$$\nabla^2\mathbf{E} - \frac{n^2}{c^2}\frac{\partial^2\mathbf{E}}{\partial t^2} = \frac{1}{\epsilon_0 c^2}\frac{\partial^2\mathbf{P}}{\partial t^2}, \tag{2.1}$$

where $\mathbf{E}$ is the electric field, $\mathbf{P}$ is the induced polarization of the medium, t is time, n is the refractive index of the nonlinear medium, c the velocity of light in vacuum and ϵ_0 is the electrical permittivity of vacuum.

The polarization $\mathbf{P}$ represents the density of electric dipoles in a dielectric material. In other words, the material's response when it is excited by an external electromagnetic wave with electric field $\mathbf{E}$. Since optical nonlinearities are generally small, the induced polarization of the medium can be written as a function of powers of the incident electric field [38] as

$$\mathbf{P} = \epsilon_0\chi^{(1)}\mathbf{E} + \epsilon_0\chi^{(2)}\mathbf{EE} + \epsilon_0\chi^{(3)}\mathbf{EEE} + ... \tag{2.2}$$

$\chi^{(1)}$ is the first-order (linear) susceptibility. It describes the linear response of the medium ($\mathbf{P^L}$). $\chi^{(2)}$ is the second-order nonlinear susceptibility, $\chi^{(3)}$ is the third-order nonlinear susceptibility and so forth. The higher nonlinear order terms stand for the nonlinear response of the medium ($\mathbf{P^{NL}}$). The three-wave mixing processes like parametric down-conversion are $\chi^{(2)}$-dependent interactions, so this

is the nonlinear coefficient of interest for us. Typical values of $\chi^{(2)}$ vary among different materials, they can range between a few 1-2 pm/V to values of 100-300 pm/V.

Light beams in the experiments considered in this thesis are well approximated as paraxial narrowband waves with well-defined polarization propagating along the z direction. The electric field and the induced polarization can be written as the sum of several waves with different central frequencies and polarizations as $\mathbf{E} = \sum_k \mathcal{E}_j \hat{e}_j + h.c.$ and $\mathbf{P} = \sum_j \mathcal{P}_j \hat{e}_j + h.c.$ with

$$\mathcal{E}_j(t, \mathbf{r}, z) = \frac{1}{(2\pi)^{3/2}} \int d\Omega d\mathbf{q} E_j(\Omega, \mathbf{q}, z) \exp\left\{ik_j z + i\mathbf{q}\cdot\mathbf{r} - i\omega t\right\},$$

$$\mathcal{P}_j(t, \mathbf{r}, z) = \frac{1}{(2\pi)^{3/2}} \int d\Omega d\mathbf{q} P_j(\Omega, \mathbf{q}, z) \exp\left\{i\mathbf{q}\cdot\mathbf{r} - i\omega t\right\}. \quad (2.3)$$

The index j stand for each of the waves considered in the nonlinear interaction. $\mathbf{q} = (q_x, q_y)$ is the transverse wave vector and $\mathbf{r} = (x, y)$ is the spatial transverse coordinate. The frequency ω is written as $\omega = \omega_j^0 + \Omega$, with ω_j^0 being the central frequency of the wave and Ω the frequency deviation from the corresponding central frequency. In the narrowband regime considered here, the frequency deviation is much more smaller than the central frequency, i.e. $\Omega \ll \omega_j^0$. The longitudinal wave number k_j is

$$k_j(\Omega, \mathbf{q}) = \left[\frac{(\omega_j^0 + \Omega)^2 n_j^2}{c^2} - |\mathbf{q}|^2\right]^{1/2}. \quad (2.4)$$

Considering the slowly varying approximation, in which the envelope of a wave varies slowly in time and space compared to its wavelength, a simplified version of the wave equation [Eq. (2.1)] can be obtained. Under this approximation the coupled nonlinear equations that describe the evolution in the longitudinal coordinate z of the electrical field amplitudes E_j and the polarizations P_j are [39]

$$\frac{\partial E_j(\Omega, \mathbf{q}, z)}{\partial z} = i\frac{\omega_j^0}{2\epsilon_0 c n_j} P_j^{NL}(\Omega, \mathbf{q}, z) \exp\left\{-ik_j z\right\}. \quad (2.5)$$

To obtain the quantum version of these coupled equations, quantization of the electric and polarization fields is required. This procedure assumes that the field operators ($\hat{\mathcal{E}}_j$ and $\hat{\mathcal{P}}_j$) have a similar form to the classical version, that is

$$\begin{aligned}\hat{\mathcal{E}}_j^+(t,\mathbf{r},z) = \frac{i}{(2\pi)^{3/2}}\int d\Omega d\mathbf{q} f_0\, \hat{a}_j(\Omega,\mathbf{q},z)\times \\ \times \exp\left\{ik_j z + i\mathbf{q}\cdot\mathbf{r} - i\omega t\right\},\end{aligned} \tag{2.6}$$

where the normalization function is $f_0 = [\hbar(\omega_j^0)/2\epsilon_0 c n_j]^{1/2}$. The annihilation and creation operators ($\hat{a}_j$ and $\hat{a}_j^\dagger$) fulfill the commutation relations

$$[\hat{a}_j(\Omega,\mathbf{q}), \hat{a}_j^\dagger(\Omega',\mathbf{q}')] = \delta(\Omega-\Omega')\delta(\mathbf{q}-\mathbf{q}'), \tag{2.7}$$

$$[\hat{a}_j(\Omega,\mathbf{q}), \hat{a}_j(\Omega',\mathbf{q}')] = 0, \tag{2.8}$$

$$[\hat{a}_j^\dagger(\Omega,\mathbf{q}), \hat{a}_j^\dagger(\Omega',\mathbf{q}')] = 0. \tag{2.9}$$

Analogously to Eq. (2.5), the coupled nonlinear equations that describe the evolution of the electrical field operators $\hat{E}_j^+$ are

$$\frac{\partial \hat{E}_j^\dagger(\Omega,\mathbf{q},z)}{\partial z} = i\frac{\omega_j^0}{2\epsilon_0 c n_j}\left[\hat{P}_j^{NL}(\Omega,\mathbf{q},z)\right]^\dagger \exp\left\{-ik_j z\right\}. \tag{2.10}$$

Finally, by substituting the appropriate nonlinear polarization $\hat{P}_j^{NL}$ that characterizes a concrete nonlinear process one can obtain the evolution equations for the field operators [36, 39]. For the case of parametric down-conversion the signal and idler operators evolve as

$$\begin{aligned}\frac{\partial \hat{a}_s(\Omega_s,\mathbf{q}_s,z)}{\partial z} = -i\beta\int d\Omega_i d\mathbf{q}_i \hat{a}_i^\dagger(\Omega_i,\mathbf{q}_i,z) F_p(\Omega_s+\Omega_i,\mathbf{q}_s+\mathbf{q}_i) \\ \times \exp\left\{i\Big[k_p(\Omega_s+\Omega_i,\mathbf{q}_s+\mathbf{q}_i) - k_s(\Omega_s,\mathbf{q}_s) - k_i(\Omega_i,\mathbf{q}_i)\Big]\right\},\end{aligned} \tag{2.11}$$

$$\begin{aligned}\frac{\partial \hat{a}_i(\Omega_i,\mathbf{q}_i,z)}{\partial z} = -i\beta\int d\Omega_s d\mathbf{q}_s \hat{a}_s^\dagger(\Omega_s,\mathbf{q}_s,z) F_p(\Omega_s+\Omega_i,\mathbf{q}_s+\mathbf{q}_i) \\ \times \exp\left\{i\Big[k_p(\Omega_s+\Omega_i,\mathbf{q}_s+\mathbf{q}_i) - k_s(\Omega_s,\mathbf{q}_s) - k_i(\Omega_i,\mathbf{q}_i)\Big]\right\},\end{aligned} \tag{2.12}$$

where the frequencies of the signal and idler down-converted photons can be written as $\omega_{s,i} = \omega^0_{s,i} + \Omega_{s,i}$, $\omega^0_{s,i}$ are the central frequencies and $\Omega_{s,i}$ the frequency deviations from the corresponding central frequencies. The phase mismatch function is $\Delta k = k_p(\Omega_s + \Omega_i, \mathbf{q}_s + \mathbf{q}_i) - k_s(\Omega_s, \mathbf{q}_s) - k_i(\Omega_i, \mathbf{q}_i)$, with $k_{p,s,i}$ being the transverse wave numbers of the pump, signal and idler photons, respectively. The function $F_p(\Omega_s + \Omega_i, \mathbf{q}_s + \mathbf{q}_i)$ defines the spectral and spatial profile of the pump beam at the initial facet ($z = 0$) of the nonlinear medium with

$$\int d\Omega\, d\mathbf{q} \left| F_p(\Omega, \mathbf{q}) \right|^2 = N_p, \tag{2.13}$$

N_p being the total number of photons of the pump beam. The constant β, measured in units of $s^{1/2}$ is

$$\beta = \left[\frac{\hbar \omega_p^0 \omega_s^0 \omega_i^0 [\chi^{(2)}]^2}{64\pi^3 \epsilon_0 c^3 n_p(\omega_p^0) n_s(\omega_s^0) n_i(\omega_i^0)} \right]^{1/2}. \tag{2.14}$$

$n_{p,s,i}$ are refractive index at the corresponding central frequencies.

The solutions of Eqs. (2.11) and (2.12) can be written as

$$\begin{aligned} \hat{a}_s(\Omega, \mathbf{q}) = \int d\Omega'\, d\mathbf{q}' \Big[& A_s(\Omega, \mathbf{q}, \Omega', \mathbf{q}') \hat{b}_s(\Omega', \mathbf{q}') + \\ & + B_s(\Omega, \mathbf{q}, \Omega', \mathbf{q}') \hat{b}_i^\dagger(\Omega', \mathbf{q}') \Big], \end{aligned} \tag{2.15}$$

$$\begin{aligned} \hat{a}_i(\Omega, \mathbf{q}) = \int d\Omega'\, d\mathbf{q}' \Big[& A_i(\Omega, \mathbf{q}, \Omega', \mathbf{q}') \hat{b}_i(\Omega', \mathbf{q}') + \\ & + B_i(\Omega, \mathbf{q}, \Omega', \mathbf{q}') \hat{b}_s^\dagger(\Omega', \mathbf{q}') \Big]. \end{aligned} \tag{2.16}$$

These are the Bogoliubov transformations, a relationship between the input annihilation operators $\hat{b}_{s,i}$ (at the input face of the nonlinear crystal ($z = 0$)), and the output annihilation operators $\hat{a}_{s,i}$ (at the output face of the nonlinear crystal ($z = L$)). $A_{s,i}$ and $B_{s,i}$ are functions that should be determined for each case. In general, these functions have to be determined numerically. However, under certain assumptions and approximations, Eqs. (2.11) and (2.12) can be

solved analytically. This is the case when the pump is considered to be a continuous-wave (CW) and a plane-wave beam. This approximation is valid when the bandwidth of the down-converted photons is much larger than the pump bandwidth, $\Delta_{dc} \gg \Delta_p$ [40]. In addition, the pump can be considered a plane wave when the length of the nonlinear crystal is much larger that the Rayleigh range of the pump beam. In these circumstances, the propagation equations (2.11) and (2.12) can be simplified and written as

$$\frac{\partial \hat{a}_s(\Omega, \mathbf{q}, z)}{\partial z} = -i\sigma \hat{a}_i^\dagger(-\Omega, -\mathbf{q}, z) \exp\left\{i\Delta k z\right\}, \tag{2.17}$$

$$\frac{\partial \hat{a}_i(\Omega, \mathbf{q}, z)}{\partial z} = -i\sigma \hat{a}_s^\dagger(-\Omega, -\mathbf{q}, z) \exp\left\{i\Delta k z\right\}, \tag{2.18}$$

where $\Delta k = k_p^0 - k_s(\Omega, \mathbf{q}) - k_i(-\Omega, -\mathbf{q})$ and the coefficient σ (measured in units of m^{-1}) is

$$\sigma = \left[\frac{\hbar \omega_p^0 \omega_s^0 \omega_i^0 [\chi^{(2)}]^2 R_p}{8\epsilon_0 c^3 n_p(\omega_p^0) n_s(\omega_s^0) n_i(\omega_i^0)}\right]^{1/2}, \tag{2.19}$$

R_p is the flux rate of pump photons (photons/s/m^2), that can be approximated as

$$R_p = \frac{E_p}{\hbar \omega_p T_0 S_p}. \tag{2.20}$$

E_p is the energy per pulse of the pump beam, T_0 is the pump pulse duration and S_p the effective area of the pump beam. The solution to Eqs. (2.17) and (2.18) is [41, 42]

$$\hat{a}_s(\Omega, \mathbf{q}) = U_s(\Omega, \mathbf{q})\, \hat{b}_s(\Omega, \mathbf{q}) + V_s(\Omega, \mathbf{q})\, \hat{b}_i^\dagger(-\Omega, -\mathbf{q}), \tag{2.21}$$

$$\hat{a}_i(\Omega, \mathbf{q}) = U_i(\Omega, \mathbf{q})\, \hat{b}_i(\Omega, \mathbf{q}) + V_i(\Omega, \mathbf{q})\, \hat{b}_s^\dagger(-\Omega, -\mathbf{q}). \tag{2.22}$$

The functions $U_{s,i}(\Omega, \mathbf{q})$ and $V_{s,i}(\Omega, \mathbf{q})$ are

$$U_{s,i}(\Omega, \mathbf{q}) = \left\{\cosh(\Gamma L) - i\frac{\Delta_{s,i}}{2\Gamma}\sinh(\Gamma L)\right\} \exp\left[\frac{i\delta_{s,i} L}{2}\right], \tag{2.23}$$

2.3 Quantum description

$$V_{s,i}(\Omega, \mathbf{q}) = -\frac{i\sigma}{\Gamma} \sinh(\Gamma L) \exp\left[i\frac{\delta_{s,i} L}{2}\right]. \tag{2.24}$$

L is the nonlinear crystal length. Under the paraxial approximation, and for $\mathbf{q} \sim 0$, an important case that we will consider in the following chapters, the phase matching functions $\Delta_{s,i}$ can be written as $\Delta_s = -\Delta_i = (D_i - D_s)\Omega$. $D_{s,i}$ are the inverse group velocities at the signal and idler central frequencies, respectively. The functions $\delta_{s,i}$ are $\delta_{s,i} = k_p + k_{s,i}(\Omega, \mathbf{q}) - k_{i,s}(-\Omega, -\mathbf{q})$ and the parameter Γ is

$$\Gamma = \left(\sigma^2 - \frac{\Delta_s^2}{4}\right)^{1/2}. \tag{2.25}$$

The flux rate (photons/s/m^2) of signal (or idler) photons generated is

$$\begin{aligned} R_s &= \frac{1}{(2\pi)^3} \int d\Omega d\mathbf{q} \int d\Omega' d\mathbf{q}' \langle \hat{a}_s^\dagger(\Omega, \mathbf{q}) \hat{a}_s(\Omega', \mathbf{q}') \rangle \\ &\times \exp\Big[-i\Big(\Omega - \Omega'\Big)t + i\Big(\mathbf{q} - \mathbf{q}'\Big) \cdot \mathbf{r}\Big)\Big] = \\ &= \frac{1}{(2\pi)^3} \int d\Omega \, d\mathbf{q} \left| V_s(\Omega, \mathbf{q}) \right|^2. \end{aligned} \tag{2.26}$$

An important parameter that characterizes any PDC process is the so-called parametric gain (G). To know how to measure this parameter, and get some physical intuition about what it represents, let us analyze the flux rate of down converted signal photons in the single-mode approximation. In this approach, we just focus on photons generated around the central frequency ω_s^0 and consider a small frequency deviation around the central frequency ($\Delta\Omega$) and a small $\Delta\mathbf{q}$. Since in this case $\Gamma = \sigma$, the flux rate of signal photons at the output facet ($z = L$) of the nonlinear crystal reads [43]

$$R_s = \frac{1}{(2\pi)^3} \sinh^2(\sigma L) \Delta\Omega \, \Delta\mathbf{q} = R_0 \sinh^2(\sigma L). \tag{2.27}$$

The parametric gain is defined as

$$G = \sigma L. \tag{2.28}$$

If we measure the signal during time T_D in an integration area S_D, the number of photons detected is

$$N_s = N_0 \sinh^2(\sigma L). \tag{2.29}$$

where $N_0 = \Delta\Omega\, \Delta\mathbf{q} T_D S_D/(2\pi)^3$. Taking into account Eq. (2.29), the gain is an estimation of the number of photons generated per unit frequency and spatial bandwidth. Figure 2.6 shows the photon flux rate (in arbitrary units) of signal photons emitted for a 1-mm-long nonlinear crystal as a function of the parametric gain.

When $G = \sigma L \ll 1$, the PDC process is said to be in the low parametric gain regime. The flux rate grows linearly as a function of the gain. On the other hand, if $G \gg 1$, the PDC process is said to be in the high parametric gain regime, the flux rate grows exponentially as a function of the gain. In any PDC process, a number of spatio-temporal independent modes can be selected [44, 45], so there is no cross-talk among them. It can be demonstrated that in the low parametric gain regime, the flux rate of paired photons generated per mode is much smaller than one, while in the high parametric gain regime the flux rate of photons generated per mode is much higher than one.

As can be deduced from analyzing the factors that influence the value of σL, one can increase the parametric gain G by:

- *Reducing the area of the pump beam, S_p.* The coefficient σ [see Eq. (2.19)] depends on the area of the pump beam as $\sim 1/\sqrt{S_p}$, so stronger focusing of the pump beam implies a higher nonlinear coefficient, and therefore a higher parametric gain. However, if we still want to use the plane wave approximation, we need that this strong focusing does not break down the fact that the Rayleigh range of the pump beam is much larger than the crystal length.

- *Reducing the pump pulse duration, T_0.* Increasing the peak intensity of the pump beam is key to increase the parametric gain. We need to combine two things: reducing the pump pulse

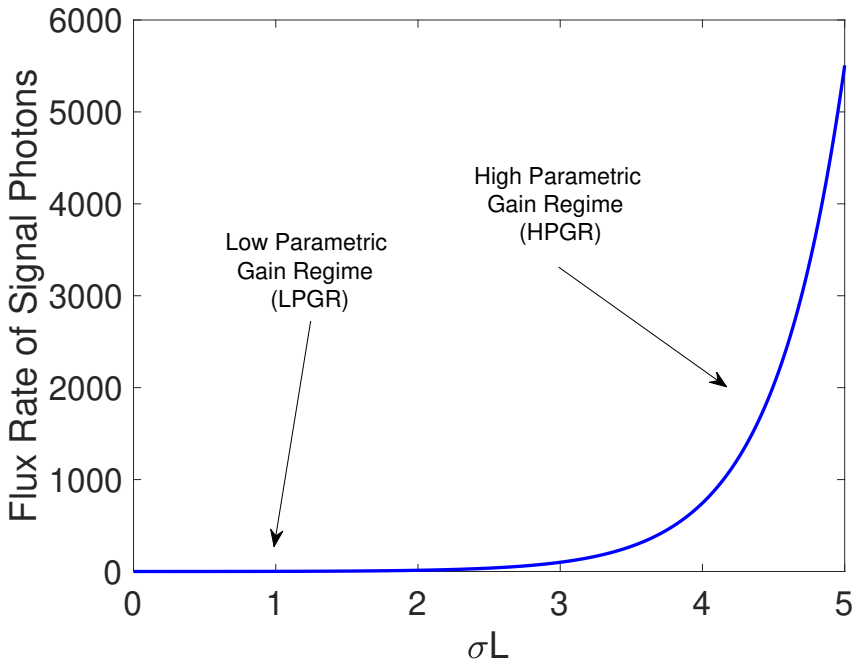

Figure 2.6: Flux rate of signal photons generated per mode as a function of the gain $G = \sigma L$, according to Eq. (2.29). The two insets indicate graphically the two regimes of PDC: the so-called low and high parametric gain regimes.

duration T_0 and/or increasing the energy per pulse E_p. The ideal case would be to have the shortest and more energetic pulse, but in a realistic scenario there must be a compromise between energy and pulse duration. We will see in a following chapter that the use of pulsed lasers that generate picosecond pulses with energy per pulse of tens of microjoules constitutes a convenient solution.

- *Using longer nonlinear crystals.* The parametric gain [Eq. (2.28)] depends linearly on the length of the nonlinear medium, so that

longer crystals lead to higher gain. However, the use of longer crystals can also produce undesirable effects for certain applications, such as a smaller bandwidth. The axial resolution of optical coherence tomography schemes deteriorates with diminishing sizes of the bandwidth.

To conclude with the analysis of the parametric gain, let us consider some numbers obtained from real experimental implementations. In the majority of experiments a continuous-wave (CW) laser source is used to pump the nonlinear crystal. High flux rates of down-converted photons using a CW pump laser have been achieved, e.g. $\sim 10^{12}$ entangled photons pairs per second in Ref. [46], which is equivalent to a classical power level of 0.3 μW. *But does this mean that this PDC process is in the high parametric gain regime ($G > 1$)?*

With the parameters used in this experiment, and considering a pump power[2] of up to $P = 2$ W, the calculation of the parametric gain leads to a value of about $G \approx 10^{-12}$, which clearly corresponds to the low parametric gain regime of PDC. This evidences the fact that the parametric gain is a measure of the number of down-converted photons generated per mode, and not just a measure of the photon fluxes generated.

Instead, if a picosecond pulsed laser with pulse duration $T_0 = 18$ ps and average power of $P_{av} = 20$ mW is used to illuminate the same nonlinear crystal, the parametric gain increases dramatically to a value of about $G \approx 10$. This example puts forward the key point to achieve the high parametric gain regime of PDC: a pulsed pump with high peak power. This is why the use of CW lasers does not lead to high-gain PDC processes.

To clarify even more this idea, let us consider a pulsed laser with pulse duration $T_0 = 100$ fs and the same average power $P_{av} = 20$ mW. The parametric gain in this case is reduced to a value of about $G \approx 0.5$, which corresponds again to a low-gain PDC process. This

[2]This value of pump power was provided to us by one of the authors of the paper.

is a clear example of how energy per pulse and pulse duration both matter, and explains why picosecond lasers with tens of milliwatts average power are used to implement parametric down-conversion process that operate in the high parametric gain regime [47, 48].

Quantum analysis of an SU(1,1) nonlinear interferometer

We have introduced the main expressions in the Heisenberg picture that describe parametric down-conversion in a single nonlinear crystal. Let us extend now this analysis to the case of nonlinear interferometers, in which two PDC processes take place. We carry out the analysis for the two types of nonlinear interferometers implemented experimentally in this thesis: an SU(1,1) configuration and an interferometer based on induced coherence.

A sketch of an SU(1,1) nonlinear interferometer is shown in Fig. 2.7. The pump beam illuminates a nonlinear crystal (NLC) where signal (s_1) and idler (i_1) waves are generated. The pump and the signal are transmitted through a dichroic mirror, while the idler is reflected. The pump and the signal are reflected by a mirror and enter again the nonlinear crystal. The distance traveled by the signal beam before reaching the crystal is z_s. We consider a reflectivity r_s that account for frequency independent losses in the signal path due to the optical elements. The idler beam interacts with a lossy object with reflectivity $r_i(\Omega)$ and is reflected back onto the crystal, traveling a total distance z_i.

The pump beam illuminates the same nonlinear crystal backwards, and the signal (s_1) and idler (i_1) are also injected back into the nonlinear crystal. Signal s_2 and idler i_2 waves are generated after the second pass by the nonlinear crystal. Finally, the spectrum and/or the flux rate of the signal photons s_2 is the quantity measured by detector D.

We neglect the spatial dependence of all waves involved: the pump, signal and idler beams are considered plane waves. The relationship between the input annihilation operators $\hat{b}_s$ and $\hat{b}_i$ and the

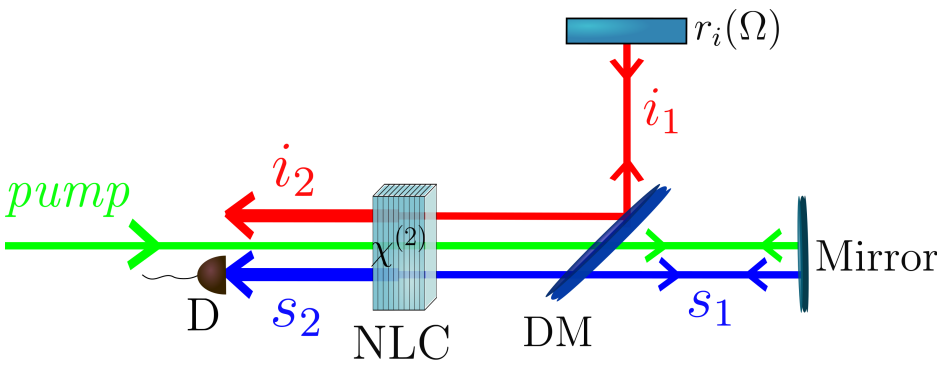

Figure 2.7: Sketch of an SU(1,1) nonlinear interferometer.

output operators $\hat{a}_{s1}$ and $\hat{a}_{i1}$ of the signal and idler beams generated after the first pass by the nonlinear crystal is described by the Bogoliubov transformations

$$\hat{a}_{s_1}(\Omega) = U_s(\Omega)\hat{b}_s(\Omega) + V_s(\Omega)\hat{b}_i^\dagger(-\Omega), \tag{2.30}$$

$$\hat{a}_{i_1}(\Omega) = U_i(\Omega)\hat{b}_i(\Omega) + V_i(\Omega)\hat{b}_s^\dagger(-\Omega). \tag{2.31}$$

The expressions for $U_{s,i}$ and $V_{s,i}$ are the ones shown in Eqs. (2.23) and (2.24). The transformations of the operators $\hat{a}_{i_1}$ and $\hat{a}_{s_1}$ accounting for propagation and loss [49, 50] read

$$\hat{a}_{i_1}(\Omega) \Longrightarrow r_i(\Omega)\hat{a}_{i_1}(\Omega)\exp\left[i\varphi_i(\Omega)\right] + \hat{f}_i(\Omega), \tag{2.32}$$

$$\hat{a}_{s_1}(\Omega) \Longrightarrow r_s\hat{a}_{s_1}(\Omega)\exp\left[i\varphi_s(\Omega)\right] + \hat{f}_s(\Omega), \tag{2.33}$$

where $\varphi_{s,i}(\Omega) = (\omega_{s,i}^0 + \Omega)z_{s,i}/c$ and $\hat{f}_{s,i}$ are operators that fulfill the commutation relation $[\hat{f}_i(\Omega), \hat{f}_i^\dagger(\Omega')] = [1 - |r_i(\Omega)|^2]\,\delta(\Omega - \Omega')$ and $[\hat{f}_s(\Omega), \hat{f}_s^\dagger(\Omega')] = [1 - |r_s|^2]\,\delta(\Omega - \Omega')$.

The PDC process occurring in the second nonlinear crystal is characterized by the Bogoliubov transformation for the signal beam $\hat{a}_{s2}(\Omega)$ as

$$\hat{a}_{s_2}(\Omega) = U_s(\Omega)\hat{a}_{s_1}(\Omega) + V_s(\Omega)\hat{a}_{i_1}^\dagger(-\Omega), \tag{2.34}$$

which yields

$$\begin{aligned}
&\hat{a}_{s_2}(\Omega) = \Big[r_s U_s(\Omega) U_s(\Omega) \exp\left[i\varphi_s(\Omega)\right] + \\
&+ r_i^*(-\Omega) V_s(\Omega) V_i^*(-\Omega) \exp\left[-i\varphi_i(-\Omega)\right] \Big] \hat{b}_s(\Omega) + \\
&+ \Big[r_s U_s(\Omega) V_s(\Omega) \exp\left[i\varphi_s(\Omega)\right] + \\
&+ r_i^*(-\Omega) V_s(\Omega) U_i^*(-\Omega) \exp\left[-i\varphi_i(-\Omega)\right] \Big] \hat{b}_i^\dagger(-\Omega) + \\
&+ U_s(\Omega) f_s(\Omega) + V_s(\Omega) \hat{f}_i^\dagger(-\Omega).
\end{aligned} \tag{2.35}$$

The spectrum of the signal photons s_2 is

$$\begin{aligned}
&S(\Omega) = \langle \hat{a}_{s_2}^\dagger(\Omega) \hat{a}_{s_2}(\Omega) \rangle = \\
&= \Big[1 - |r_i(\Omega)|^2 \Big] |V_s(\Omega)|^2 + \\
&+ \Big| r_s U_s(\Omega) V_s(\Omega) \exp\left[i\varphi_s(\Omega)\right] + \\
&+ r_i^*(-\Omega) V_s(\Omega) U_i^*(-\Omega) \exp\left[-i\varphi_i(-\Omega)\right] \Big|^2 .
\end{aligned} \tag{2.36}$$

Figure 2.8 shows some examples of signal spectra for different values of the idler reflectivity r_i, according to Eq. (2.36). For the sake of simplicity, we consider $r_s = 1$, no frequency dependence of r_i and a fixed path unbalance between signal and idler paths of $\Delta z = z_s - z_i = 300\ \mu m$. When the idler path is blocked ($r_i = 0$), the signal spectrum does not show any modulation. Fringes appear for values $r_i \neq 0$, and show maximum visibility for $r_i = 1$.

The flux rate of signal photons can be calculated as[3]

$$N_s = \frac{1}{2\pi} \int d\Omega S(\Omega). \tag{2.37}$$

[3]The $1/(2\pi)$ term that appears in front of the integral, instead of the term $1/(2\pi)^3$ that appears in Eq. 2.27, is due to the fact that here we are considering as variable only the frequency, neglecting the $\mathbf{q}$ variable.

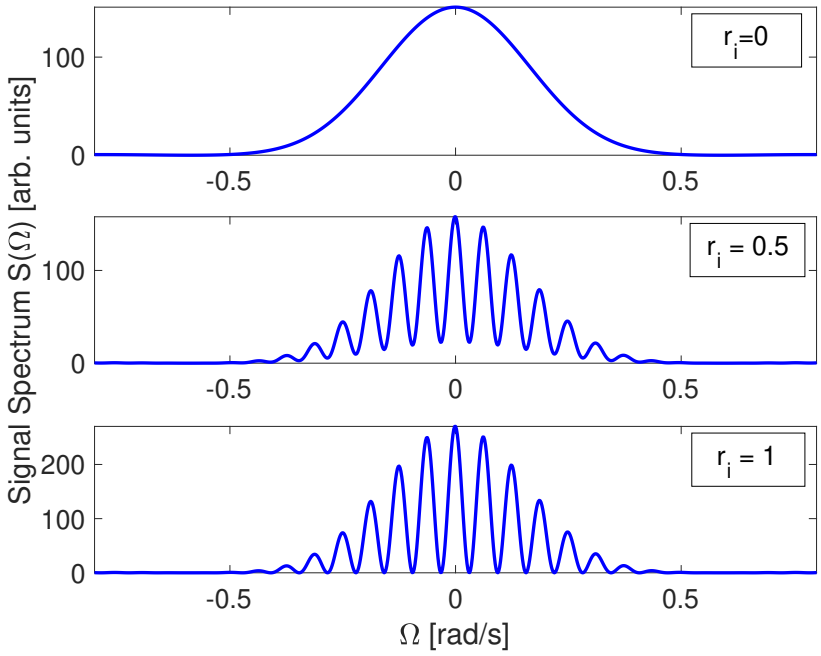

Figure 2.8: Signal spectra $S(\Omega)$ for three different values of the idler losses r_i. (TOP) $r_i = 0$. (CENTER) $r_i = 0.5$. (BOTTOM) $r_i = 1$. We make use of Eq. (2.36).

We measure the flux rate of signal photons N_s as a function of the path length difference $\Delta z = z_s - z_i$ and determine the visibility of the interference fringes. The visibility is defined as

$$V = \frac{N_s^{max} - N_s^{min}}{N_s^{max} + N_s^{min}} \tag{2.38}$$

with N_s^{max} and N_s^{min} being the maximum and the minimum values of flux rate, respectively. The visibility of the fringes is [51]

$$V = \frac{2|r_s||r_i|\,|\nu|}{(1-|r_i|^2)\alpha + |r_i|^2\beta + |r_s|^2\gamma}, \tag{2.39}$$

where

$$\nu = \int d\Omega\, U_s(\Omega) U_i(-\Omega) \left|V_s(\Omega)\right|^2 \exp\left[i\frac{\Omega}{c}\Delta z\right],$$
$$\alpha = \int d\Omega\ \left|V_s(\Omega)\right|^2,$$
$$\beta = \int d\Omega\ \left|U_i(-\Omega)\right|^2\ \left|V_s(\Omega)\right|^2,$$
$$\gamma = \int d\Omega\ \left|U_s(\Omega)\right|^2\ \left|V_s(\Omega)\right|^2. \tag{2.40}$$

We can obtain simplified expressions for the visibility in two extreme but highly important cases: the low ($G \ll 1$) and high ($G \gg 1$) parametric gain regimes.

- **Low parametric gain regime**

  In this regime, the gain σL is very small, thus we can safely write $\Gamma \sim i\frac{\Delta_s}{2}$. The Bogoliubov functions $U_{s,i}$ and $V_{s,i}$ can be written as

  $$U_{s,i}(\Omega) = \exp\left[i\frac{k_{s,i}L}{2}\right], \tag{2.41}$$

  $$V_{s,i}(\Omega) = -i\sigma L\, \mathrm{sinc}(\frac{\Delta_s L}{2}) \exp\left[i\frac{\Delta_s L}{2}\right]. \tag{2.42}$$

  In this case the visibility of the interference fringes gives a linear relationship on $|r_i|$, that is

  $$V = \frac{2|r_s|}{1+|r_s|^2}|r_i|. \tag{2.43}$$

  This linear dependence on the reflectivity r_i is shown in Fig. 2.9 as the blue curve.

- **High parametric gain regime**

  In this regime, the σL is large and the parametric gain is greater than one ($G > 1$). We need to consider the full expressions of

the Bogoliubov functions $U_{s,i}$ and $V_{s,i}$ (see Eqs. (2.23) and (2.24)). The visibility in this case is

$$V = \frac{2|r_s|}{|r_i|^2 + |r_s|^2}|r_i|. \tag{2.44}$$

Fig. 2.9 shows this nonlinear dependence on the reflectivity r_i for a high value of the gain, $G = 4$, as the red curve.

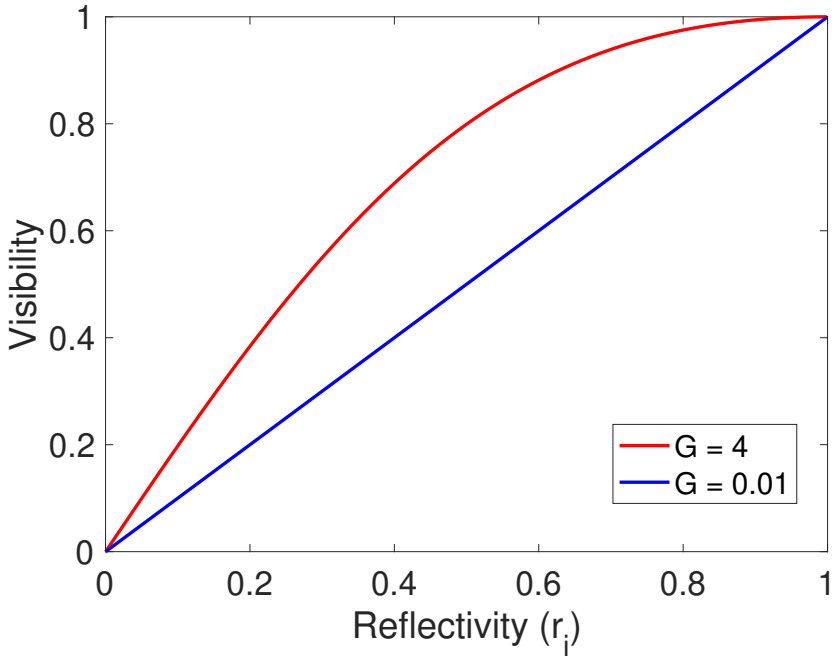

Figure 2.9: Visibility of the interference fringes as a function of the idler reflectivity (r_i) for different values of the parametric gain in an SU(1,1) nonlinear interferometer. The blue solid line correspond to $G = 0.01$ (low parametric gain regime). The red solid line corresponds to $G = 4$ (high parametric gain regime).

2.3 Quantum description

Quantum analysis of an interferometer based on the induced coherence effect

A sketch of an interferometer based on induced coherence is shown in Fig. 2.10. The pump beam illuminates two identical second-order nonlinear crystals (NLC_1 and NLC_2) and paired photons emerge from both crystals (signal s_1 and idler i_1 from NLC_1; signal s_2 and idler i_2 from NLC_2). The idler i_1 interacts with an object with reflectivity $r_i(\Omega)$ and is then injected in NLC_2. The total distance travelled by i_1 before reaching NLC_2 is z_i. Both idler photons i_1 and i_2 are made to be indistinguishable.

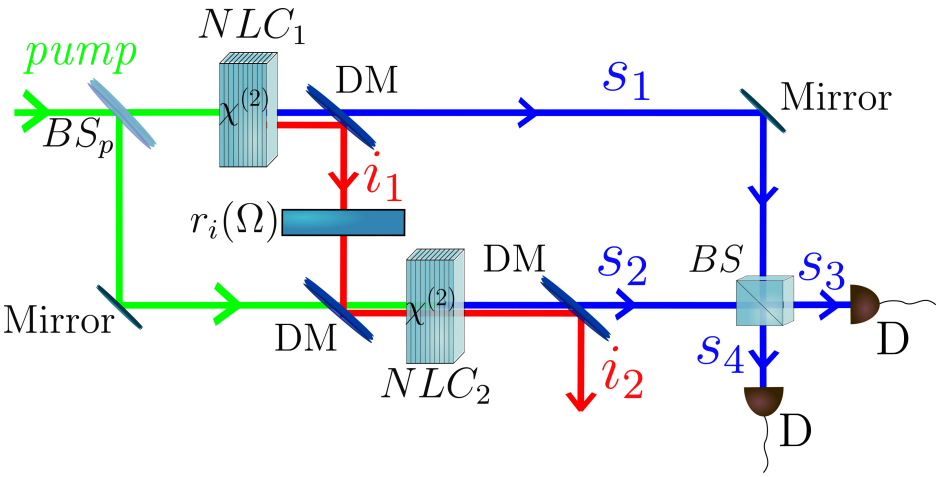

Figure 2.10: Sketch of an nonlinear interferometer based on the induced coherence effect.

The relationship between the input annihilation operators $\hat{b}_s$ and $\hat{b}_i$ and the output operators $\hat{a}_{s_1}$ and $\hat{a}_{i_1}$ of the signal and idler beams generated after NLC_1 is described by the Bogoliubov transformation

$$\hat{a}_{s_1}(\Omega) = U_s(\Omega)\hat{b}_s(\Omega) + V_s(\Omega)\hat{b}_i^{\dagger}(-\Omega), \tag{2.45}$$

$$\hat{a}_{i_1}(\Omega) = U_i(\Omega)\hat{b}_i(\Omega) + V_i(\Omega)\hat{b}_s^{\dagger}(-\Omega). \tag{2.46}$$

The expressions for $U_{s,i}$ and $V_{s,i}$ are the ones shown in Eqs. (2.23) and (2.24). The transformations for the operators $\hat{a}_{i_1}$ and $\hat{a}_{s_1}$ accounting for propagation and loss read

$$\hat{a}_{i_1}(\Omega) \Longrightarrow r_i(\Omega)\hat{a}_{i_1}(\Omega)\exp\left[i\varphi_i(\Omega)\right] + \hat{f}_i(\Omega), \tag{2.47}$$

$$\hat{a}_{s_1}(\Omega) \Longrightarrow \hat{a}_{s_1}(\Omega)\exp\left[i\varphi_{s_1}(\Omega)\right], \tag{2.48}$$

where $\varphi_{s_1,i}(\Omega) = (\omega^0_{s,i} + \Omega)z_{s_1,i}/c$ and $\hat{f}_i$ is an operator that fulfills the commutation relation $[\hat{f}_i(\Omega), \hat{f}_i^\dagger(\Omega')] = [1 - |r_i(\Omega)|^2]\,\delta(\Omega - \Omega')$.

The parametric down-conversion process occurring in the second nonlinear crystal is characterized by the Bogoliubov transformation for the signal s_2 beam as

$$\hat{a}_{s_2}(\Omega) = U_s(\Omega)\hat{c}_s(\Omega) + V_s(\Omega)\hat{a}^\dagger_{i_1}(-\Omega), \tag{2.49}$$

taking into account propagation along a distance $z_{s_2} = z_{s_1} + \Delta z$

$$\hat{a}_{s_2}(\Omega) \Longrightarrow \hat{a}_{s_2}(\Omega)\exp\left[i\varphi_{s_2}(\Omega)\right], \tag{2.50}$$

where $\varphi_{s_2}(\Omega) = (\omega^0_{s_2} + \Omega)z_{s_2}/c$ and Δz is the optical path difference travelled by s_2. Finally we can write

$$\begin{aligned}
&\hat{a}_{s_2}(\Omega) = U_s(\Omega)\hat{c}_s(\Omega) + \\
&+r_i^*(-\Omega)V_s(\Omega)U_i^*(-\Omega)\exp[-i\,\varphi_i(-\Omega)]\,\hat{b}_i^\dagger(-\Omega) + \\
&+r_i^*(-\Omega)V_s(\Omega)V_i^*(-\Omega)\exp[-i\,\varphi_i(-\Omega)]\,\hat{b}_s(\Omega) + \\
&+V_s(\Omega)\hat{f}_i^\dagger(-\Omega).
\end{aligned} \tag{2.51}$$

Signal photons s_1 and s_2 are overlapped in a beam splitter BS and the degree of interference between both waves is the quantity measured at detector D. The total distance travelled by signal s_1 is z_{s_1}, and z_{s_2} is the distance travelled by signal s_2 before reaching the beam splitter. At the beam splitter, the input-output operators relationship between input operators, $\hat{a}_{s_1}$ and $\hat{a}_{s_2}$, and output operators, $\hat{a}_{s_3}$ and $\hat{a}_{s_4}$, are

$$\begin{aligned}
\hat{a}_{s_3}(\Omega) &= r\hat{a}_{s_1}(\Omega) + t\hat{a}_{s_2}(\Omega) \\
\hat{a}_{s_4}(\Omega) &= t\hat{a}_{s_1}(\Omega) + r\hat{a}_{s_2}(\Omega)
\end{aligned} \tag{2.52}$$

where $r = 1/\sqrt{2}$ is the reflection coefficient of the BS, and $t = i/\sqrt{2}$ is its transmission coefficient.

The spectrum of signal photons measured in one output port of the BS is

$$S(\Omega) = \left\langle \hat{a}^{\dagger}_{s_3}(\Omega)\, \hat{a}_{s_3}(\Omega) \right\rangle = \left[1 - |r_i(\Omega)|^2\right] |V_s(\Omega)|^2 + \\ + \Big| V_s(\Omega) \exp[i\, \varphi_{s_1}(\Omega)] + \\ + r_i^*(-\Omega) V_s(\Omega) U_i^*(-\Omega) \exp[-i\, \varphi_i(-\Omega) + i\varphi_{s_2}(\Omega)] \Big|^2. \tag{2.53}$$

First-order correlation function between signal photons s_1 and s_2

We are also interested in calculating the normalized first-order correlation function $g^{(1)}_{s_1,s_2}$ between signal photons generated in the first nonlinear crystal (with operator $\hat{a}_{s_1}$) and signal photons generated in the second nonlinear crystal (with operator $\hat{a}_{s_2}$). The maximum value of the first-order correlation function takes place when $z_{s_1} = z_{s_2} + z_i$, and this is the case we consider here. We have

$$g^{(1)}_{s_1,s_2} = \frac{\left| \langle \hat{a}^{\dagger}_{s_1}(t) \hat{a}_{s_2}(t) \rangle \right|}{\sqrt{\langle \hat{a}^{\dagger}_{s_1}(t)) \hat{a}_{s_1}(t) \rangle} \sqrt{\langle \hat{a}^{\dagger}_{s_2}(t) \hat{a}_{s_2}(t) \rangle}}. \tag{2.54}$$

The flux rate of signal photons s_1 is

$$\langle \hat{a}^{\dagger}_{s_1}(t) \hat{a}_{s_1}(t) \rangle = \frac{1}{2\pi} \int d\Omega \Big| V_s(\Omega) \Big|^2. \tag{2.55}$$

The flux rate of signal photons s_2 is

$$\langle \hat{a}^{\dagger}_{s_2}(t) \hat{a}_{s_2}(t) \rangle = \frac{1}{2\pi} \int d\Omega \Big| V_s(\Omega) \Big|^2 \Big[1 + |r_i|^2 \Big| V_i(-\Omega) \Big|^2 \Big]. \tag{2.56}$$

The cross-correlation term is

$$\langle \hat{a}^{\dagger}_{s_1}(t) \hat{a}_{s_2}(t) \rangle = \frac{r_i^*}{2\pi} \int d\Omega \Big| V_s(\Omega) \Big|^2 U_i^*(-\Omega) \tag{2.57}$$

The first-order correlation function can be written as

$$g^{(1)}_{s_1,s_2} = \frac{|r_i| \left| \int d\Omega \left|V_s(\Omega)\right|^2 U_i^*(-\Omega) \right|}{\sqrt{\int d\Omega \left|V_s(\Omega)\right|^2} \sqrt{\int d\Omega \left|V_s(\Omega)\right|^2 \left[1 + |r_i|^2 \left|V_i(-\Omega)\right|^2\right]}}. \quad (2.58)$$

In the low parametric gain regime, $|U_i| \sim 1$ and $|V_s(\Omega)|^2 \ll 1$. Moreover we can safely assume that $U_i(\Omega)$ is constant over the bandwidth determined by the function $V_s(\Omega)$. In this case we obtain [9]

$$g^{(1)}_{s_1,s_2} = |r_i|. \quad (2.59)$$

In the low parametric gain regime the degree of first-order coherence corresponds to the visibility of the interference pattern observed in one output port of the interferometer. This linear dependence on the reflectivity r_i is shown in Fig. 2.11 (blue line).

In all other cases we need to consider the full expression given in Eq. (2.58). Except in the case of low parametric gain regime considered above, the degree of first-order coherence does not correspond to the visibility of the interference pattern, although it can be obtained from its measurement (see Appendix D for a detailed explanation). The reason for this is that the flux rates of signal photons s_1 and s_2 are not equal. One example of the nonlinear dependence on the reflectivity r_i is shown in Fig. 2.11 (red line). This shape is qualitatively very similar to the ones obtained using the single-mode approximation [29, 52].

2.3.2 Single-mode approximation

Some of the results presented before can also be well described qualitatively using the single-mode approximation ($\Omega = 0$). We can obtain an expression for the visibility of the interference fringes in an SU(1,1) nonlinear interferometer equivalent to Eq. (2.39), that is

$$V = \frac{2|r_s||r_i||U_1||U_2||V_1||V_2|}{(1-|r_i|^2)|V_2|^2 + |r_i|^2|U_1|^2|V_2|^2 + |r_s|^2|U_2|^2|V_1|^2}, \quad (2.60)$$

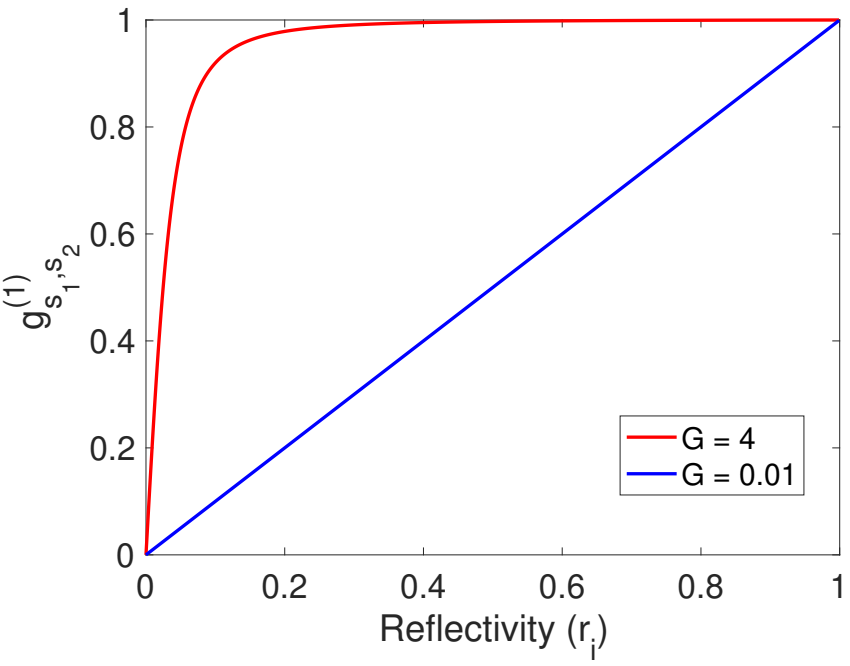

Figure 2.11: Degree of first-order coherence as a function of the idler reflectivity (r_i) for different values of the parametric gain in an interferometer based on induced coherence. The blue solid line correspond to $G = 0.01$ (low parametric gain regime). The red solid line corresponds to $G = 4$ (high parametric gain regime).

where U_1 and V_1 refer to the first pass by the nonlinear crystal and U_2 and V_2 to the second pass. If we write $|V_j| = \sinh(G_j)$, $|U_j| = \cosh(G_j)$ and we make use of $|U_j|^2 - |V_j|^2 = 1$ $(j = 1, 2)$ [48], then

$$V = \frac{0.5 \times |r_s||r_i|\left[\sinh^2(G_1+G_2) - \sinh^2(G_1-G_2)\right]}{\sinh^2(G_2) + |r_s|^2\sinh^2(G_1) + (|r_s|^2+|r_i|^2)\sinh^2(G_1)\sinh^2(G_2)}. \tag{2.61}$$

We consider two important limits. First, in the low parametric gain regime, the values of $G_{1,2}$ are very small, so $\sinh(G_j) \sim G_j$ and

$G_1^2 G_2^2 \ll G_1^2, G_2^2$. We thus have

$$V = \frac{2|r_s| G_1 G_2}{G_2^2 + |r_s|^2 G_1^2} \; |r_i|, \tag{2.62}$$

which corresponds to the expected linear relationship on $|r_i|$. For $G_1 = G_2$ this is Eq. (2.43).

Second, in the very high parametric gain regime, when the difference of gains is small, $\sinh^2(G_1 + G_2) \sim \exp[2(G_1 + G_2)]/4 \gg \sinh^2(G_1 - G_2)$ and $\sinh^2(G_1)\sinh^2(G_2) \sim \exp[2(G_1 + G_2)]/16 \gg \sinh^2(G_1), \sinh^2(G_2)$. The visibility is

$$V = \frac{2|r_s||r_i|}{|r_s|^2 + |r_i|^2}. \tag{2.63}$$

Notice two important points for the limit of very high parametric gain regime, when the difference of gains is not very large: i) The visibility does not depend on the gain, and ii) For $|r_s| = |r_i|$ the visibility is 1.

2.3.3 Quantum analysis of a nonlinear interferometer in the Schrödinger picture

SU(1,1) nonlinear interferometer

In the Schrödinger picture, the input state of signal and idler photons evolve along the the nonlinear crystal using a phenomenological Hamiltonian. For the case of parametric down-conversion, the Hamiltonian describes the process in which the nonlinear medium absorbs a pump photon and two down-converted photons are generated. The Hamiltonian operator is written as

$$\hat{\mathcal{H}}_j = \hbar(g_j \hat{a}_{\mathrm{s}}^\dagger \hat{a}_{\mathrm{i}}^\dagger + g_j^* \hat{a}_{\mathrm{s}} \hat{a}_{\mathrm{i}}), \tag{2.64}$$

where $j = 1, 2$ refers to the first and the second nonlinear crystals where the interactions take place, and the coupling constants g_j are defined as

$$g_j = |g| \exp(i\varphi_{\mathrm{p}_j}). \tag{2.65}$$

2.3 Quantum description

The losses introduced by the object placed in the path of the idler i_1 are modeled considering a beam splitter with reflection and transmission coefficients, r and t, respectively. The relation between the input $|\Psi_{in}\rangle$ and the output state $|\Psi_{out}\rangle$ is obtained through the unitary transformation T defined as [53–55]

$$\begin{aligned} T = \exp\left(-\frac{i\hat{H}_2\tau}{\hbar}\right) \exp\left(\gamma(\hat{a}_0^\dagger \hat{a}_\mathrm{i} + \hat{a}_\mathrm{i}^\dagger \hat{a}_0)\right) \times \\ \times \exp\left(i\varphi_\mathrm{s}\hat{a}_\mathrm{s}^\dagger \hat{a}_\mathrm{s} + i\varphi_\mathrm{i}\hat{a}_\mathrm{i}^\dagger \hat{a}_\mathrm{i}\right) \exp\left(-\frac{i\hat{\mathcal{H}}_1\tau}{\hbar}\right), \end{aligned} \tag{2.66}$$

where τ is the interaction time. Notice that the transformation T is essentially the product of four exponential terms. The first term represents generation of photons in the second nonlinear crystal. The second term stand for the losses experienced by the idler i_1, with $\tan(\gamma) = r/t$. a_0 is the annihilation operator associated to the *lossy* output port. The third term corresponds to the propagation of the signal s_1 and the idler i_1, with $\varphi_{s,i}$ being the phases acquired in free propagation by experienced by both waves. Substituting the expressions of the Hamiltonian [Eq. (2.64)], the unitary transformation can be rewritten as

$$\begin{aligned} T = \exp\left[-i\tau(g_2\hat{a}_\mathrm{s}^\dagger \hat{a}_\mathrm{i}^\dagger + g_2^*\hat{a}_\mathrm{s}\hat{a}_\mathrm{i})\right] \exp\left[\gamma(\hat{a}_0^\dagger \hat{a}_\mathrm{i} + \hat{a}_\mathrm{i}^\dagger \hat{a}_0)\right] \times \\ \times \exp\left[i\varphi_\mathrm{s}\hat{a}_\mathrm{s}^\dagger \hat{a}_\mathrm{s} + i\varphi_\mathrm{i}\hat{a}_\mathrm{i}^\dagger \hat{a}_\mathrm{i}\right] \exp\left[-i\tau(g_1\hat{a}_\mathrm{s}^\dagger \hat{a}_\mathrm{i}^\dagger + g_1^*\hat{a}_\mathrm{s}\hat{a}_\mathrm{i})\right]. \end{aligned} \tag{2.67}$$

If the input state is the vacuum $|\Psi_{in}\rangle = |0\rangle_\mathrm{s} |0\rangle_\mathrm{i} |0\rangle_0$, the output state is $|\Psi_{out}\rangle = T |\Psi_{in}\rangle$. In the Fock state basis the output quantum state

reads

$$|\Psi_{out}\rangle = \frac{1}{U_1^2}\sum_{q=0}^{\infty}\sum_{n=0}^{q}\sum_{k=q-n}^{\infty}\sum_{l=0}^{q-n}\left[\frac{V_1\exp[i(\varphi_{\rm i}+\varphi_{\rm s})]}{U_1}\right]^k\left[\frac{V_2}{U_1}\right]^n$$
$$\times\left[\frac{-V_2^*}{U_1}\right]^{k+n-q}\binom{k}{l}^{\frac{1}{2}}\binom{k}{q-n}^{\frac{1}{2}}\binom{k-l}{k+n-q}^{\frac{1}{2}}\binom{q}{n}^{\frac{1}{2}}\binom{q-l}{n}^{\frac{1}{2}}$$
$$\times r^{k-l}t^l U_1^{l-2(q-n)}\,|q\rangle_{\rm s}\,|q-l\rangle_{\rm i}\,|l\rangle_0\,, \tag{2.68}$$

where $U_1 = U_2 = \cosh(\tau|g|)$ and $V_j = -i\sinh(\tau|g|)\exp(i\varphi_{\rm p_j})$. The strength of the interaction is given by the value of $\tau|g|$. φ_{p_j} are the phases of the pump beam in the first and second nonlinear crystals.

Despite the algebraic difficulty shown in Eq. (2.68), the Schrödinger picture is quite useful to get an intuitive idea of the physical meaning of the final state in the low parametric gain regime. In this regime the functions $U_{1,2}$ and V_j are $U_1 = U_2 = 1$ and $V_j = -i\tau|g|\exp(i\varphi_{\rm p_j})$. For the sake of simplicity, let us consider that there is no loss in the idler path, so the transmission coefficient is $t = 0$ and therefore only terms with index $l = 0$ are different from zero. To keep the expansion in Eq. (2.68) to first order on the strength of the interaction, we need to consider only the terms with indexes $q = 1$, $l = 0$, $k = 0$, $n = 1$ and $q = 1$, $l = 0$, $k = 1$, $n = 0$. The output quantum state in the low parametric gain regime reads

$$|\Psi_{out}\rangle \sim |vac\rangle_{s,i,0} + \Big\{V_1\exp\left[i(\varphi_s+\varphi_i+\varphi_r)\right] + V_2\Big\}\,|1\rangle_s\,|1\rangle_i\,|0\rangle_0\,, \tag{2.69}$$

where φ_r is the phase introduced by reflection from the phase object. This is the quantum state usually considered in the analysis of experiments working with SU(1,1) interferometers in the low parametric gain regime [10, 17]. Inspection of the quantum state shows that the probability to observe pairs of signal-idler photons after the second pass by the nonlinear crystal is the result of interference between two options:

- The signal-idler pairs are generated in the first nonlinear crystal, or in the first pass by a single nonlinear crystal. Taking into account the phase of the pump during the first pass by the nonlinear crystal, the reflectivity of the sample (we are considering a phase object), and the path traversed by both photons, that provide phases φ_s and φ_i, the quantum amplitude of this option is: $rV_1 \exp\left[i(\varphi_s + \varphi_i)\right]$.
- The signal-idler pairs are generated in the second nonlinear crystal, or in the second pass by a single nonlinear crystal. Taking into account the phase of the pump during the second pass by the nonlinear crystal, the quantum amplitude of this second option is V_2.

The probability to detect a signal photon is maximum when

$$\Delta\varphi_p = \varphi_{p_2} - \varphi_{p_1} = \varphi_r + \varphi_s + \varphi_i, \tag{2.70}$$

and the probability is minimum when

$$\Delta\varphi_p = \varphi_r + \varphi_s + \varphi_i + \pi. \tag{2.71}$$

If $|V_2| = |V_1|$ the probability goes from zero to a maximum value.

Nonlinear interferometer based on induced coherence

For an interferometer based on induced coherence, the general expression of the transformation T reads

$$T = \exp\left[-\frac{i\hat{\mathcal{H}}_2\tau}{\hbar}\right] \exp\left[\gamma(\hat{a}_0^\dagger \hat{a}_\mathrm{i} + \hat{a}_\mathrm{i}^\dagger \hat{a}_0)\right] \exp\left[-\frac{i\hat{\mathcal{H}}_1\tau}{\hbar}\right]. \tag{2.72}$$

For the sake of simplicity, we neglect here the role of phases acquired during propagation of all waves. Substituting the expressions for the Hamiltonian [see Eq. (2.64)] we can write

$$\begin{aligned} T = &\exp\left[-i\tau(g_2 \hat{a}_{s_2}^\dagger \hat{a}_\mathrm{i}^\dagger + g_2^* \hat{a}_{s_2} \hat{a}_\mathrm{i})\right] \exp\left[\gamma(\hat{a}_0^\dagger \hat{a}_\mathrm{i} + \hat{a}_\mathrm{i}^\dagger \hat{a}_0)\right] \\ &\times \exp\left[-i\tau(g_1 \hat{a}_{s_1}^\dagger \hat{a}_\mathrm{i}^\dagger + g_1^* \hat{a}_{s_1} \hat{a}_\mathrm{i})\right]. \end{aligned} \tag{2.73}$$

The output quantum state is obtained by applying this transformation to an initial state that considers all the modes in the vacuum state $|\Psi_{in}\rangle = |0\rangle_{s_1} |0\rangle_{s_2} |0\rangle_{\mathrm{i}} |0\rangle_0$. The output quantum state reads

$$|\Psi_{out}\rangle = \sum_{k,m=0}^{\infty} \sum_{n=0}^{k} t^n r^{k-n} \frac{1}{U_1 U_2^{n+1}} \left[\frac{V_1}{U_1}\right]^k \left[\frac{V_2}{U_2}\right]^m \binom{k}{n}^{\frac{1}{2}} \binom{n+m}{n}^{\frac{1}{2}} \times |k\rangle_{\mathrm{s1}} |m\rangle_{\mathrm{s2}} |n+m\rangle_{\mathrm{i}} |k-n\rangle_0 \,. \tag{2.74}$$

In the low parametric gain regime, the functions $U_{1,2}$ and V_j are $U_{1,2} = 1$ and $V_j = -i\tau|g| \exp\{i\varphi_{\mathrm{p}_j}\}$ and the output quantum state described in Eq. (2.74) can be written as

$$\begin{aligned} \left|\bar{\Psi}_{out}\right\rangle &= |vac\rangle_{s_1,s_2,i,0} + V_2 |0\rangle_{s_1} |1\rangle_{s_2} |1\rangle_i |0\rangle_0 + \\ &+ V_1 \big[t |1\rangle_{s_1} |0\rangle_{s_2} |1\rangle_i |0\rangle_0 + r |1\rangle_{s_1} |0\rangle_{s_2} |0\rangle_i |1\rangle_0 \big], \end{aligned} \tag{2.75}$$

which is the typical state considered in the literature for induced coherence experiments working in the low parametric gain regime [9, 10]. Inspection of Eq. (2.75) shows that when $r = 0$ (no loss in the idler path), there is quantum interference between two options: the paired signal-idler photons are generated in the first nonlinear crystal (quantum amplitude V_1) or in the second nonlinear crystal (quantum amplitude V_2). If the idler photon generated in the first nonlinear crystal is blocked ($t = 0$), there is no quantum interference between signal photons.

The Schrödinger picture gives an intuitive explanation of the phenomena considered in the low parametric gain regime. However, when we consider multimode systems (including the frequency, for instance) or go to the high parametric gain regime, the use of the Schrödinger picture becomes very complicated and inconvenient, since one needs to include higher order terms that are cumbersome to handle. The Schrödinger picture losses its intuitive appealing. This is why it is much more convenient and easy to use a quantum analysis based on the Heisenberg picture.

CHAPTER

THREE

OPTICAL COHERENCE TOMOGRAPHY (OCT) IN THE LOW PARAMETRIC GAIN REGIME

This chapter puts forward a new application of nonlinear interferometers in the field of imaging: Optical Coherence Tomography (OCT). In 2017 (corresponding paper published at the beginning of 2018 [56]) we demonstrated the feasibility of doing OCT making use of an interferometer based on induced coherence (*Mandel-type* interferometer). A few months later Paterova *et al.* [16] presented the same idea using an SU(1,1) interferometer (*Yurke-type* interferometer). Both schemes worked in the low parametric gain regime of down-conversion. The first *standard* OCT schemes were introduced in the early 1990s [2,3]. In this chapter we give a detailed analysis of the OCT introduced in 2018 [56]. We analyze its working principle, the experimental details, the pros and cons of our approach and the potential main applications are put forward. The first section of this chapter revisits the

main characteristics of *standard* OCT for the sake of comparison with the novel scheme presented here and in the following chapter. The last section of this chapter is devoted to discuss key potential benefits of the novel OCT scheme when compared with the standard counterpart, as well as the limitations that must be overcome before it can be considered a viable OCT alternative solution.

3.1 Introduction to *standard* optical coherence tomography

Optical Coherence Tomography (OCT) is a noninvasive imaging technique that allows cross-sectional and high axial resolution tomographic imaging of a sample by measuring the light reflected from it. It was first introduced in 1991 and the name of this novel technique was given by Huang *et al.* [2]. The same imaging method was demonstrated the very same year by Dresel *et al.* [3]. The main difference between both research works was that Huang *et al.* imaged the retina in their implementation of OCT, while Dresel *et al.* imaged a rough surface. Imaging of the retina turns out to be one of the main and most successful applications of OCT. However the fundamental working principle in both papers is the same.

Since its invention and first implementation in 1991, OCT has become a widespread highly successful imaging technique[1] applied in many different areas of science and technology, from medicine [4] to art conservation studies [5, 6]. The first commercial OCT instrument was developed by Carl Zeiss in 1994 for ophthalmology. From then on this technology has been embraced by the ophthalmic community becoming the gold standard for live retinal imaging today.

Replacing tissue excision, which is highly invasive and susceptible to sampling errors, by minimally invasive techniques such as magnetic resonance imaging (MRI), position emission tomography (PET) or X-ray computed tomography (CT) has revolutionized the

[1] For a daily basis update of information on OCT see *www.octnews.org*.

diagnostic medicine in the last decades. Thanks to many different advances in medical devices, OCT has joined these imaging systems, and is nowadays also applied to image internal body organs by using catheters or other imaging probes. OCT is increasingly becoming a key tool for non-invasive diagnosis, finding new applications in areas such as cardiology or gastroenterology.

Before entering into a detailed explanation of the working principle of OCT, let us consider why it is an important and successful technology in comparison with other medical imaging techniques. The key advantage of OCT is that it fills the gap between axial resolution and penetration depth between confocal microscopy and ultrasound. This can be clearly seen in Fig. 3.1.

On the one hand, confocal microscopy has submicron axial resolution but a poor image penetration depth of less than a millimeter in most biological tissues. On the other hand, standard clinical ultrasound attain huge penetration depth ($\sim$ 10 cm) but shows a very limited axial resolution. Higher frequency ultrasound gains resolution but reduced image penetration. OCT constitutes the trade-off between both techniques: the axial resolution ranges from 1 to 15 micrometers and the imaging depth is limited to $2-3$ millimeters due to optical scattering.

OCT can be called low-coherence interferometry. *Interferometry* is the tool to measure the magnitude and echo time delay of the backscattered light from a sample. The *low-coherence* (broad bandwidth) nature of the source of light allows to obtain an axial resolution of just a few $\sim \mu$m, even submicron resolution in non-commercial advanced systems. To do so, OCT uses a Michelson interferometer (Fig. 3.2). Light coming from a broadband light source is divided by a beam splitter forming the two arms of the interferometer. One light beam constitutes the *reference* beam and the other, which illuminates the sample, is the *object* beam. The output signal that is measured results from the interference of the reference beam with the object beam after being reflected from the sample.

Interferometry assesses the electric field rather than the intensity

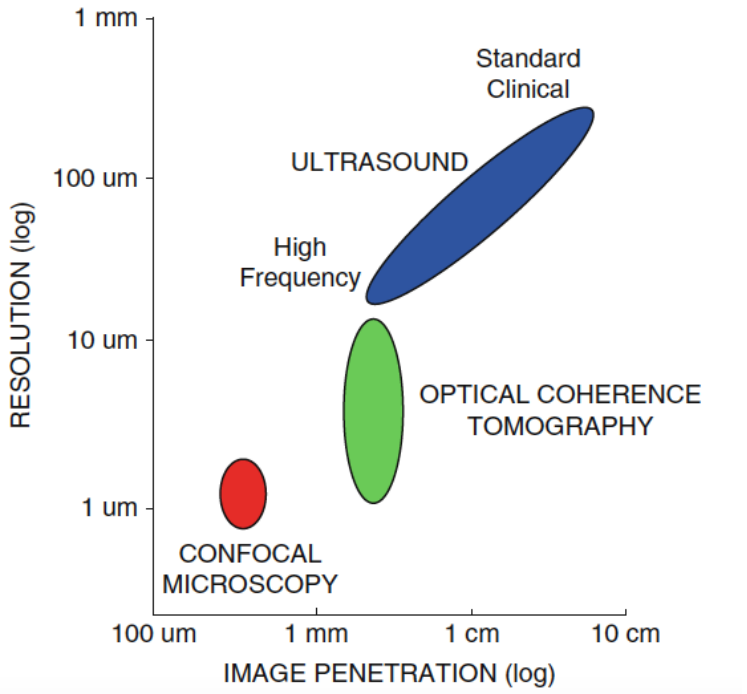

Figure 3.1: Graphical comparison between optical coherence tomography, confocal microscopy and ultrasound techniques in terms of penetration depth and axial imaging resolution. Image taken from *Chapter 1* of Ref. [4].

of the light wave, but the detector measures the output intensity. The output field of an interferometer is the sum of the reference and object electric fields (E_r and E_o), and the intensity is proportional to the square of the electric field. The output intensity I_0 is

$$I_0 = |E_r|^2 + |E_o|^2 + 2E_rE_o\cos(2k\Delta L), \tag{3.1}$$

where ΔL is the path length difference between the reference and object arms of the interferometer and k is the frequency-dependent wavenumber.

3.1 Introduction to *standard* optical coherence tomography

In the next section we will give a detailed mathematical analysis of OCT. However, for the sake of simplicity, let us consider here the case of a sample formed by a layer of refractive index n and thickness d embedded between two facets with reflectivities r_1 and r_2 (see Fig. 3.2). The reflection coefficient r_i under normal incidence is

$$r_1 = \frac{n - n_0}{n + n_0}, \qquad r_2 = \frac{n_0 - n}{n_0 + n}. \tag{3.2}$$

The sample is embedded between media with refractive index n_0. We assume that the refractive index n and the reflectivities $r_{1,2}$ do not depend noticeable on the frequency. The electric field coming from the reference arm is $E_r = E_i/\sqrt{2}$ where E_i is the input electric field. If the reflectivity of the facets that form the layers is very small ($|r_{1,2}|^2 \ll 1$ and $|t_1|^2 \sim 1$), which is the case in most situations of interest such as biological samples, we can approximate the object beam as a superposition of multiple beams reflected from different longitudinal positions inside the sample as

$$E_o = \frac{iE_i}{\sqrt{2}} \left\{ r_1 + r_2 \exp\left[2i \frac{\omega_0 + \Omega}{c} nd \right] \right\}. \tag{3.3}$$

OCT measures *directly* the reflectivity of each layer of the object and its position. The key factor that allows to distinguish the position of different layers is the low-coherence of the light source. Indeed the axial resolution of the OCT system depends on the coherence length of the source, i.e. the shorter the coherence length, the better the axial resolution.

The general expression of the coherence length l_c is [57]

$$l_c = \frac{4 \ln 2}{n\pi} \frac{\lambda_0^2}{\Delta\lambda_{FWHM}}, \tag{3.4}$$

where $\lambda_0 = 2\pi c/\omega_0$ is the central wavelength of the light source, $\Delta\lambda_{FWHM}$ is the bandwidth at full width half maximum and n is the refractive index of the medium at a certain depth. Eq. (3.4)

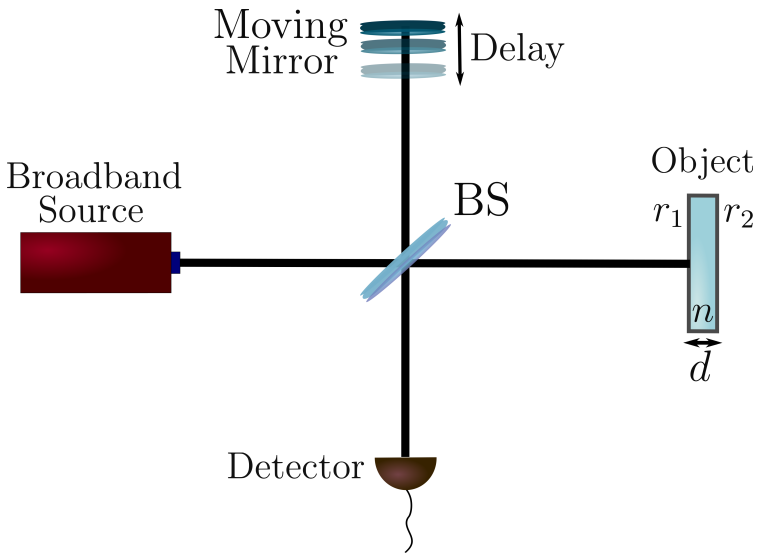

Figure 3.2: General scheme of an optical coherence tomography (OCT) setup. $r_{1,2}$ are the reflectivities of the object at the input and the output facets, respectively. d is the thickness of the sample and n its refractive index. The mirror in the reference arm can be moved changing the path length traversed by the reference beam, so the path length difference between the reference and object beams.

shows clearly that the broader the bandwidth, the smaller is the coherence length, and so the better is the axial resolution of OCT. The most common and easy way to generate broadband light is by using continuous-wave (CW) light with extremely low-coherence.

The visibility of the interference fringes measured at the output of the interferometer for a specific layer inside the object depend on the reflectivity at this specific layer, as

$$V = \frac{I_{max} - I_{min}}{I_{max} + I_{min}} = \frac{2|r_i|}{1 + |r_i|^2}, \tag{3.5}$$

where I_{max} and I_{min} are the maximum and minimum intensities measured changing the path length traversed by the reference beam with

the help of a movable mirror. For each axial measurement, the two interfering waves (the reference and the object beams) show coherence only at a certain axial position, and the low-coherence nature of the source provides the resolution required to determine the position of the reflectivity measurement. The interference can be observed and measured in two domains: the time-domain (TD) and the spectral or Fourier-domain (FD), giving name to the two main modalities of OCT. In TD-OCT, we measure the total intensity at the detection stage $I_d(z)$ as a function of the position z of the movable reference mirror. Its displacement is used to reconstruct the sample reflectivity profile. Interference is only observed if the two arms of the interferometer are balanced up to the coherence length of the light source. The main disadvantage of this time domain approach is that requires relatively complex mechanical and optical elements to scan 10 picosecond delays at kilohertz rates to achieve real-time imaging.

In FD-OCT, the intensity $I_d(k)$ is measured as a function of the wavenumber k. This spectrum is the result of the frequency-dependent interference between the reference and object beams [58]. The presence of the sample modulates the spectrum and by Fourier analysis the sample reflectivity profile can be retrieved. The Wiener-Khinchin theorem relates the auto-correlation and the spectral density power, so that the depth profile of the sample can be calculated by Fourier transforming the measured spectra. In this approach there is no need to scan the reference mirror position, thus the imaging speed is dramatically increased. In addition, FD-OCT just requires a single scan so that's why it shows better signal to noise ratio compared to TD-OCT [59].

3.2 Mathematical analysis of *standard* OCT

The main goal of OCT is to reconstruct the reflectivity depth profile of an arbitrary sample from noninvasive measurements using low-

coherence interferometry. To do so, it makes use of a Michelson interferometer as shown in (Fig. 3.2). The broadband light source has a spectral density $\Phi(k)$ characterized with a Gaussian function of the form

$$\Phi(k) = \frac{1}{\sqrt{\pi}B} \exp(-\frac{k^2}{B^2}), \tag{3.6}$$

where $k = \Omega/c$ is the wavenumber deviation from the central wavenumber $k_0 = \omega_0/c$. The function $\Phi(k)$ is normalized so that $\int \Phi(k)dk = 1$. The parameter B is related with the full width half maximum spectral bandwidth $\Delta\lambda_{FWHM}$ of the light source as

$$\Delta\lambda_{FWHM} = \frac{\lambda_0^2\sqrt{\ln(2)}}{\pi}B, \tag{3.7}$$

where λ_0 is the central wavelength of the laser source. It is convenient to write the expressions considering the wavenumber k as the main variable, since we will see that the Fourier transform directly relates this variable to the depth profile of the sample. The input electric field E_i is considered a plane wave written in complex form as

$$E_i = \Phi(k)\exp(ikz). \tag{3.8}$$

The light coming from the source is divided by a 50:50 beam splitter with reflection $r = 1/\sqrt{2}$ and transmission $t = i/\sqrt{2}$ coefficients. The reference beam is reflected back by the reference mirror and travels a total distance of $2z_R$. The object beam interacts with the sample and traverses a total distance of $2z_S = 2(z_R + \Delta L)$, with $2\Delta L$ being the path unbalance between the reference and the object arms of the interferometer.

The object to be analyzed is characterized by its field reflectivity profile along the beam propagation, $r(k)$. For real biological tissues, this is a continuous varying function since the refractive index changes continuously depending on the depth and light source wavelength, $n(z, \lambda)$. For the sake of simplicity, let us consider a series of N-discrete reflections located at different depth inside the sample. In

this scenario, the field reflectivity $r(k)$ can be written as

$$r(k) = \sum_{n=1}^{N} r_{S_n} e^{2ikn(z_{S_n})(z_{S_n} - z_S)}, \tag{3.9}$$

where $r_{S_1}, r_{S_2}...$ are the electric field reflectivities at distances $z_{S_1}, z_{S_2}...$ from the beam splitter, respectively. $n(z_{S_n})$ is the refractive index of the sample at the corresponding depth position z_{S_n}. The power reflectivity is the squared of the electric field reflectivity $R_n = |r_n|^2$. The electric fields coming from the sample and the reference arm of the interferometer are

$$E_R = \frac{E_i}{\sqrt{2}} \exp(2ikz_R), \tag{3.10}$$

$$E_S = \frac{E_i}{\sqrt{2}} r(k) \exp(2ikz_S). \tag{3.11}$$

Finally, both beams recombine at the beam splitter and the interference of both electric fields generates a photocurrent at the detector $I_D(k)$ that is proportional to the square of the sum of the fields

$$\begin{aligned} I_D(k) &= \left\langle |E_R + E_S|^2 \right\rangle = \frac{\Phi(k)}{4}[1 + R_{S_1} + R_{S_2} + ...] + \\ &+ \frac{\Phi(k)}{2} \sum_{n=1}^{N} \sqrt{R_{S_n}} \cos\left(2k(z_R - z_{S_n})\right) + \\ &+ \frac{\Phi(k)}{4} \sum_{n \neq m = 1}^{N} \sqrt{R_{S_n} R_{S_m}} \cos\left(2k(z_{S_n} - z_{S_m})\right). \end{aligned} \tag{3.12}$$

As can be seen in Eq. (3.12), the detector current is composed by three terms:

- *The constant or DC component*: The first term constitutes a constant term independent of the path-length difference. It is mainly composed by the light source wavenumber spectrum and the amplitude is proportional to the sum of the sample reflectivities. It is the largest component of the detector current.

- *The Cross-Correlation components*: This second term is the desired one for doing OCT, because it provides information about the sample reflectors and its axial position. It depends on the spectrum wavenumber and the path difference between the reference arm and the corresponding sample reflector. The amplitude is proportional to the square-root of the sample reflector reflectivity, so it is typically smaller than the DC component.

- *The Auto-Correlation components*: The last term stands for the interference between different sample reflectors. They are undesired terms of the OCT signal, and are generally considered as artifacts. The amplitude of this component depends on the square-root product of the power reflectivities of different sample reflectors. Therefore these terms are smaller than the cross-correlation terms. In any case, one option to remove this undesired information is to use common-path systems, in which the auto-correlation terms are directly the desired OCT signal.

3.2.1 Time-Domain OCT (TD-OCT)

In time-domain OCT (TD-OCT), the detector current $I_D(z_R)$ is measured while the path length of the reference arm z_R is varied in time. In this approach, the reference mirror is translated longitudinally to retrieve the internal sample reflectivity profile. The OCT signal is obtained by integration of Eq. (3.12) over all wavenumber k, so that

$$\begin{aligned} I_D(z_R) &= \frac{1}{4}[1 + R_{S_1} + R_{S_2} + ...] + \\ &+ \frac{1}{2}\sum_{n=1}^{N} \sqrt{R_{S_n}} \cos\left(2k_0(z_R - z_{S_n})\right) e^{-(z_R - z_{S_n})^2 \Delta k^2}. \end{aligned} \tag{3.13}$$

The first term constitutes a DC offset proportional to the sum of the sample reflectivities. The second term depends on the square-root of the power reflectivity of each sample reflector and is modulated

3.2 Mathematical analysis of *standard* OCT

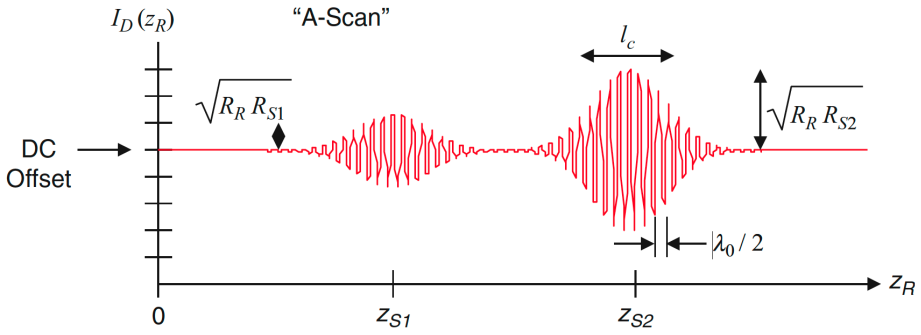

Figure 3.3: Time-domain OCT signal $I_D(z_R)$ as a result of an axial scan of a single layer sample composed by two facets. R_{S_1} and R_{S_2} are the power reflectivities of each facet, z_{S_1} and z_{S_2} are the facet's locations. Figure taken from Ref. [4].

by a cosinusoidal carrier wave centered at the arm length difference between the reference and the object arms.

As an illustration and for the sake of simplicity, let us consider a single layer sample constituted by two low reflectivity facets. The field reflectivity $r(k)$ [Eq. (3.9)] in this case can be written as

$$r(k) = r_{S_1} + r_{S_2} \exp(2ik_0 n_0 d + 2ikn_g d), \tag{3.14}$$

where n_0 is the refractive index of the sample at the central frequency, d is the sample thickness and n_g the group refractive index. Thus the time domain OCT signal [Eq. (3.13)] depending on the reference arm scanning position $I_D(z_R)$ is

$$\begin{aligned} I_D(z_R) &= \frac{1}{4}[1 + R_{S_1} + R_{S_2}] + \\ &+ \frac{1}{2}\sqrt{R_{S_1}} \cos\left(2k_0(z_R - z_{S_1})\right) e^{-(z_R - z_{S_1})^2 \Delta k^2} + \\ &+ \frac{1}{2}\sqrt{R_{S_2}} \cos\left(2k_0(z_R - z_{S_2})\right) e^{-(z_R - z_{S_2})^2 \Delta k^2}. \end{aligned} \tag{3.15}$$

Figure 3.3 shows a typical result of an axial scan for this single layer sample in TD-OCT. When the sample reflectivity profile is con-

volved with the source coherence function, two fringe bursts appear at the layers' unbalancing positions ($z_R - z_{S_n}$) providing the information about the thickness of the sample $d = (z_{S_2} - z_{S_1})/n$. The value of each facet's field reflectivity (r_{S_1} and r_{S_2}) is determined by the amplitude of the fringes.

3.2.2 Fourier-Domain OCT (FD-OCT)

Fourier-domain OCT (FD-OCT) was introduced by Fercher *et al.* in 1995 [58]. The core features of this approach are the same as those of its time domain counterpart: low-coherence interferometry with a broadband light source. However now one measures the spectrum of the signal without scanning the reference mirror. This OCT modality encompasses two main approaches depending on the detection system: swept-source and spectral-domain OCT.

In spectral-domain OCT (SD-OCT), the interference spectrum is measured directly by a detector array placed after a grating (spectrometer) and a high-speed line camera. This method is the one proposed by Fercher in 1995. Because SD-OCT effectively captures the interference spectrum in one scan, it offers a significant sensitivity advantage ($\sim 50 - 100$ times higher) over the temporal domain detection.

In swept-source OCT (SS-OCT), the wavenumber dependent current $I_d(k)$ is measured sequentially by the same detector while changing the wavenumber of the narrowband swept-laser source [60]. This approach does not require a spectrometer and a line scan camera. As a result, it can work over a wider range of wavelengths than cameras do. Furthermore, swept-source OCT is not constrained by camera speed, allowing for faster imaging than spectral-domain OCT. However this technique requires the use of a high-speed sweeping narrow-linewidth source.

In both spectral-domain OCT (SD-OCT) and swept-source OCT (SS-OCT), regardless of the detection system, one captures the spectral density $S(k)$ and processes it using Fourier analysis to reconstruct

the sample's reflectivity profile. The spectral density $S(k)$ of the output beam of the interferometer for an arbitrary reflection coefficient $r(k)$ is

$$S(k) = \frac{\Phi(k)}{4}\left|\exp\big(2i(k_0+k)z_r\big) + r(k)\exp\big(2i(k_0+k)z_s\big)\right|^2. \quad (3.16)$$

Expanding the modulus of Eq. (3.16) and substituting the expression of the field reflectivity $r(k)$ [Eq. (3.9)], the spectral density is written as

$$\begin{aligned} S(k) &= \frac{\Phi(k)}{4}[1 + R_{S_1} + R_{S_2}...] + \\ &+ \frac{\Phi(k)}{2}\sum_{n=1}^{N}\sqrt{R_{S_n}}\cos\left(2k(z_R - z_{S_n})\right) + \\ &+ \frac{\Phi(k)}{4}\sum_{n\neq m=1}^{N}\sqrt{R_{S_n}R_{S_m}}\cos\left(2k(z_{S_n} - z_{S_m})\right). \end{aligned} \quad (3.17)$$

The position of the interfaces and the corresponding reflectivities are obtained by Fourier transforming the spectral density shown in Eq. (3.17) so

$$\begin{aligned} \hat{S}(z) = \mathcal{F}[S(k)] &= \frac{\hat{\Phi}(z)}{4}[1 + R_{S_1} + R_{S_2}...] + \\ &+ \frac{1}{4}\sum_{n=1}^{N}\sqrt{R_{S_n}}\big[\hat{\Phi}\big(2(z_R - z_{S_n})\big) + \hat{\Phi}\big(-2(z_R - z_{S_n})\big)\big] + \\ &+ \frac{1}{4}\sum_{n\neq m=1}^{N}\sqrt{R_{S_n}R_{S_m}}\big[\hat{\Phi}\big(2(z_{S_n} - z_{S_m})\big) + \hat{\Phi}\big(-2(z_{S_n} - z_{S_m})\big)\big], \end{aligned} \quad (3.18)$$

where $\hat{\Phi}(z) = \mathcal{F}[\Phi(k)]$. Analogously to the time domain case, let us consider a single layer sample with two low reflectivity facets. The

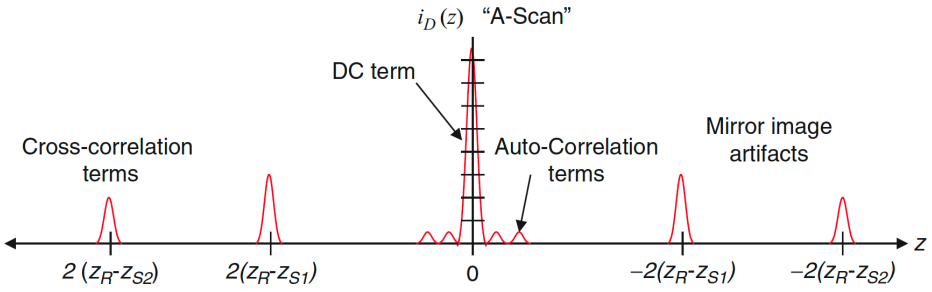

Figure 3.4: Fourier-domain OCT signal $\hat{S}(z)$ as a result of an axial scan of a single layer sample composed by two low reflectivity facets. z_R is the optical path length of the reference arm; z_{S_1} and z_{S_2} are the facet's locations. Figure taken from Ref. [4].

field reflectivity function $r(k)$ of the sample is described in Eq. (3.14). The Fourier-domain OCT signal [Eq. (3.18)] can be written as

$$\begin{aligned}\hat{S}(z) = &\frac{\hat{\Phi}(z)}{4}[1 + R_{S_1} + R_{S_2}] + \\ &+ \frac{1}{4}\sqrt{R_{S_1}}\big[\hat{\Phi}\big(2(z_R - z_{S_1})\big) + \hat{\Phi}\big(-2(z_R - z_{S_1})\big)\big] + \\ &+ \frac{1}{4}\sqrt{R_{S_2}}\big[\hat{\Phi}\big(2(z_R - z_{S_2})\big) + \hat{\Phi}\big(-2(z_R - z_{S_2})\big)\big] + \\ &+ \frac{1}{4}\sqrt{R_{S_1}R_{S_2}}\big[\hat{\Phi}\big(2(z_{S_1} - z_{S_2})\big) + \hat{\Phi}\big(-2(z_{S_1} - z_{S_2})\big)\big].\end{aligned} \tag{3.19}$$

Note that the OCT signal in this case is composed by seven peaks (Fig. 3.4). One DC peak appearing at $z = 0$, three peaks located at $z > 0$ and three more peaks at $z < 0$. The *cross-correlation* peaks, which provide information about the location and reflectivity of the two sides of the sample, appear at a relative position to the reference coordinate z_R that is doubled $2(z_R \pm z_{S_n})$. The square-root of the power reflectivity $\sqrt{R_{S_n}}$ of each layer determines the amplitude of these peaks.

The artifact *auto-correlation* peaks appear nearby the zero path

length position, since the distance between the sample reflectors is typically much smaller than the distance between them and the mirror in the reference arm. The amplitude of these peaks is much smaller than the cross-correlation ones.

3.3 OCT based on induced coherence

In this section we present a *new type* of optical coherence tomography scheme based on the concept of induced coherence[2]. The idea to merge two ideas, OCT and nonlinear interferometers, was first introduced in 2018 [56]. A *proof-of-concept* experiment demonstrated that in addition to obtaining information in the transverse plane of a sample [10] (perpendicular to the beam propagation), it was also possible to do optical sectioning (in the axial direction, along the beam propagation). Three-dimensional images can be obtained without the need to detect the photons that actually interacted with the sample.

The proposed experimental setup (Fig. 3.5) is a nonlinear interferometer based on the concept of induced coherence, using two spatially separated down-converters working in the low parametric gain regime of down-conversion. The sample is placed between the two PDC sources.

There are subtle differences between this novel technique and standard OCT schemes (Fig. 3.6) [61]. In *standard* OCT, the reference and the object light beams have different intensities: $I_0/2$ and $|\tau|^2 I_o/2$, respectively (Fig. 3.6(a)). τ is the field reflectivity (transmissivity) of the sample. The two beams show first-order coherence for a concrete value of the delay between both (Fig. 3.6(b)). The visibility of the interference fringes depends directly on τ [Eq. (3.5)] since both beams have different intensities. Thus OCT performs a measurement of the output intensity that gives the reflectivity of the sample. It does not measure first-order coherence.

On the other hand, in the proposed scheme based on induced

[2]See Section 2.2.2 for a detailed description of the *induced coherence* effect.

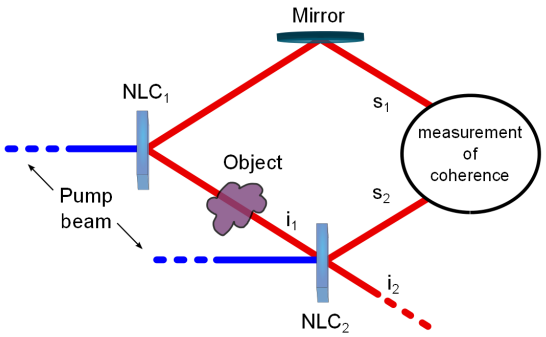

Figure 3.5: Simplified sketch of the nonlinear interferometer based on the concept of induced coherence, aimed at measuring optical sectioning of an object. $NLC_{1,2}$ are nonlinear crystals; s, i refer to the signal and idler photons, with sub-indexes indicating from which crystal they are emitted.

coherence in the low parametric gain regime, the two signal beams that are made to interfere have the same photon flux $N_0/2$ (Fig. 3.6(c)), independently of the reflectivity τ of the sample. Instead, the coherence between both signal beams depends linearly on the losses introduced by the sample (Fig. 3.6(d)). Thus the role of optical coherence is twofold: assessing the desired value of the reflectivity and providing the axial optical sectioning of the sample.

Regarding axial resolution there is no practical advantage nor difference between the standard OCT scheme and the proposed one. In general the broader the bandwidth of the light source, the better the axial resolution. So that, if the bandwidth of the light source used in standard OCT is the same as the bandwidth of the down-converted photons in this novel approach, the axial resolution will be identical.

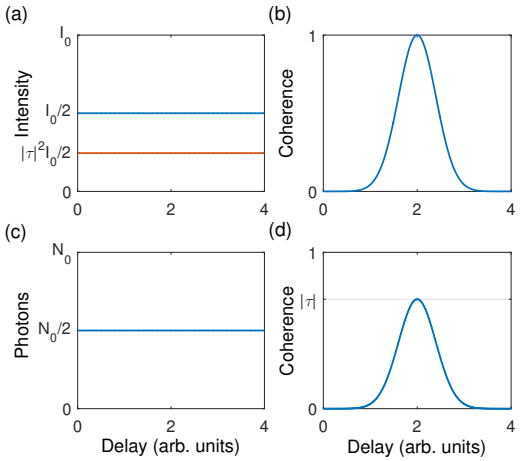

Figure 3.6: Differences in physical principle between an *standard* OCT scheme and the novel configuration based on *induced coherence*. (a, c) Intensity (or photon flux) of the reference and the sample beams of the interferometer. (b, d) Degree of first-order coherence between the reference and sample beams of the interferometer. I_0 is the total intensity and N_0 is the total number of photons propagating through the interferometer. τ is the field reflectivity of the sample.

3.4 Experimental setup

The experimental setup used for observing optical sectioning based on the concept of induced coherence is shown in Fig. 3.7. The pump laser is a high-power continuous-wave (CW) laser Verdi V10 (Coherent) with wavelength $\lambda_p = 532$ nm. A linear attenuator composed by a half-wave plate, a polarizing beam splitter and a second half-wave plate is implemented to control the power of the pump beam and its polarization.

A short-pass filter (SPF) is used to eliminate residual emission from the Verdi V10 at different wavelengths. This is due to the laser's operating principle. Namely, the Verdi is made up of two diodes that emit light at 808 nm and pump a neodymium-doped yttrium vana-

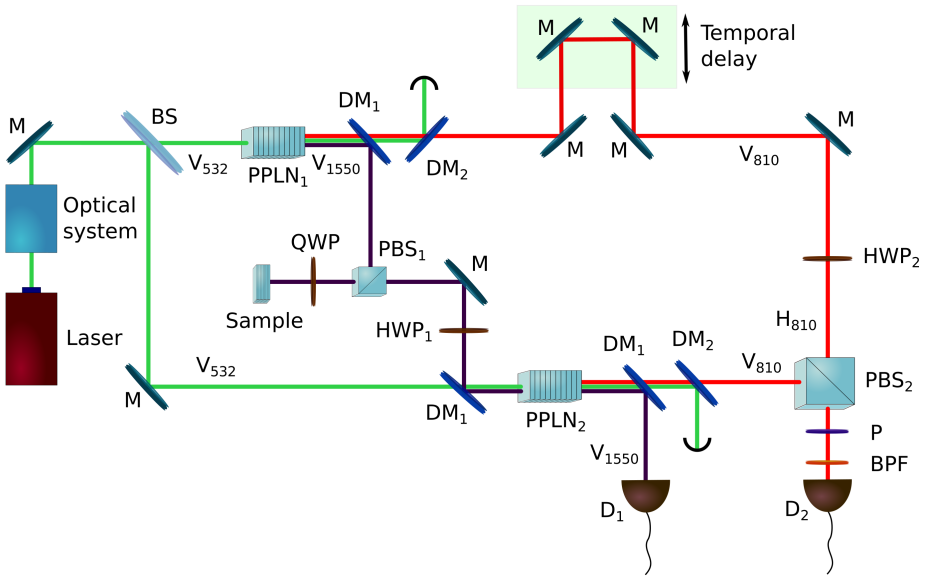

Figure 3.7: Experimental setup aimed at doing OCT based on the concept of induced coherence. *Laser*: Verdi V10 (Coherent). *Optical system*: linear attenuator and short-pass filter (SPF). *BS*: beam splitter. *M*: mirrors. $PPLN_{1,2}$: periodically-poled lithium niobate crystals. $DM_{1,2}$: dichroic mirrors. $PBS_{1,2}$: polarizing beam splitters. *QWP*: quarter-wave plate. $HWP_{1,2}$: half-wave plates. *Sample*: simulated by a mirror and a neutral density filter. *P*: linear polarizer. *BPF*: bandpass filter. D_1: optical spectrum analyzer (OSA) for telecom band. D_2: single-photon counting module. *V* designates vertical polarization with sub-indexes indicating the wavelengths of the corresponding beams.

date (Nd:YVO4) crystal, which then re-emits light at 1064 nm. This light is frequency-doubled by a lithium triborate (LBO) crystal in a ring cavity arrangement, yielding the desired 532 nm light. We discovered residual emission at 808 and 1064 nm in our measurements, which manifested as noise, and this is why we filtered out this unwanted emission.

3.4 Experimental setup

A 50:50 beam splitter (BS) divides the pump beam, allowing it to be directed with equal power to the two nonlinear crystals. The crystals are two 20 mm long periodically-poled lithium niobate[3] ($PPLN_{1,2}$). They absorb the 532 nm pump photon and generate two lower-frequency ones, the signal and the idler, by means of parametric down-conversion (PDC). The PDC process is non-degenerate Type-0, which means the pump, signal and idler photons all have the same vertical polarization and that the signal and the idler photons have different central wavelengths, 810 and 1550 nm, respectively.

The two nonlinear crystals are mounted on top of ovens (PV20 from Covesion) that are coupled to temperature controllers (OC2 from Covesion) that allow for temperature adjustments with a precision of 0.01 °C and a maximum working temperature of 200 °C. The spectral response of the nonlinear crystals changes with the temperature, resulting in various phase-matching conditions for each temperature. We set the temperatures in both ovens so that the emission from both crystals is spectrally identical.

The efficiency of the PDC processes in our experiment is very low. In particular, given that the crystals' effective second order nonlinear coefficient is $\chi^{(2)} = 14\ pm/V$ and that we used a pump power of $P =$ 1 W, the parametric gain[4] is of about $G \approx 10^{-11}$. This result implies that the number of entangled photons generated per mode at each crystal is significantly less than one, indicating that we are in the low parametric gain regime of PDC. In this scenario, the probability to generate simultaneously a pair of photons in both nonlinear crystals is negligible.

The signal s_1 and the idler i_1 generated in the first nonlinear crystal ($PPLN_1$) are separated by a dichroic mirror (DM_1). The signal s_1 is transmitted and forms the upper arm of the interferometer. The residual pump beam is eliminated with a dichroic mirror (DM_2). The signal s_1 experiences a temporal delay implemented by means of two mirrors located on top of a 6-mm translation stage (Thorlabs Z806).

[3] See Appendix B for the detailed material properties of the crystal.

[4] See Section 2.3.1 for a detailed analysis of the parametric gain concept.

This platform can move in steps of 30 nm to introduce the desired phase shift between both arms of the interferometer. After that, its polarization is rotated to horizontal by a half-wave plate (HWP_2) before reaching the PBS_2.

The idler i_1 is reflected and starts the lower arm of the interferometer. Because of its vertical polarization, it is reflected again by the polarizing beam splitter (PBS_1). A quarter-wave plate (QWP) changes its polarization to circular before interacting with the sample, simulated by a neutral density filter and a mirror mounted on a translation stage than can be moved longitudinally up to 1 mm. The idler is reflected by the sample with probability $|\tau|^2$. After this interaction, the idler i_1 polarization is changed to horizontal by the quarter-wave plate (QWP). The i_1 photon is then transmitted through PBS_1 and its polarization is again changed to vertical with a half-wave plate (HWP_1), in order to erase all distinguishing information with the idler generated in $PPLN_2$. It is finally reflected by the dichroic mirror (DM_1) and spatially overlapped with the pump that shines the second nonlinear crystal ($PPLN_2$).

As a result, the idler i_2 photon generated in $PPLN_2$ is consequently fully spatially and spectrally overlapped with the one coming from $PPLN_1$. The two idler photons are separated from the second signal photon s_2 by means of a dichroic mirror (DM_1) and coupled into a single mode fiber to an optical spectrum analyzer (OSA). The residual pump beam is eliminated with a dichroic mirror (DM_2). The signal photon s_2 travels through the lower arm of the interferometer until it reaches the PBS_2. An 810 ± 10 nm band-pass filter (BPF) is implemented at the output of PBS_2 to filter out any residual pump beam and to exclusively select the desired signal photons.

The results shown in the next section are interferometric measurements between the two signal photons (s_1 and s_2) after being recombined in the last polarizing beam splitter (PBS_2). In practice, the pump and the down-converted light have finite spectral width, which means finite coherence time. As a result, additional constraints related to the interferometers' arm lengths must be fulfilled. If the

pump has much longer coherence length than the down-converted light, which is the case, the following conditions must be satisfied:

$$|z_{p_2} - z_{p_1} - z_{i_1}| \ll L_{dc}, \tag{3.20}$$

$$|z_{s_1} - z_{s_2} - z_{i_1}| \ll L_{dc}, \tag{3.21}$$

where z_{p_2} is the optical path length travelled by the pump beam from the input BS to $PPLN_2$; z_{p_1} is the optical path length travelled by the pump beam from the input BS to $PPLN_1$; z_{i_1} is the optical path length travelled by the i_1 photon from $PPLN_1$ to $PPLN_2$; z_{s_1} is the optical path length travelled by the s_1 photon from $PPLN_1$ to the last PBS_2; z_{s_2} is the optical path length travelled by the s_2 photon from $PPLN_2$ to the last PBS_2; and L_{dc} is the coherence length of the down-converted light.

In other words, the two arms of the interferometer must be unbalanced up to the coherence length of the down-converted photons. If this requisite is satisfied, there is no way to tell which crystal a signal photon came from when it arrived at the detector. On the other hand, the interference is lost if the idler i_1 path is blocked or the conditions in Eqs. (3.20) and (3.21) are not met.

In the case that there is coherence between the signal photons, the polarization state at the output of PBS_2 is

$$|\Psi\rangle = \frac{1}{\sqrt{2}}\big[\,|H\rangle + \exp(i\phi)\,|V\rangle\,\big], \tag{3.22}$$

where ϕ is the phase shift between the two arms of the interferometer, assuming equal emission probability from both sources. Contrarily, if there is no coherence between the signal photons the polarization state reads

$$\rho = \frac{1}{2}\big[\,|H\rangle\langle H| + |V\rangle\langle V|\,\big], \tag{3.23}$$

which shows no phase difference dependence. In practice, a polarizer (P) is implemented at the output of PBS_2 to measure the phase

shift given in Eq. (3.22). The polarizer projects both orthogonally polarized signal photons to a diagonal state of the form

$$|D\rangle = \frac{1}{\sqrt{2}}\big[\,|H\rangle + |V\rangle\,\big]. \tag{3.24}$$

Finally, the interference signal is coupled into a single-mode fiber and measured with a silicon-based single-photon detector (SPCM-AQRH-13-FC from Perkin-Elmer).

3.5 Results

The main purpose of this work is to show, in a *proof-of-concept* experiment, the possibility to do a 1D axial scan of a sample using a nonlinear interferometer based on induced coherence . The results presented below are not meant to compete with the axial resolution values provided by standard OCT systems. In conventional OCT schemes LED light sources having a bandwidth greater than 100 nm (FWHM) are used, providing axial resolutions of few microns.

In our case, the idler spectral emission of the 20-mm-long PPLN Type-0 crystals has a bandwidth of around 1.6 nm at full-width at half maximum (FWHM). An optical spectrum analyzer for telecom band (HP 71451B from Hewlett Packard) was used to measure the spectrum, which was then digitized using WebPlotDigitizer. Figure 3.8 shows the measured spectrum of the idler photons, which corresponds to an axial resolution of about 500 μm. In the discussion section, it will be addressed how to increase the axial resolution.

The OCT measurement is mimicked by putting a mirror in the idler i_1 path, where the sample is meant to be placed (see Fig. 3.7), and changing its longitudinal position 1 mm. As mentioned in the previous subsection, the degree of first-order coherence between the signal photons is the quantity measured. The result is shown in Fig. 3.9.

The envelope delineated by the experimental data (blue dots) in Fig. 3.9 clearly corresponds to a triangular coherence function (solid

3.5 Results

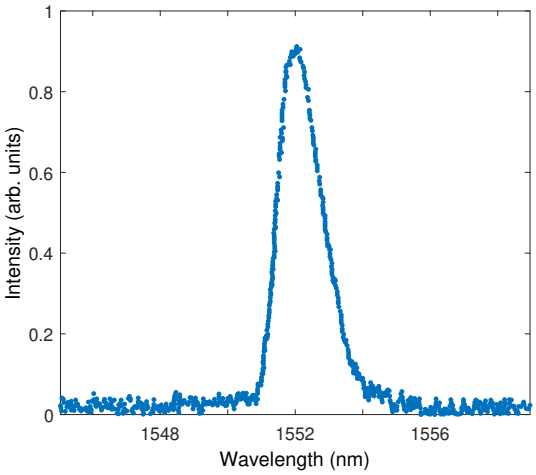

Figure 3.8: Measured spectrum of the idler photons. The spectrum is centered at 1552.3 nm with a bandwidth of 1.6 nm at full width at half maximum (FWHM).

blue line) for each of the two-layer positions, which can be written as[5]

$$\left|g^{(1)}_{s_1,s_2}(T)\right| = \frac{\left|\langle \hat{a}^{\dagger}_{s_1}(t+T)\hat{a}_{s_2}(t)\rangle\right|}{\sqrt{\langle \hat{a}^{\dagger}_{s_1}(t))\hat{a}_{s_1}(t)\rangle}\sqrt{\langle \hat{a}^{\dagger}_{s_2}(t)\hat{a}_{s_2}(t)\rangle}} = \\ = \mathrm{tri}\Big\{\frac{1}{DL}(T-T_0)\Big\}, \tag{3.25}$$

where *tri* is the triangular function, D is the inverse group velocity difference between signal and idler photons, L is the length of the nonlinear crystal and T_0 is the temporal delay between signal photons.

The product DL is the inverse bandwidth of the down-converted photons, which is proportional to the coherence length. The spatial

[5]See Appendix E for the complete derivation of the first-order coherence function.

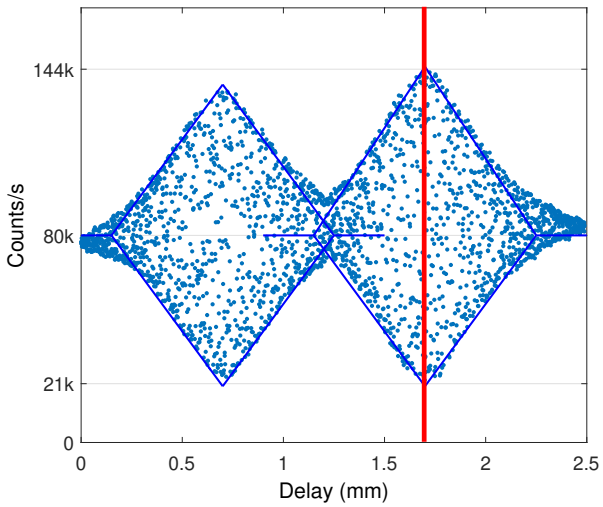

Figure 3.9: Degree of first-order coherence between the signal photons measured from two simulated *layers* separated 1 mm. We detect with a single-photon detector the 809.4 nm signal photons at the output of PBS_2, while changing the path length difference between the two arms of the interferometer by 1 μm steps. The maximum visibility is $V = 73\%$, marked with the red region. Blue dots are experimental data and the solid blue line stands for the theoretical prediction given by Eq. (3.25), considering our visibility values.

resolution cDL is the axial resolution of the OCT scheme (500 μm, in our case). This can be directly assessed by the value of the bandwidth at FWHM of the coherence functions shown in Fig. 3.9.

The maximum visibility of the peaks is slightly different, $V = 69\%$ for the left peak and $V = 73\%$ for the right one. This small discrepancy is due to the fact that the alignment was optimized for one position of the mirror. In these results, the full bandwidth of the down-converted photons generated in both crystals is used. Each experimental dot represents the number of signal photons detected by the single-photon module as the path length difference between

3.5 Results

the two arms of the interferometer is changed in 1 μm increments.

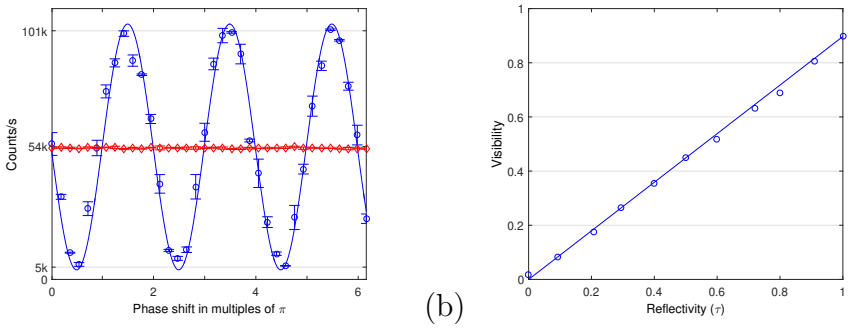

(a) (b)

Figure 3.10: (a) Interference fringes for two different values of the reflection coefficient. Blue circles: $|\tau| = 1$; Red diamonds: $|\tau| = 0$. The maximum visibility measured is $V = 90\%$. The error bars designate the standard deviation of the experimental measures. (b) Experimental and theoretical relationship between the interference pattern visibility and the reflectivity (τ). Circles: experimental data; Solid line: theoretical prediction given by Eq. (2.59), taking into account our visibility conditions.

Finally, we must get the experimental linear relationship between the visibility of the signal photons and the losses introduced in the idler i_1 path [Eq. (2.59)] in order to demonstrate that we are witnessing induced coherence in the low parametric gain regime. Figure 3.10(a) shows the number of signal photons detected at the output of PBS_2 while changing the path length of one arm of the interferometer with respect to the other by 30 nm steps. Interference fringes appear for $|\tau| = 1$ (blue circles) with a visibility of $V = 90\%$. On the other hand, when the idler i_1 path is blocked ($|\tau| = 0$) the interference disappears (red diamonds). The phase scan depicted in Fig. 3.10(a) was performed in the red region shown in Fig. 3.9.

Figure 3.10(b) depicts the experimental relationship between the visibility of the interference pattern and the reflectivity τ. The value

of τ is introduced by a variable neutral density filter (NDF) placed in the idler i_1 path. The maximum visibility observed is $V = 90\%$, which is crucial for achieving high sensitivities when sensing layer reflectivities.

In contrast to the results presented in Fig. 3.9, where the whole bandwidth of the signal photons was used, in the measurements shown in Fig. 3.10 the spectral bandwidth is filtered using a 8-mm fiber Bragg grating (FBG). It provides a very narrow filtering of about 0.1 nm. At room temperature, the FBG filter's central operating wavelength is 809.4 nm. The central wavelength can be altered by changing its temperature or stretching it, but we chose to change the temperature of the PPLN ovens instead. This is the reason why the idler spectrum shown in Fig. 3.8 is centered at 1552.3 nm.

The FBG is used to narrowly filter the signal photons bandwidth for two main reasons. To begin with, it increases the coherence length up to tens of centimeters, making it simpler to experimentally balance both arms of the interferometer. Notwithstanding, the axial resolution degrades considerably. This the reason why we do not use the FBG for the optical sectioning measurement shown in Fig. 3.9.

On the other hand, the use of the FBG provides for a reduction in the spectrum distinguishability of photons generated in distinct crystals. This explains the noticeable increase in visibility compared to when we use the full bandwidth. In fact, the maximum visibility value obtained in our work ($V = 90\%$) is remarkably high when compared to the values of similar works.

For instance, in the original paper on induced coherence paper from 1991 [9] the maximum visibility value obtained was $V = 30\%$. In a more recent work by Barreto *et al.* [10], they showed a maximum visibility value of $V = 77\%$. These results from prior works demonstrate how difficult it is to correctly overlap spatial modes when huge bandwidths are considered, as well as to adjust for all the many degrees of freedom in the system than can cause path distinguishability.

3.6 Frequency-correlation requirements for observing induced coherence

Note: the results, figures and conclusions of this section are taken from Ref. [62]. The idea of induced coherence was first demonstrated in the low parametric gain regime of down-conversion [9,22], although later it was also shown that this effect is still present in the high gain regime as well [28, 29]. In the first scenario, paired photons are generated in one crystal or the other, while in the latter can be generated in both simultaneously.

The low parametric gain regime is of particular interest to us because it allows to easily assess the degree of entanglement between down-converted photons. In this context, a continuous-wave (CW) laser is used to shine coherently the two separated parametric down-converters, so that the bandwidth of the pump laser δ_p is much smaller than the bandwidth of down-conversion Δ_{dc} [40]. Thus, the signal-idler pair is generated with a high degree of entanglement. Thus, we can ask ourselves: *What is the role of entanglement and correlations in induced coherence? Can induced coherence still be observed if there is no frequency-correlations between the signal-idler pair?*

For the sake of simplicity, we restrict our analysis to the frequency-entanglement case. That is, we consider the biphoton function that describes the signal-idler pair to be of the form $\Phi(\Omega_s, \Omega_i)$, where $\Omega_{s,i}$ are the signal and idler photons frequency deviations, respectively. If the biphoton function can be factored, i.e. $\Phi(\omega_s, \omega_i) = F(\Omega_s)G(\Omega_i)$, then the state is separable and there is no frequency entanglement. On the contrary, if the biphoton function is not separable, then the state is entangled.

The key parameter to quantify the degree of entanglement is the ratio between the bandwidth of the pump and the bandwidth of down-conversion $\gamma = \delta_p/\Delta_{dc}$ [63, 64]. The state is separable if $\gamma = 1$,

and the degree of entanglement is high if $\gamma \gg 1$ or $\gamma \ll 1$.

Let us start our analysis assuming that the shape of the spectrum of pump beam is described by the function

$$F_p(\Omega_p) = \frac{T_0^{1/2}}{\pi^{1/4}} \exp\left[-\frac{\Omega_p^2 T_0^2}{2}\right] \exp\left[ik_p(\Omega_p) z_p\right], \tag{3.26}$$

which constitutes a Gaussian spectral shape. $\Omega_p = \Omega_s + \Omega_i$ is the pump frequency deviation, T_0 is the temporal width of the pump pulse duration, k_p is the pump wave-vector and z_p is the distance travelled by the pump beam until it reaches the nonlinear crystal. The function $F_p(\Omega_p)$ is normalized to 1.

Starting from this and taking into account the appropriate Bogoliubov transformations at both nonlinear crystals, the first-order correlation function $g^{(1)}_{s_1,s_2}$ between the signal photons in an induced coherence scheme is[6]

$$\left|g^{(1)}_{s_1,s_2}(T_1,T_2)\right| = \mathrm{tri}\left(\frac{T_1}{DL}\right) \exp\left[-\frac{1}{16T_0^2}\left[\left(1-\frac{2D_+}{D}\right)T_1 + 2T_2\right]^2\right], \tag{3.27}$$

where $\mathrm{tri}(\xi/2) = 1/\pi \int \mathrm{sinc}^2(x)\exp(i\xi x)\mathrm{d}x$ is the triangular function, $D_+ = N_p - (N_s + N_i)/2$ ($N_{p,s,i}$ are the inverse group velocities), and

$$T_1 = \frac{z_3 - z_1 + z_2}{c} + N_i L, \tag{3.28}$$

$$T_2 = \frac{z_{p_2} - z_{p_1} - z_2}{c} - N_i L. \tag{3.29}$$

$z_{1,2,3}$ are the distances travelled by the signal s_1, the idler i_1 and the signal s_2, respectively. The condition $T_2 = 0$ needs to be fulfilled to ensure proper parametric amplification in the second nonlinear crystal.

On the other hand, in an induced coherence scheme working in the low parametric gain regime, the biphoton function $\Psi(\omega_s, \omega_i)$ can

[6]See Appendix E for the complete derivation of $g^{(1)}_{s_1,s_2}$.

be written as [61]

$$\Psi(\Omega_s, \Omega_i) = i\sigma L F(\Omega_s + \Omega_i) \text{sinc}\left[\frac{\Delta k L}{2}\right] \exp\left(i s_k L\right), \tag{3.30}$$

where σ is the nonlinear coefficient (see Section 2.3.1, Eq. (2.19)), L is the length of the nonlinear crystal, $F(\Omega_s + \Omega_i)$ is a function that describes the pump spectrum shape, $\Delta k = k_p(\Omega_s + \Omega_i) - k_s(\Omega_s) - k_i(\Omega_i)$ is the wave-vector phase mismatch, and $s_k = k_p(\Omega_s + \Omega_i) + k_s(\Omega_s) + k_i(\Omega_i)$ determines the nature of the correlations between the paired photons and the degree of entanglement between them [36].

Under certain approximations [61, 65], the normalized biphoton function [Eq. (3.30)] is

$$\Phi(\Omega_s, \Omega_i) = \left(\frac{\alpha T_0 D L}{\sqrt{2}\pi}\right)^{1/2} \exp\left[-\frac{(\Omega_s + \Omega_i)^2 T_0^2}{2}\right] \times \exp\left[-\frac{\alpha^2 (DL)^2}{16}(\Omega_s - \Omega_i)^2\right], \tag{3.31}$$

where $\alpha = 0.455$; T_0 is the pump pulse duration and $D = N_i - N_s$ is the difference of idler and signal inverse group velocities. $|\Phi(\Omega_s, \Omega_i)|^2$ is the probability to detect a signal photon at frequency $\omega_s^0 + \Omega_s$ in coincidence with an idler photon at frequency $\omega_i^0 + \Omega_i$.

Figure 3.11 shows the normalized biphoton functions [Eq. (3.31)] and the first-order correlation functions [Eq. (3.27)], for three different pump pulse widths. The three cases correspond to different degrees of entanglement γ: $\gamma \ll 1$ ($T_0 = 100$ ps), $\gamma = 1$ ($T_0 = 212$ fs) and $\gamma \gg 1$ ($T_0 = 10$ fs).

There is frequency anti-correlation between signal and idler photons when $T_0 \gg DL$ (Fig. 3.11(a)). In this scenario, coincidences can be detected if $\Omega_i \sim -\Omega_s$. There is frequency correlation for $T_0 \ll DL$ (Fig. 3.11(c)), and there are coincidences if $\Omega_i \sim \Omega_s$. The degree of correlation is low in between, and the quantum state is separable (Fig. 3.11(b)). The first-order correlation functions for these examples are shown in Fig. 3.11(d), (e) and (f). We see coherence for all degrees

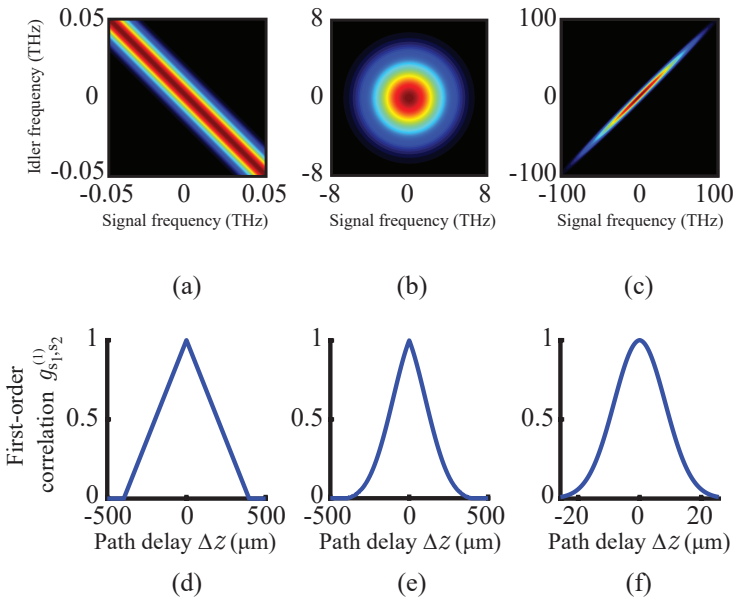

Figure 3.11: (a), (b) and (c): Normalized biphoton function $|\Phi(\Omega_s, \Omega_i)|^2$, for different pump pulse duration T_0. The axis correspond to the signal and idler angular frequency deviation, Ω_s and Ω_i, respectively. (d), (e) and (f): First-order correlation function $g^{(1)}_{s_1,s_2}$. The pump pulse duration T_0 are: (a) and (d) $T_0 = 100$ ps; (b) and (e) $T_0 = 212$ fs; (c) and (f) $T_0 = 10$ fs. The nonlinear crystal length is $L = 5$ mm.

of entanglement, throwing out the possibility that induced coherence is caused by the entanglement nature of the paired photons.

In conclusion, the initial question is answered: induced coherence in the low parametric gain regime can be observed regardless of the degree of entanglement between the signal and idler photons. As a result, we infer that the induced coherence is not the product of paired photon quantum entanglement.

3.7 Discussion

As previously stated, the results reported in Section 3.5 constitute a proof of work that lay the groundwork for developing OCT techniques based on nonlinear interferometers. For realizing this promise, this novel approach should solve certain problems that at this moment in time prevent the new OCT scheme from being considered a *practical* OCT solution.

The most remarkable practical advantage of OCT based on a nonlinear interferometer vs *typical* or standard OCT systems is that it allows the light that probes the sample under investigation to have a different wavelength than the light that is detected. This has two important consequences:

- *To detect light at the most convenient wavelength:* Certain wavelengths are more handy because detectors in that frequency band are more efficient. Silicon-based photodetectors, for example, which are the most common and cost-effective, perform admirably in the $700 - 900$ nm wavelength range, with great efficiency and response times. However, due to the material's inherent limitations, silicon produces a significant reduction in sensitivity above 1000 nm. Alternatives to silicon-based photodetectors, such as indium gallium arsenide (InGaAs) detectors, are significantly more expensive and harder to operate.

- *To use longer wavelengths for probing the sample:* Parametric down-conversion is a versatile solution to generate light in the far-IR range or even THz radiation [14, 66]. In a biological imaging scenario, this would result in a deeper penetration depth into the sample, while still using the optimum wavelength for detection.

The following are the most noticeable limitations of OCT based on induced coherence over its standard counterpart:

- *The axial resolution:* As a general rule in OCT systems, the broader the spectrum bandwidth, the better is the axial resolution. Typical axial resolution values of standard OCT systems are between 3 and 12 μm [4]. Broader bandwidths (hundreds of nanometers) in parametric down-conversion can be obtained by using shorter nonlinear crystals or by appropriately engineering the phase-matching conditions of longer crystals [64,67,68]. In this way, axial resolutions similar to the ones achieved with current OCT systems are likely to be observed.

- *The acquisition times:* The OCT approach proposed here is based on a time domain measurement, which involves scanning the location of one mirror in one interferometer arm while measuring the interference signal. As mentioned in the introduction of this Chapter, Fourier or spectral-domain OCT provides for a noticeable increase of the imaging speed because there are no movable elements. It also outperforms TD-OCT in terms of sensitivity [59]. In short, re-adapting our proposal's detection system to perform frequency measurements would be a significant upgrade.

- *The power:* For OCT applications in ophthalmology, for example, light entering the cornea should have a maximum power of about 750 μW. Typical power values in art restoration studies are a few mW. All of these power values are dramatically higher than the power involved in our proposal. The solution to this challenge is to work in the high parametric gain regime of down-conversion [43], rather than the low gain regime. In this sense, applications for imaging have been already demonstrated in both regimes [69]. Another possibility is to use stimulated parametric down-conversion processes [70].

- *The robustness:* The OCT system proposed has to improve in terms of robustness. As previously stated, any type of path distinguishability has a significant impact on the induced coher-

ence effect, and precisely overlapping the idler modes is quite difficult. As a result, this novel approach is unlikely to be a viable OCT solution. A Michelson-type nonlinear interferometer[7] could be a more robust choice since only one nonlinear crystal is employed. It is easier to align experimentally and requires fewer optical elements.

It is worth noting that several of these limitations have been already addressed in different works. In 2018, two months after our publication, Paterova *et al.* [16] demonstrated a TD-OCT system using an SU(1,1) nonlinear interferometer in the low parametric gain regime of down-conversion. This approach solves the robustness weakness of our proposal since only one nonlinear crystal is used, but still the power limitation is present.

In 2020, Vanselow *et al.* [71] put forward a FD-OCT system using an SU(1,1) nonlinear interferometer in the low parametric gain regime of down-conversion. They use ultra-broadband paired photons, which allows them to reach an impressive OCT axial resolution of 10 μm. Furthermore, the measurements are made in the Fourier domain, which speeds up acquisition and improves sensitivity. Even so, the power used to illuminate the sample (90 pW) is still insufficient for ophthalmology applications.

It is conceivable to devise an OCT setup based on nonlinear interferometry that overcomes all of these drawbacks. It is an SU(1,1) nonlinear interferometer that makes Fourier domain measurements and operates in the high parametric gain regime with broad bandwidth paired photons. That is precisely the proposal presented in the following Chapter.

[7] See Section 2.2 for a detailed description of a Michelson-type nonlinear interferometer.

CHAPTER

FOUR

OPTICAL COHERENCE TOMOGRAPHY IN THE HIGH PARAMETRIC GAIN REGIME

This chapter describes the second nonlinear interferometer aimed at doing OCT implemented in this thesis. It is an SU(1,1) nonlinear interferometer working in the high parametric gain regime of down-conversion [51]. This novel scheme can be understood as the *enhanced version* of the experimental setup presented in Chapter 3. The first part of this chapter is devoted to describe how this new scheme overcomes the main limitations presented in the discussion section of the previous chapter. Then the attention is shifted to analyze mathematically this new scheme. Finally the experimental setup and main results are presented and discussed in detail.

4.1 Introduction

For sensing and imaging, the high parametric gain regime of PDC has various advantages. Firstly, higher photon fluxes allow for the use of standard charge-coupled device (CCD) cameras or spectrometers rather than single-photon detectors, resulting in images with a higher signal-to-noise ratio and faster acquisition times. Secondly, in contrast to traditional OCT or in the case of low parametric gain applications, the measured power is significantly higher than the power probing the sample. Thirdly, because the interference visibility is nonlinearly related to the idler losses, this regime is particularly susceptible to small reflectivities. Finally, the high-gain regime affords bigger frequency bandwidths [47], which would result in an improved axial resolution in OCT methods.

There are a few weaknesses in the OCT scheme presented in the previous chapter that can be now fixed. These limitations have practical solutions. Working in the high parametric gain regime of PDC is the solution to achieve higher power values to probe the sample and to detect it. The parametric gain indicates the flux rate of photon pairs generated per mode, and the most efficient way to achieve higher-than-one values of the gain is to use strong pulsed pump lasers (among others, see Section 2.3.1).

In one of the experiments with the highest flux rate of down-converted photons reported up to date using CW pumping [46], they generated flux rates of $\sim 10^{12}$ paired photons per second, which is equivalent to a power of ~ 0.3 μW at 1064 nm. This high values of the flux rate required the use of a long crystal ($L = 12$ mm) and type-I SPDC, which restricted the bandwidth of down-conversion to $\Delta\lambda = 31$ nm. More dramatically, pump powers of up to 2 W were needed. Still the value of the gain is very small, $G \sim 10^{-11}$. We should remark that these high values of flux rates would be very difficult to achieve with CW pumping with shorter crystals and non-degenerate SPDC configurations.

Instead, when using a pulsed pump laser high gain levels can be

achieved. In Ref. [72], they use a pulsed laser with pulses of duration 18 ps, beam waist 170 μm, and average pump power up to 25 mW. They generated flux rates of $\sim 5 \times 10^7$ paired photons per second and per mode, with a gain of $G = 15$. Taking into account that the frequency repetition rate of the pump laser is 1 KHz, and at least 40 modes are being generated, this result in a flux rate of $\sim 2 \times 10^{12}$ paired photons per second. The bandwidth is $\Delta\lambda = 90$ nm at 790 nm. The main advantage of this approach is that it is much more versatile concerning which photon wavelengths, bandwidth and flux rates can be generated.

It is worth noting that in 2009, Shapiro *et al.* [73] demonstrated an OCT scheme based on induced coherence and large parametric gain, using a pair of bright pseudo-thermal beams possessing phase-sensitive cross correlation. This proposal solves the power limitation of our proposal, although it still has a low axial resolution (~ 2 mm) and perform the measurements with IR light beams.

Returning to our proposal's limitations, adopting Fourier or spectral domain OCT (FD-OCT) instead of time-domain OCT (TD-OCT) can result in a reduction in acquisition times. Experimentally, it is as simple as measuring the signal spectrum with a standard visible spectrometer without having to scan the phase of one of the interferometer arms.

Furthermore, as shown in Ref. [16], utilizing a single crystal configuration improves robustness and simplicity. The scheme is an SU(1,1) nonlinear interferometer rather than an induced coherence interferometer. Because fewer optical elements are required, the risk of loss and misalignment is reduced, which is advantageous for OCT.

Finally, the axial resolution of our OCT scheme (~ 500 μm) is very far from the values handled in standard OCT ($\sim 3 - 12$ μm). The axial resolution of OCT is generally determined by the bandwidth of the light employed, with the broader the bandwidth, the higher the axial resolution. There are several approaches to enhance the bandwidth of down-converted photons. We choose the easiest solution: shorten the nonlinear crystal's length. As a result, we will

employ an identical nonlinear crystal as in the previous chapter, but 20 times shorter.

The scheme presented in this chapter is the product of all of these considerations and experimental changes. It is an SU(1,1) nonlinear interferometer that works in the high parametric gain regime of down-conversion. The goal is to conduct a *proof-of-concept* experiment to show that this approach can be used to perform FD-OCT of a sample.

4.2 Experimental setup

The experimental setup used is shown in Fig. 4.1. The pump laser is the second-harmonic of a pulsed Nd:YAG laser (model PL2210A-SH-TH, from EKSPLA) that generates 18 ps pulses at wavelength $\lambda_p = 532$ nm and repetition rate of 1 kHz. A linear attenuator (not depicted in Fig. 4.1) composed by a half-wave plate, a polarizing beam splitter and a second half-wave plate is implemented to control the mean power and the polarization of the pump beam.

A dichroic mirror (DM_1) reflects the pump beam towards an $L = 1$ mm periodically poled lithium niobate ($PPLN$) crystal that generates by means of parametric down-conversion signal and idler beams at central wavelengths $\lambda_s = 810$ nm and $\lambda_i = 1550$ nm, respectively. The PDC process is Type-0, meaning that the pump, signal and idler beams have the same vertical polarization.

The nonlinear crystal is mounted on top of an oven (PV10 from Covesion) that is coupled to a temperature controller (OC1 from Covesion) that allows for temperature adjustments with a 0.01 °C precision and a maximum working temperature of 200 °C. In this way, the spectral response of the nonlinear crystal can be tuned by changing its temperature. The temperature of the PPLN crystal is set at $T = 123$ °C, obtaining a signal spectrum bandwidth of 8 ± 1 nm at full-width half maximum (FWHM), measured with a visible spectrometer (AvaSpec StarLine, from Avantes). The idler spectrum bandwidth is 30 ± 3 nm, measured with an infrared spectrometer

4.2 Experimental setup

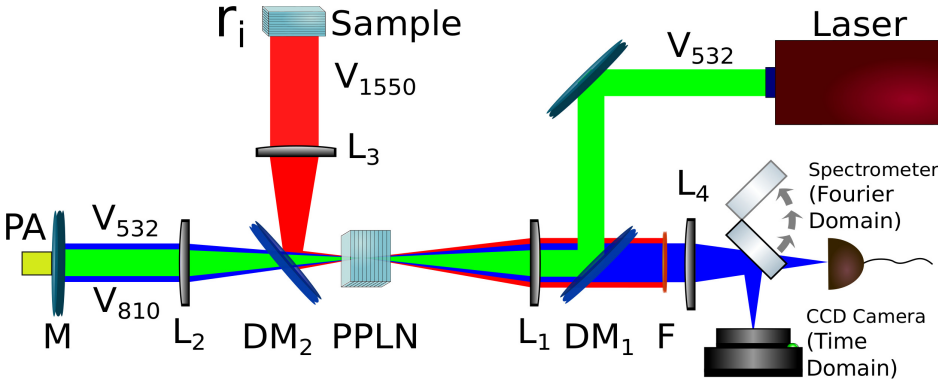

Figure 4.1: Experimental setup aimed at doing OCT based on an SU(1,1) nonlinear interferometer in the high-parametric gran regime of down-conversion. *Laser*: PL2210A/SH/TH (Ekspla). $DM_{1,2}$: dichroic mirrors. $L_{1,2,3,4}$: lenses. $PPLN$: periodically-poled lithium niobate crystal. M: mirror. PA: piezoelectric actuator. F: short-pass filter. V designates vertical polarization with sub-indexes indicating the wavelengths of the corresponding beams. With a flip mirror, one can measure the flux rate of signal photons (Time-domain measurement) or its spectrum (Fourier-domain measurement).

(AvaSpec NIRLine, from Avantes).

The pump beam is focused onto the nonlinear crystal by means of lens L_1 with focal length $f_1 = 200$ mm. The pump beam size at the crystal is 40 ± 10 μm (FWHM). The signal s_1 and the idler i_1 beams are separated by a short-pass dichroic mirror (DM_2) with transmission edge at 950 nm (DMSP950T, from Thorlabs). The signal s_1 and the pump are transmitted while the idler beam is reflected, forming the two arms of the interferometer.

The *reference arm* of the interferometer is formed by the signal s_1 and pump beams. Both are collimated using a lens L_2 with focal length $f_2 = 200$ mm. On the other hand, the idler i_1 beam constitutes the *probing arm* of the interferometer and is collimated using the lens L_3 with focal length $f_3 = 150$ mm.

The pump and signal beams are reflected by a mirror (M) that is mounted into a piezoelectric actuator (PA) to scan the phase if needed. After that, both beams are focused back onto the nonlinear crystal by means of lens L_2. The distance travelled by the signal s_1 before re-entering the nonlinear crystal is $2z_s$. At the same time, the idler i_1 beam interacts with an object with reflectivity r_i and is focused back on the crystal by the lens L_3, travelling a total distance $2z_i$.

Finally, parametric amplification takes places due to the second pass of the pump by the nonlinear crystal. The signal s_2 and idler i_2 beams are generated. Both are transmitted by the dichroic mirror (DM_1) and the idler radiation is filtered out by a short-pass filter (F). A flip mirror allows to change between two different detection devices: a CCD camera and a spectrometer. The results presented in the next section were taken using both detection systems.

In the first case, the signal s_2 is reflected by the mirror to a CCD camera (SP620U, from Spiricon) placed in the Fourier plane of a lens L_4 (focal length $f_4 = 100$ mm). In this scenario, when the phase of the pump beam is scanned by the piezoelectric actuator (PA), interference fringes arise if the arms of the interferometer are balanced up to the coherence length of the PDC radiation.

On the other hand, if the flip mirror is removed from the signal s_2 path, the signal beam is spatially filtered in the Fourier plane of lens L_4 and fiber-coupled to a visible spectrometer (AvaSpec StarLine, from Avantes). In this scenario, the signal s_2 spectrum is directly measured. The spectral interference is observed without scanning the phase, regardless of the optical path difference [74], as long as the fringes are broader than the spectrometer resolution.

4.3 Mathematical analysis of OCT in the high parametric gain regime

The results presented in the next section are based on measurements of the signal beam spectrum $S(k)$ (Fourier-domain measurement) or signal photons flux N_s (time-domain measurement). The complete derivation of both quantities for an SU(1,1) nonlinear interferometer is done in detail in Section 2.3.1. In particular, the OCT measurement that we present next is in the Fourier domain. This means that when a sample is introduced into the idler i_1 path, the spectrum of the signal s_2 beam is measured without scanning any mirror. The probed sample is a single layer with two facets. In this case, its field reflectivity can be written as [61]

$$r(k) = r_1 + r_2 \exp\left[2i(k_0 n_0 + k n_g)d\right], \tag{4.1}$$

where $r_{1,2}$ are the field reflection coefficients from the first and the second facets, respectively. Note that the power reflection coefficients are $R_{1,2} = |r_{1,2}|^2$. n_0 is the refractive index at the central frequency, n_g is the group index, d is the sample thickness, $k = \Omega/c$ is the wavenumber deviation from the central wavenumber $k_0 = \omega_0/c$, and Ω is the angular frequency deviation from the central frequency ω_0.

The spectral density of the signal photons s_2, which is the quantity that is measured by a spectrometer, is

$$\begin{aligned} S(k) &= |V_s(k)|^2 \left[1 - |r(-k)|^2\right] + \\ &+ \left| U_s(k) V_s(k) e^{i\varphi_s(k)} + r^*(-k) U_i^*(-k) V_s(k) e^{-i\varphi_i(-k)} \right|^2, \end{aligned} \tag{4.2}$$

where $\varphi_s(k) = 2(k_s^0 + k)z_s$ and $\varphi_i(k) = 2(k_i^0 + k)z_i$. $2z_s$ and $2z_i$ are the distances traversed by the signal and idler photons before entering the nonlinear crystal. The expressions for the Bogoliubov complex functions $U_{s,i}(k)$ and $V_{s,i}(k)$ are presented in Section 2.3.1 [Eqs. (2.23) and (2.24)].

As detailed in Section 3.2.2, a Fourier transform procedure is applied to the measured spectrum $S(k)$ to experimentally determine the position of the sample's facets and their reflection coefficients. Although the shape of the spectrum $S(k)$ in the low and high parametric gain regimes are qualitatively similar, it is only possible to obtain an analytical solution for the Fourier transform in the low parametric gain regime [61].

On the other hand, we carry out a time-domain measurement to investigate the dependence of the signal s_2 beam's interference visibility on the sample's reflectivity located in the idler i_1 path. That is, the flux of signal s_2 photons is measured while the phase is scanned, for different reflectivity values of the sample. The general expression for the interference visibility is described in Section 2.3.1.

4.4 Experimental results

The key to the results presented in this chapter is that the measurements have been made in the high parametric gain regime of down-conversion. The concept of parametric gain has been defined and explained in length on these pages, including what it means, what it depends on, and what are its implications. However, no instructions on how to quantify it experimentally have been provided. Now is the time to do so.

The parametric gain G can be found from the nonlinear dependence of the measured PDC intensity I on the pump average power P (see Fig. 4.2) [43]. The fitting function [75]

$$I = I_0 \sinh^2\left(B\sqrt{P}\right), \tag{4.3}$$

is based on Eqs. (2.27) and (2.29), with I_0 and B being the fitting parameters. The gain must be measured around the zero mismatch; otherwise, one gets an averaged value of G. This is why the PDC radiation must be well filtered in $\mathbf{q}$ and Ω, near the frequency-degenerate point. To do so experimentally, the signal photons are filtered very

narrowly with a band-pass filter (810 ± 2 nm) and its intensity is measured in the Fourier plane of a lens $f = 50$ mm.

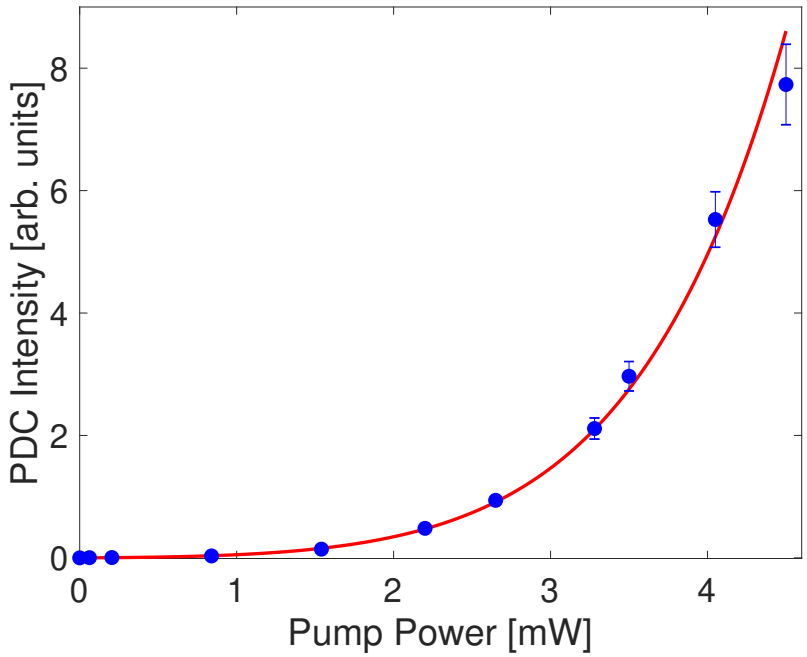

Figure 4.2: Measured dependence of the PDC intensity on the pump power (blue dots) and its fit function (red line), according to Eq. (4.3). The error bars designate the standard deviation of the experimental measures.

After the fitting and proper filtering, each pump power corresponds to a certain gain value

$$G = B\sqrt{P}. \tag{4.4}$$

In our experiment, we measure the parametric gain for the first pass by the nonlinear crystal to be $G = 1.7 \pm 0.2$. Thus, the total number of idler photons probing the sample is estimated to be about ~ 13000

photons, which is equivalent to ~ 7 paired photons per mode, clearly corresponding to the high parametric gain regime of PDC. The total energy of the idler photons probing the sample is 1.6 pJ, which leads to a mean power value of 1.6 pW[1].

Apart from the value of the parametric gain, the nonlinear dependence of the interference visibility on the reflectivity of the sample is another crucial evidence that we are in the high parametric gain regime of PDC. To study this relation, the reflectivity of a sample is mimicked by a variable neutral density filter (NDC-50C-4M, from Thorlabs) and a highly reflecting mirror.

We measure the flux rate of signal s_2 photons $N_s = 1/(2\pi) \int S(k)dk$ as a function of the path length difference between the two arms of the interferometer, scanned by a piezoelectric actuator PA (see Fig. 4.1). The visibility of the interference fringes is assessed according to the definition $V = (N_s^{max} - N_s^{min})/(N_s^{max} + N_s^{min})$, where N_s^{max} and N_s^{min} are the maximum and minimum of the flux rate, respectively. The procedure is repeated for several values of the reflectivity of the sample r_i, i.e. for several positions of the neutral density filter placed in the idler i_1 path.

Note that the two arms are balanced up to the coherence length of the PDC radiation ($l_c \sim \lambda^2/\Delta\lambda = 82$ μm), where $\Delta\lambda$ is the bandwidth of PDC at FWHM. The phase scan is performed in a small region (0.5 μm) around the maximum visibility point. Figure 4.3 shows the measured interference visibility (blue dots) for $G = 1.7$ and calculated for $G = 0.4$ (red dashed line), $G = 1.7$ (green solid line) and $G = 4.8$ (blue dashed line), according to Eq. (2.39). The insets of Fig. 4.3 show some examples of the measured interference patterns when scanning the phase. The maximum visibility value measured is $V = 90\%$.

We consider a reflectivity $r_s = 0.6$ for the signal beam that takes into account losses in optical elements along the signal s_1 path (double pass through an uncoated lens and the dichroic mirror) and possible spatial mode mismatch. Note that in the very high parametric gain

[1]See Appendix F for a detailed explanation on how to estimate all these values.

4.4 Experimental results

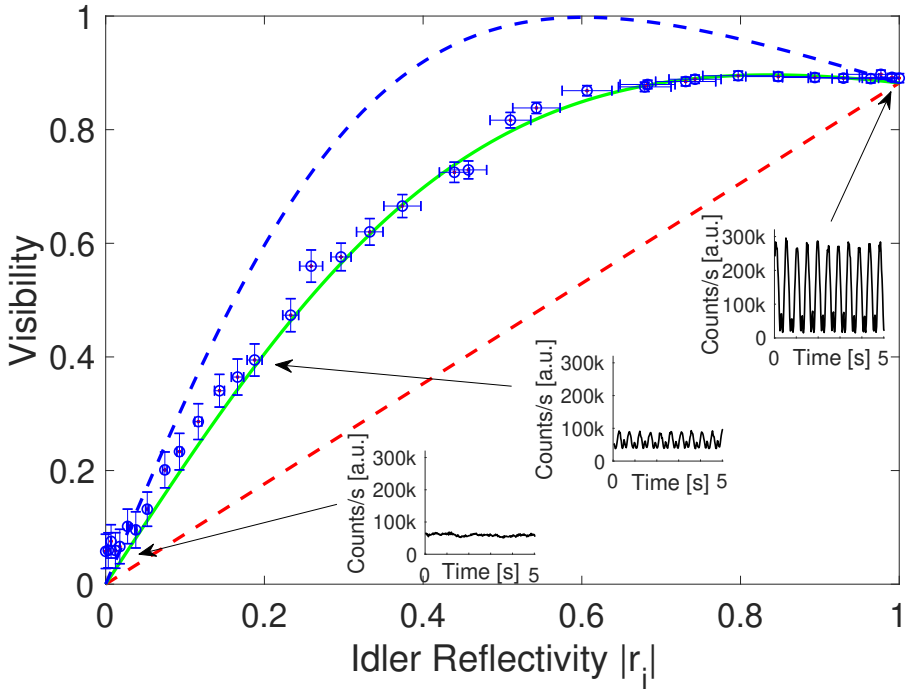

Figure 4.3: Interference visibility as a function of the idler reflectivity. Blue dots are experimental data, error bars are given by the standard deviation, and lines are theoretical predictions. We consider $r_s = 0.6$. Dashed red curve: $G = 0.4$ (low gain regime); green solid line: $G = 1.7$; dashed blue line: $G = 4.8$. For the theoretical curves, we choose the path length difference Δz that provides the best visibility. The error bars designate the standard deviation obtained by error propagation (see Appendix I for further details).

(blue dashed line) case, if the signal and idler losses are equal, $r_s = r_i$, the visibility value is 1.

The green solid line is the case studied in our experiment, which clearly shows the expected nonlinear dependence. The experimental results are in good agreement with the theory. These nonlinear relationships have also been observed for configurations where

the first parametric down-converter is seeded with an intense signal beam [11, 76].

This nonlinear dependence is an indication of the sensitivity enhancement of OCT: for lower reflectivity values, which is the case of interest for multiple OCT applications, the slope increases with the gain. Concretely, the slope goes from 1 for the low gain regime [Eq. (2.43)] to 2 for the high gain regime [Eq. (2.44)]. This last value is also characteristic of standard OCT systems.

The final results in this work demonstrate Fourier or spectral-domain OCT (FD-OCT) using this high-gain SU(1,1) nonlinear interferometer. In contrast to time-domain OCT (TD-OCT), which requires a value of path unbalancing Δz near to zero (within the coherence length of the source), FD-OCT analyzes the modulation of the spectrum of the output signal beam and requires a non-zero value of the path length difference. This is the reason why we start by determining the path length difference between the two arms of the interferometer.

Figure 4.4 summarizes the main results on the path unbalancing Δz characterization. We move the position of a mirror in the signal path to modify the path difference between the two arms of the interferometer. Figure 4.4(a) and (b) show the measured spectrum for two different values of the path length difference: $\Delta z_1 = 300$ μm and $\Delta z_2 = 220$ μm. The spectral modulation visibility is affected by signal path losses as well as the resolution of the spectrometer ($\delta\lambda \sim$ 1.2 nm). Despite this, we can still obtain relevant information.

Figure 4.4(c) depicts the Fourier transform of the spectra shown in Figs. 4.4(a) and (b). The separation between the two peaks is 80 μm, which is exactly the difference between the two unbalancing values ($\Delta z_1 - \Delta z_2$) considered. Finally, the procedure is repeated for several unbalancing positions. Figure 4.4(d) shows the position of the Fourier transform peaks as a function of the path length difference. The experimental data is in good agreement with the theoretical prediction.

There are some limitations to consider when resolving the spectral

4.4 Experimental results

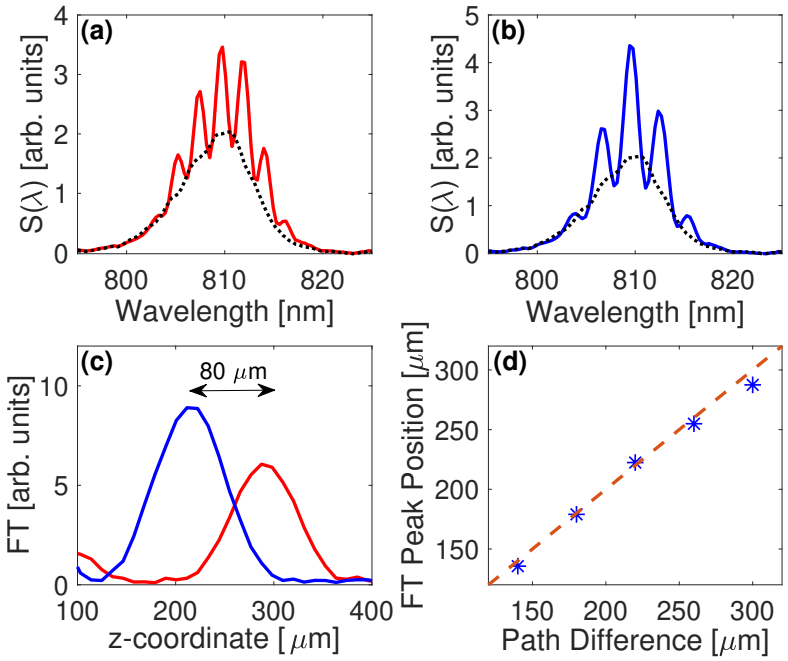

Figure 4.4: (a,b) Spectra measured for two different optical path differences $\Delta z_{1,2}$ (solid line). The dotted lines stand for the spectrum when the idler arm is blocked. (a) $\Delta z_1 = 300$ μm; (b) $\Delta z_2 = 220$ μm. (c) Zoom of the Fourier transforms of the (a,b) spectra after resampling to wavenumber k. The position of the peaks assesses directly the unbalancing between the arms of the interferometer. The peak separation is 80 μm, corresponding to the path difference between $\Delta z_1 - \Delta z_2$. (d) Position of the Fourier transform peak versus the path difference. Stars are the experimental data, and the dashed line is the theoretical dependence assuming exact equality.

modulations, basically related to the bandwidth of the source Δ_{dc} and the resolution of the spectrometer $\delta\lambda$. That is, the average fringe separation in angular frequency ($2\pi c/|\Delta z|$), must be smaller than the PDC bandwidth and greater than the resolution of the spectrometer.

This constraint can be written in the form

$$\frac{\lambda_s^2}{\Delta\lambda_s} \ll |\Delta z| \ll \frac{\lambda_s^2}{\delta\lambda}. \tag{4.5}$$

In our experiment, we have $\Delta\lambda_s = 8$ nm and $\delta\lambda = 1.2$ nm, so that the restriction on the path unbalancing bounds reads as 82 μm $\ll |\Delta z| \ll$ 546 μm.

These results are the prelude to the FD-OCT measurement, in which the objective is to perform a 1D axial scan of a single layer sample with two reflective facets. Particularly, we probe a $d = 100$ μm thickness microscope glass slide, with group index $n_g \sim 1.5$. Thus, the optical path length is $2n_g d \sim 300$ μm. We measure the spectrum $S(\lambda)$ of the signal s_2 beam with a visible spectrometer. After proper re-sampling to wavenumber k, a Fourier transform procedure[2] is applied to obtain information of the sample.

The 1D FD-OCT measurement performed in our experiment is shown in Fig. 4.5. As explained in Section 3.2.2, the Fourier transform of a single layer sample with two reflective facets must show seven peaks. In our case, only three peaks are observed. This is because the resolution of the spectrometer used ($\delta\lambda$) does not allow to resolve the spectral modulation caused by the sample when $|\Delta z_1|, |\Delta z_2| \ll 82$ μm, with $\Delta z_{1,2}$ being the path length differences corresponding to each of the two facets. Both of them must fulfill the restriction shown in Eq. (4.5).

Despite this, the distance between the peaks located at $z \neq 0$ shown in Fig. 4.5 is twice the optical length of the sample[3] $2n_g d$. The axial resolution of our OCT scheme can be assessed by the bandwidth of the Fourier transform peaks at FWHM, 60 μm. Of course, this value can be readily improved by engineering phase-matching conditions of nonlinear crystals [64, 67, 68, 77] and by spectral shaping [78].

[2] See Appendix G for further details on the FT method employed for OCT.

[3] See Appendix H for a detailed explanation on why the FT of the spectrum of the signal beam shown in Fig. 4.5 shows three peaks, and why the distance between peaks is $2n_g d$.

4.4 Experimental results

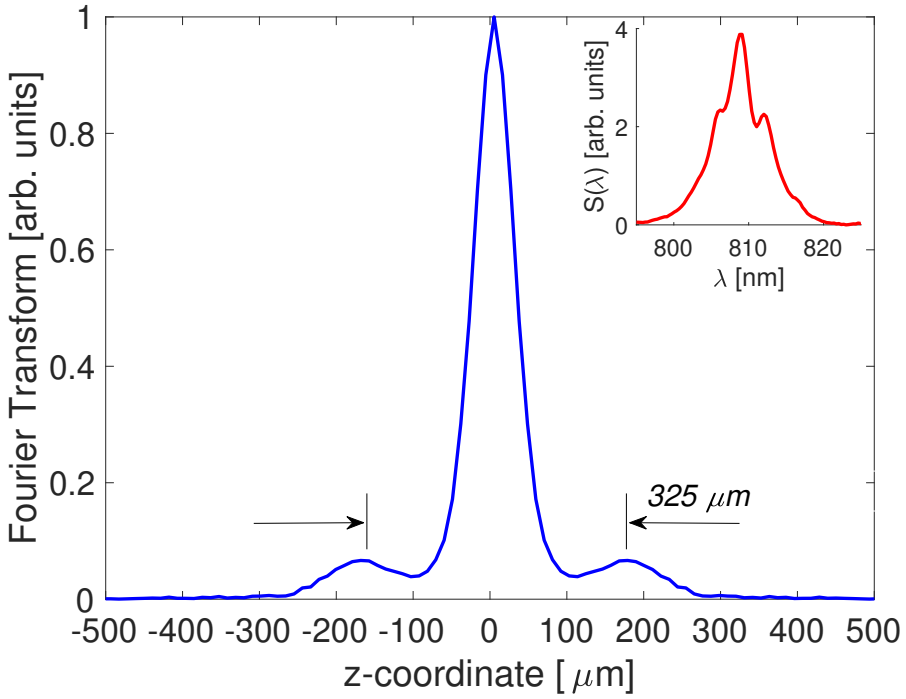

Figure 4.5: Fourier transform of the measured spectrum after resampling it to wavenumbers. The inset shows the measured spectrum $S(\lambda)$. The separation between the two lower peaks corresponds to the measured optical path length of the sample, 325 μm. The inset shows the measured spectrum $S(\lambda)$.

CHAPTER

FIVE

COMPLEMENTARITY RELATIONSHIP IN NONLINEAR INTERFEROMETERS BASED ON INDUCED COHERENCE

This chapter considers a nonlinear interferometer based on induced coherence. It address a fundamental question: how to *measure* and *quantify* the role of the distinguishability of signal photons that originate in different nonlinear crystals and its influence on the degree of first-order coherence induced. The first part of this chapter is devoted to explaining what is the relationship between quantum interference, measured as visibility of a interference pattern, and distinguishability. We introduce and demonstrate a novel scheme to quantify such distinguishability based on the measurement of second-order correla-

tion functions. Surprisingly, this measurement is found to be valid for both the low and high parametric gain regimes of down-conversion. This allows us to write down a complementarity relationship between distinguishability and first-order coherence.

5.1 Introduction

Quantum interference happens when there are several alternatives for an event to happen and there is no way, even in principle, to distinguish between them. This is one of the most profound and fundamental statements coming from quantum mechanics. Richard Feynmann considered quantum interference as the greatest mystery in quantum mechanics [79].

The possible *alternatives* can be identified as different possible spatial *paths* that a quantum entity (i.e., a photon, an atom, etc.) can undergo before reaching a detector. Quantum interference is observed in a detector if, and only if, each quantum detection can NOT be associated with any particular path linking the detector and the quantum source [80]. The gold standard for illustrating this idea is the double-slit experiment, in which interference is only observed if the paths are indistinguishable [81].

The most common way to quantify quantum interference is the visibility of the interference fringes of an interference pattern. On the other hand, path distinguishability is usually associated with the available amount of which-way information. What is interesting is that both quantities are complementary and can be quantitatively related. In diverse interferometric scenarios, simple expressions of the form $D^2 + V^2 = 1$ have been derived [82–84], where D is the distinguishability and V the visibility of the interference pattern.

There are lots of theoretical papers on this subject, however there aren't many experiments. One experiment by Rempe's group is arguably the most important [85–87]. They use a double-slit configuration to measure the interference of Rubidium atom trajectories, and

used as path witness the quantum internal state of the atoms, which can change depending on which path the atoms take. Interestingly, the observation of no interference in this which-way experiment cannot be attributed to the 'back action' of path detection on the atom's momentum, because it is too little to explain the atomic motion. As a result, rather than the uncertainty principle, they attribute it to correlations between the which-way detector and atomic motion.

The concept of distinguishability was given an entirely new perspective when the idea of induced coherence was introduced in the early 1990s. Rather than considering alternatives like the path each of the interfering photons takes, the alternatives are the creation of the photon pairs themselves. The signal photons that are combined in the interferometer, s_1 and s_2, can be generated in different nonlinear crystals. The idler photons, i_1 and i_2, that accompany the corresponding signal photons can act as witnesses of the origin of the signal photons. If the idler photons are perfectly overlapped, there is no information about which crystal the signal photons originate, the signal photons show first-order coherence and we observe interference with high visibility between them. If we can distinguish the origin of the idler photons, and so the origin of the signal photons, there is no induced coherence and we observe no interference between the signal photons.

The idea of induced coherence was put forward and demonstrated in the low parametric gain regime of down-conversion, where paired photons are generated in one nonlinear crystal or the other. In this scenario, the explanation given above is absolutely valid. However, induced coherence is still present in the case of high parametric gain [29, 52], when signal and idler pairs are generated in both crystals simultaneously. In this case the usual explanation is that there is a phase relationship between input and output beams in the second nonlinear crystal that induce coherence between the two signal beams that are made to interfere. Some even discuss the quantum versus non-quantum character of this regime compared to the case of low parametric gain regime.

The question is: *Are two different explanations necessary to describe the physics in both regimes?* In this chapter we will show that this is not the case. We can explain the concept of induced coherence in all regimes with ideas based on information concepts, as it was originally done. We can make use of the explanation given for the low parametric gain regime presented in 1991 [9]. Here we introduce and demonstrate experimentally a new measure of distinguishability that applies to both low and high parametric gain regimes, which is based solely on second-order correlation functions $g_{si}^{(2)}$ between signal and idler photons. This allows us to write an equality of the type $D^2 + V^2 = 1$ for both gain regimes of down-conversion.

We should mention that there have been experiments utilizing quantum erasing of which-way information [88], that needs to measure correlations (coincidence counts) in order to delete path information. In our experiments on induced coherence we always measure singles to observe an interference pattern.

5.2 Induced coherence: a Quantum Information view

Figure 5.1 shows a sketch of an interferometer that makes use of the induced coherence effect. The study of the first-order correlation function $g_{12}^{(1)}$ between signals s_1 and s_2 has been done in detail in Section 2.3.1. The aim here is to investigate the second-order correlation functions $g_{13}^{(2)}$ and $g_{23}^{(2)}$ between signal s_1 and s_2 and the idler i_3 to determine a measurable variable of distinguishability.

Analysis in the low parametric gain regime

Parametric down-conversion efficiency is so low that we can safely assume that paired photons are generated in one nonlinear crystal or in the other, but never simultaneously in both crystals. In this

5.2 Induced coherence: a Quantum Information view

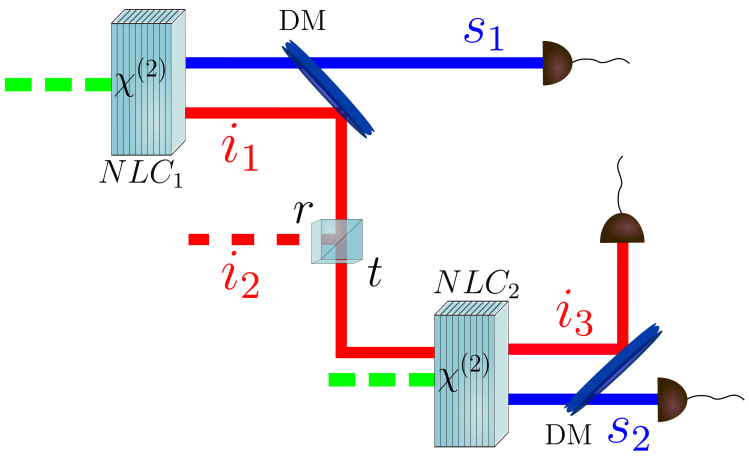

Figure 5.1: Simplified sketch of an induced coherence experimental setup. DM: dichroic mirror; r and t are the reflection and transmission coefficients of a beam splitter that models losses in the idler path. s_1: signal photon generated in the first NL-crystal; s_2: signal photon generated in the second NL-crystal; i_1: idler photon generated in the first NL-crystal; i_2 idler photon generated in the first nonlinear crystal and reflected from the BS; i_3: idler photon generated in the second nonlinear crystal, or generated in the first nonlinear crystal and transmitted at the BS.

scenario, the quantum state of signal-idler photons is

$$|\Psi\rangle_{si} = \frac{1}{\sqrt{2}} |1\rangle_{s_1} |0\rangle_{s_2} \left[r |1\rangle_{i_2} |0\rangle_{i_3} + t |0\rangle_{i_2} |1\rangle_{i_3} \right] + \\ + \frac{1}{\sqrt{2}} |0\rangle_{s_1} |1\rangle_{s_2} |0\rangle_{i_2} |1\rangle_{i_3} . \tag{5.1}$$

The first term corresponds to the generation of the signal-idler pair in the first nonlinear crystal, and the second term corresponds to the generation in the second nonlinear crystal. The quantum state that describes the idler photons in the basis $\{|1\rangle_{i_1} |0\rangle_{i_3}, |0\rangle_{i_1} |1\rangle_{i_3}\}$ is

$$\rho_1 = \begin{pmatrix} |r|^2 & rt^* \\ r^*t & |t|^2 \end{pmatrix}, \tag{5.2}$$

where r and t are the reflectivity and transmissivity values of the beamsplitter that simulate the losses experienced by the idler i_1, with $|r|^2 + |t|^2 = 1$. If the signal and idler photons are generated in the second nonlinear crystal, the quantum state of the idler photons in the same basis is

$$\rho_2 = \begin{pmatrix} 0 & 0 \\ 0 & 1 \end{pmatrix}. \tag{5.3}$$

The quantum state of the witness idler photons is

$$\rho_w = \frac{1}{2}\rho_1 + \frac{1}{2}\rho_2 = \frac{1}{2}\begin{pmatrix} |r|^2 & rt^* \\ r^*t & |t|^2 \end{pmatrix} + \frac{1}{2}\begin{pmatrix} 0 & 0 \\ 0 & 1 \end{pmatrix} = \frac{1}{2}\begin{pmatrix} |r|^2 & rt^* \\ r^*t & 1+|t|^2 \end{pmatrix}. \tag{5.4}$$

The distinguishability D can be defined as the trace distance between the density operators ρ_1 and ρ_2 [84]

$$D = \frac{1}{2}Tr\Big|\rho_1 - \rho_2\Big|. \tag{5.5}$$

The eigenvalues $\lambda_{1,2}$ of

$$\frac{1}{2}(\rho_1 - \rho_2) = \begin{pmatrix} |r|^2/2 & rt^*/2 \\ r^*t/2 & -|r|^2/2 \end{pmatrix}, \tag{5.6}$$

are

$$\lambda_{1,2} = \pm|r| = \pm\sqrt{1-|t|^2}, \tag{5.7}$$

The distinguishability D is

$$D = \frac{1}{2}(|\lambda_1| + |\lambda_2|) = |r| = \sqrt{1-|t|^2}. \tag{5.8}$$

Since the visibility V of the interference fringes of induced coherence experiments in the low parametric gain regime is

$$V = |t|, \tag{5.9}$$

an Englert-type [84] equality of the form

$$V^2 + D^2 = |t|^2 + (1-|t|^2) = 1, \tag{5.10}$$

is fulfilled.

In the Heinsenberg picture, the second-order correlation function $g_{13}^{(2)}$ between signal s_1 and idler i_3, and the second-order correlation function $g_{23}^{(2)}$ between signal s_2 and idler i_3 are [36, 89]

$$g_{13}^{(2)} = 1 + \frac{|t|^2}{1+|t|^2}\frac{B}{R}, \tag{5.11}$$

and

$$g_{23}^{(2)} = 1 + \frac{1}{1+|t|^2}\frac{B}{R}, \tag{5.12}$$

where B is the down-conversion bandwidth and R is the flux rate of paired photons. This expressions are valid for a temporal delay between signal and idler photons smaller than $1/B$. Otherwise, $g_{13}^{(2)} = g_{23}^{(2)} = 1$. Substituting Eqs. (5.11) and (5.12) in Eq. (5.8) we have

$$D = \sqrt{1-|t|^2} = \sqrt{\frac{g_{23}^{(2)} - g_{13}^{(2)}}{g_{23}^{(2)} - 1}}, \tag{5.13}$$

which constitutes a measurable value of the distinguishability D valid for an induced coherence scheme.

Analysis in the general case, including the high and low parametric gain regimes

In order to extend this analysis to the general case of any photon flux, let us consider the single-mode approximation. In this scenario, the Bogoliubov transformations that state the input-output operator relations (see Fig. 5.1) in the first nonlinear crystal are

$$\begin{aligned} \hat{a}_{s_1} &= U\hat{b}_s + V\hat{b}_i^\dagger, \\ \hat{a}_{i_1} &= U\hat{b}_i + V\hat{b}_s^\dagger, \end{aligned} \tag{5.14}$$

with $|U|^2 - |V|^2 = 1$. The idler i_1 interacts with a lossy object, thus

$$\hat{a}_{i_1} \Longrightarrow t\hat{a}_{i_1} + \hat{f}, \tag{5.15}$$

with t being the transmissivity. The operator $\hat{f}$ fulfills $[\hat{f}, \hat{f}^\dagger] = 1 - |t|^2$. The input-output relations in the second nonlinear crystal read

$$\begin{aligned} \hat{a}_{s_2} &= U\hat{c}_s + V\hat{a}^\dagger_{i_1}, \\ \hat{a}_{i_3} &= U\hat{a}_{i_1} + V\hat{c}^\dagger_s. \end{aligned} \tag{5.16}$$

The normalized second-order correlation functions between signal s_1 and the idler photon i_3 $[g^{(2)}_{13}]$ and between signal s_2 and the idler photon i_3 $[g^{(2)}_{23}]$ are

$$g^{(2)}_{13} = \frac{\langle \hat{a}^\dagger_{s_1}\hat{a}^\dagger_{i_3}\hat{a}_{i_3}\hat{a}_{s_1}\rangle}{\langle \hat{a}^\dagger_{s_1}\hat{a}_{s_1}\rangle\langle \hat{a}^\dagger_{i_3}\hat{a}_{i_3}\rangle}, \tag{5.17}$$

$$g^{(2)}_{23} = \frac{\langle \hat{a}^\dagger_{s_2}\hat{a}^\dagger_{i_3}\hat{a}_{i_3}\hat{a}_{s_2}\rangle}{\langle \hat{a}^\dagger_{s_2}\hat{a}_{s_2}\rangle\langle \hat{a}^\dagger_{i_3}\hat{a}_{i_3}\rangle}. \tag{5.18}$$

The expected values can be written as

$$\langle \hat{a}^\dagger_{s_1}\hat{a}_{s_1}\rangle = |V|^2, \tag{5.19}$$

$$\langle \hat{a}^\dagger_{s_2}\hat{a}_{s_2}\rangle = |V|^2\big(1 + |t|^2|V|^2\big), \tag{5.20}$$

$$\langle \hat{a}^\dagger_{i_3}\hat{a}_{i_3}\rangle = |V|^2\big(1 + |t|^2|U|^2\big), \tag{5.21}$$

$$\langle \hat{a}^\dagger_{s_1}\hat{a}^\dagger_{i_3}\hat{a}_{i_3}\hat{a}_{s_1}\rangle = |V|^2\Big[|V|^2 + |t|^2|U|^2(1 + 2|V|^2)\Big], \tag{5.22}$$

$$\langle \hat{a}^\dagger_{s_2}\hat{a}^\dagger_{i_3}\hat{a}_{i_3}\hat{a}_{s_2}\rangle = |V|^2|U|^2\Big[|t|^4(|U|^4 + |V|^4 + 1) + 2|t|^2(|V|^2 - 1) + 1\Big]. \tag{5.23}$$

Substituting these values on Eqs. (5.17) and (5.18), the final expressions of the normalized second-order correlation functions are

$$g^{(2)}_{13} = 1 + \frac{|t|^2|U|^4}{|V|^2\big[1 + |t|^2|U|^2\big]}, \tag{5.24}$$

5.2 Induced coherence: a Quantum Information view

and

$$g_{23}^{(2)} = 1 + \frac{|t|^4|U|^6 + 2|t|^2|U|^4 - 2|t|^4|U|^4 + |U|^2(1-|t|^2)^2}{|V|^2\left[1+|t|^2|V|^2\right]\left[1+|t|^2|U|^2\right]}. \quad (5.25)$$

Finally, substituting Eqs. (5.24) and (5.25) into the definition of the proposed distinguishability D [Eq. (5.8)], we obtain

$$D = \sqrt{\frac{1-(1-|V|^2)|t|^2 - |t|^4|V|^2}{1+2|t|^2|V|^2+|t|^4|V|^4}}, \quad (5.26)$$

which constitutes a measurable distinguishability D value valid for any parametric gain regime.

As detailed in Appendix D, the visibility of the interference pattern in the high parametric gain regime is not equivalent to the degree of coherence $|g_{12}^{(1)}|$, since the flux rate of signal photons s_1 and s_2 may be different. The general expression of the degree of coherence for an induced coherence scheme is [29, 52]

$$g_{12}^{(1)} = |t|\sqrt{\frac{1+|V|^2}{1+|V|^2|t|^2}}. \quad (5.27)$$

It can be easily demonstrated that the following equality is fulfilled

$$D^2 + [g_{12}^{(1)}]^2 = 1, \quad (5.28)$$

using Eqs. (5.26) and (5.27). Figure 5.2 shows some examples of this relationship for different values of the parametric gain. The important point to remark here is that we have derived a complementarity relationship that relates the first-order induced coherence between signal photons s_1 and s_2 and the distinguishability.

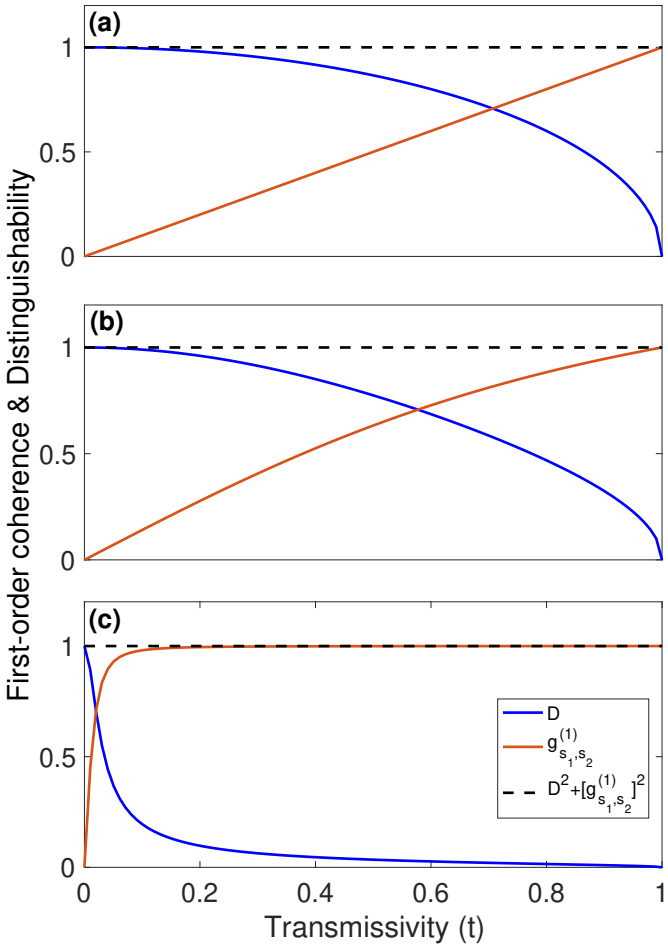

Figure 5.2: Complementarity relationship between the first-order correlation function of signal photons s_1 and s_2, and the distinguishability D, for different values of the parametric gain G. The red solid curves stand for the first-order coherence $g_{12}^{(1)}$; the blue solid line stand for the distinguishability D; the black dashed line stand for the sum $D^2 + [g_{12}^{(1)}]^2$. (a) $G = 0.01$; (b) $G = 1.7$ and (c) $G = 10$.

5.3 Experimental setup

The experimental setup is depicted in Fig. 5.3. It is essentially the same setup used in Ref. [56], which is explained in detail in Chapter 3. The main difference is that now the idler photons are measured to perform coincidence measurements with the signal photons. Let us summarize the key elements of the experiment, with a special emphasis on how we perform coincidence measurements.

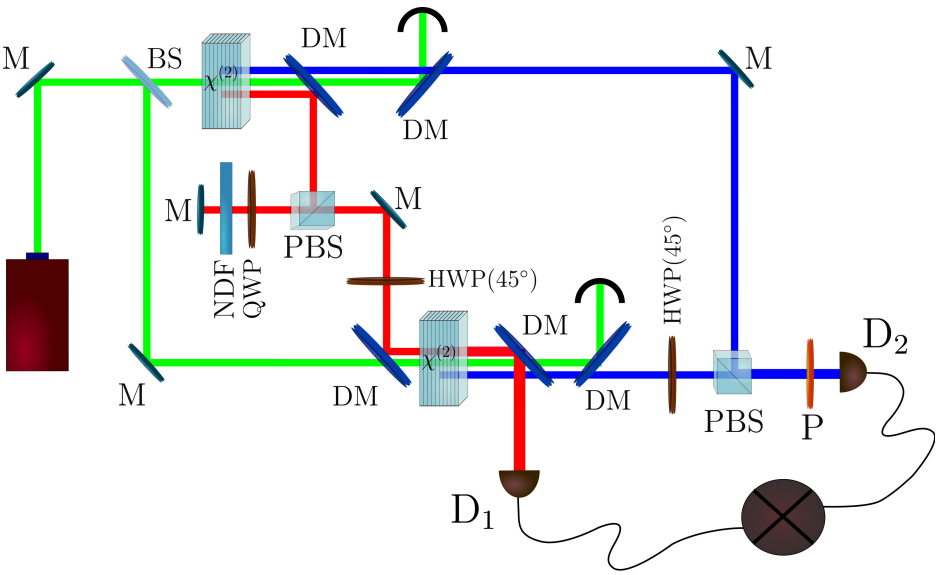

Figure 5.3: Experimental setup aimed at observing optical coherence and quantum correlations. In order to measure the first-order coherence function, we only use one the single-photon detector D_2. For measuring second-order correlation functions, we use detectors D_1 and D_2.

Our setup is essentially a nonlinear interferometer made up of two identical sources separated and pumped by the same pump beam. The pump is the continuous-wave (CW) Verdi V10 model (Coherent), with a central wavelength of $\lambda_p = 532$ nm. The PDC sources

are two 20-mm-long PPLN crystals mounted in ovens, to guarantee the necessary phase matching to generate the signal-idler pair of photons with maximum efficiency. The central wavelengths of the signal and the idler are $\lambda_s = 810$ nm and $\lambda_i = 1550$ nm, respectively. The idler photon generated in the first crystal experiences losses introduced by a neutral density filter, before being injected into the second crystal. The idler photons generated in both crystals (which are ideally indistinguishable) are coupled to a single-mode fiber and measured by the D_1 detector. On the other hand, the signal photons generated in both crystals are recombined in the last polarizing beam splitter PBS before being detected by D_2.

The goal is to evaluate the second-order correlation functions $g_{13}^{(2)}$ and $g_{23}^{(2)}$ by measuring coincidences (simultaneous detection) between signal s_1 and idler i_3 and between signal s_2 and idler i_3, as function of the losses experienced by the idler i_1. In our case, the measurements of coincidences must be done between photons with differing central wavelengths, which implies the use of two separate and different single-photon detectors, one operating in the visible range (signal) and the other in the near infrared (idler). Because the electronics, response times and detection windows of both detectors are obviously different, the challenge will be to devise a way to measure coincidences in both.

To do this, it is necessary to understand how both single-photon detectors operate. We use two single-photon avalanche photodiodes (APD), which are semiconductor-based photodetectors. The working principle of APD's is based on the photoelectric effect: the absorbed photons excite the carriers (electrons and holes) from the thin semiconductor film layer. APD's operate with a relatively high reverse voltage (typically tens or hundreds of volts), that allows the carriers to be strongly accelerated in the strong internal electric field, so that they easily generate secondary carriers. This avalanche process amplifies the photocurrent by a significant factor, also called *gain*. The signal photons are detected by a silicon-based single-photon counting module SPCM-AQRH-14-FC (Perkin-Elmer), that detects single

photons over the wavelength range of 400 nm to 1060 nm. The photon detection efficiency at 810 nm is approximately 60 %. The signal photons are coupled to the detector via single mode fiber. Each photon detection generates a 30 ns width TTL-level electronic signal that is available at the output BNC connector.

The idler photons are detected by a single-photon detection module id201 (idQuantique) based on indium gallium arsenide (InGaAs). This module detects IR photons with an efficiency up to 25 %. The idler photons are coupled via single mode fiber and each detection generates a TTL-type electronic signal of 100±10 ns width. It has an adjustable detection pulse width from 2.5 ns to 100 ns and a tunable delay between 0 and 25 ns.

The coincidence measurements are performed in the following way: the Perkin-Elmer output detection is used as the input trigger for the idler photon detection. As a result, an idler count is directly a coincidence. To make that happen, the photons' arrival times at their detectors must be fine-tuned. Not only that, but we must additionally account for the detectors' response times as well as the delay provided by the BNC connection that links them.

Figure 5.4 shows a schematic with the time lines of both photons and the id201 detector. The time of arrival of the idler photon to the detector needs to be adjusted so that the condition: $t_{idler} \geq t_{signal} + 8$ ns, is fulfilled. To do this, we must use the right fiber and coaxial cable lengths. The signal and the idler photons' single mode optical fiber lengths in the experiment are $l_{signal} = 2$ m and $l_{idler} = 12$ m, respectively. The length of the BNC coaxial cable that connects both APD's is $l_{BNC} = 0.40$ m.

5.4 Experimental results

The goal is to measure the second-order correlation function between signal and idler photons generated in the two SPDC crystals, $g^{(2)}_{13}$ and $g^{(2)}_{23}$, as a function of the losses introduced in the idler i_1 path. The

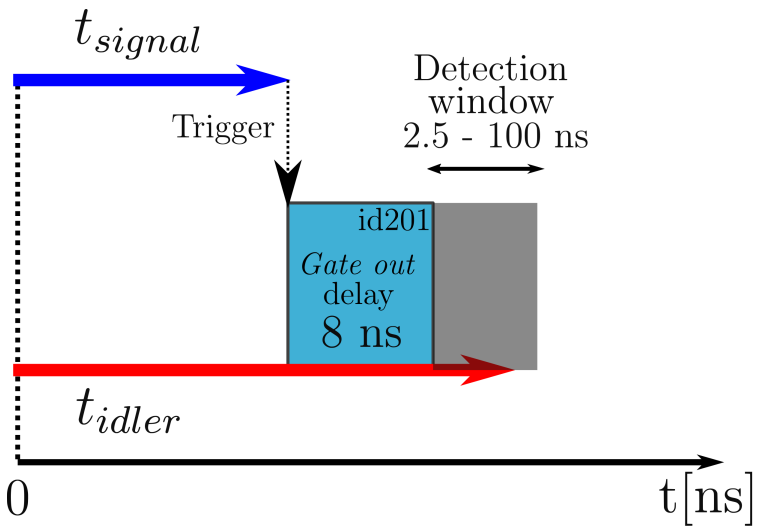

Figure 5.4: Temporal lines for both photons and the idQuantique id201 detector. The detection of the signal photon generates an electronic signal that serves as in input trigger to detect a coincidence with the id201 detector. To account for a coincidence, the time of arrival t_{idler} of the idler photon to the detector needs to be adjusted so that it *falls* within the detection window.

theoretical expressions are shown in Eqs. (5.11) and (5.12). Now the question is: *how can such functions be evaluated using coincidence measurements?*

Let us answer it step by step. First, in an experimental setup the rate of coincidence counts R_{13} in a detection time window T_R is [90]

$$\begin{aligned} R_{13} &= \eta_{13} \int d\tau < a^{\dagger}_{s_1}(t) a^{\dagger}_{i_3}(t+\tau) a_{i_3}(t+\tau) a_{s_1}(t) >= \\ &= \frac{\eta_{13}}{\eta_1 \eta_3} R_1 R_3 T_R \Big[1 + \frac{T_c}{T_R} \frac{B}{R} \Big], \end{aligned} \tag{5.29}$$

where η_{13} is the efficiency of coincidence detection, $R_{1,3}$ is the measured singles flux rate, $\eta_{1,3}$ are singles efficiencies, T_R is the detection

time and T_c is the coherence time (inverse bandwidth) of the paired signal-idler photons. We write $g_{13}^{(2)}(\tau) = 1 + \gamma(\tau)$. Therefore

$$\gamma(0) = \frac{R_{13} - \eta R_1 R_3 T_R}{\eta R_1 R_3 T_c}, \tag{5.30}$$

where $\eta = \eta_{13}/(\eta_1\eta_3)$. The value of $\gamma(0)$ and hence the correlation function $g_{13}^{(2)}(0)$ can be assessed using the experimental values of R_{13}, R_1, R_2 and R_3. The procedure is repeated for different values of the reflectivity r of the neutral density filter introduced in the idler path.

Furthermore, Eqs. (5.29) and (5.30) show that given a constant temporal detection window T_R, flux rates should be as low as possible ($RT_R << 1$) and total detection windows (T_0) as long as possible ($T_0 >> T_R$). The experimental parameters are set to be:

- Detection (coincidence) window width: $T_R = 2.5$ ns.
- Total detection window width: $T_0 = 30$ s.
- Trigger (signal) flux rate: $R_1 = 2000$ Hz.
- Idler singles flux rate: $R_3 = 2000$ Hz.

Figure 5.5 illustrates the coincidence counts R_{13} and R_{23} measured as a function of the delay between the signal photons and the idler, for different values of the reflection coefficient r introduced by the NDF. Signal s_1 and idler coincidences are affected by the value of r, which has a direct impact on the signal-idler correlation. On the other hand, the value of r is observed not to have any effect on the coincidences between signal s_2 and idler i_3, as expected.

Finally, using Eqs. (5.29) and (5.30), the normalized second-order correlation functions $g_{13}^{(2)}$ and $g_{23}^{(2)}$ can be assessed from the maximum values of R_{13} and R_{23} and the singles flux rates R_1, R_2 and R_3, for each reflection coefficient r. Figure 5.6 shows both the experimental data and the theoretical curves, showing a very good agreement.

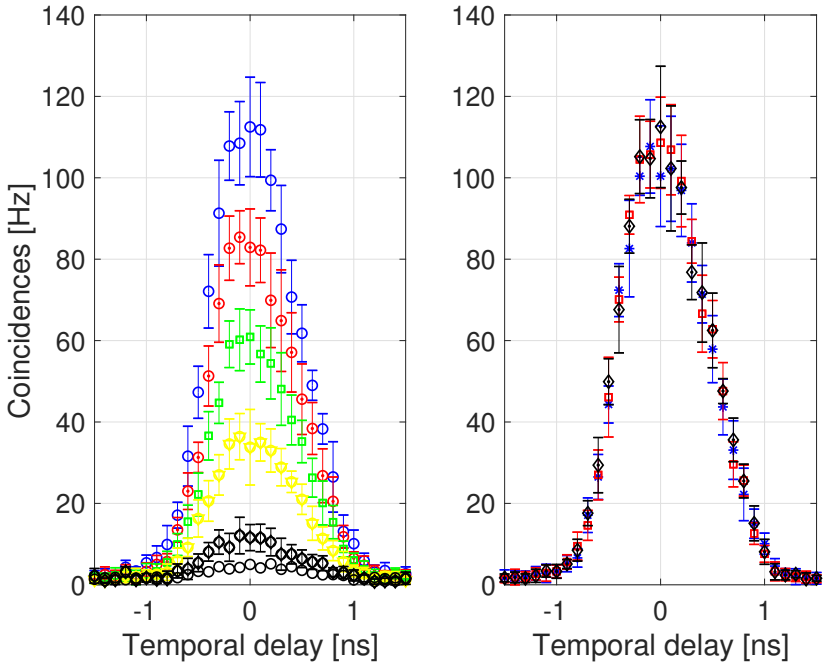

Figure 5.5: Measured coincidences counts (R_{12}) for different values of the reflection coefficient (r) as a function of the temporal delay. LEFT: Coincidences counts between signal s_1 photons and idler photons. The different curves correspond to different values of the idler losses: $|r| = 1.0$; $|r| = 0.8$; $|r| = 0.6$; $|r| = 0.4$; $|r| = 0.2$ and $|r| = 0$. RIGHT: Coincidences counts rate between signal s_2 photons and idler photons. The different curves correspond to different values of the idler losses: $|r| = 1.0$; $|r| = 0.5$ and $|r| = 0$.

Once we have measured the second order correlation functions dependence on the reflection coefficient, we can calculate the proposed distinguishability according to Eq. (5.13). Figure 5.7 shows both theoretical and experimental values of visibility (red) and distinguishability (blue) as a function of the reflection coefficient. The experimental results are in good agreement with the theory.

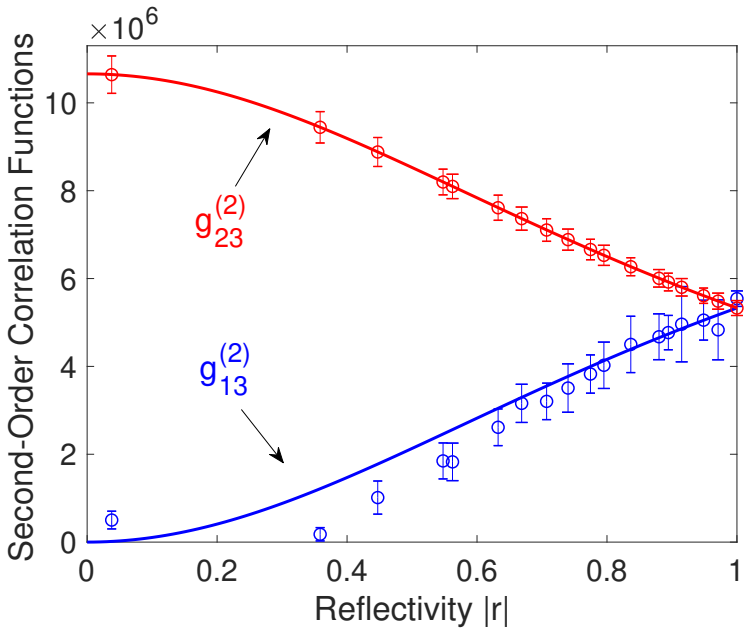

Figure 5.6: Normalized second-order correlation functions ($g^{(2)}_{13}$ and $g^{(2)}_{23}$) as a function of the reflection coefficient (r). The blue dots correspond to calculated values from experimental data of $g^{(2)}_{13}$ and the red ones for $g^{(2)}_{23}$. The theoretical curves [Eqs. (5.17) and (5.18)] make use of the measured values $R_{1,2} = 2000$ Hz and $B = 1/580$ fs. The error bars designate the standard deviation of the experimental measures.

In conclusion, we have demonstrated a profound link between coherence (first-order correlation function) and correlations (second-order correlation function). We have measured the dependence of the normalized second-order correlation functions ($g^{(2)}_{13}$ and $g^{(2)}_{23}$) with the reflection coefficient r that inroduce loss. This loss also tunes the degree of coherence between signal photons. Distinguishability can be quantified by how much difference there is between $g^{(2)}_{13}$ and $g^{(2)}_{23}$, that also determines the amount of coherence present between signal pho-

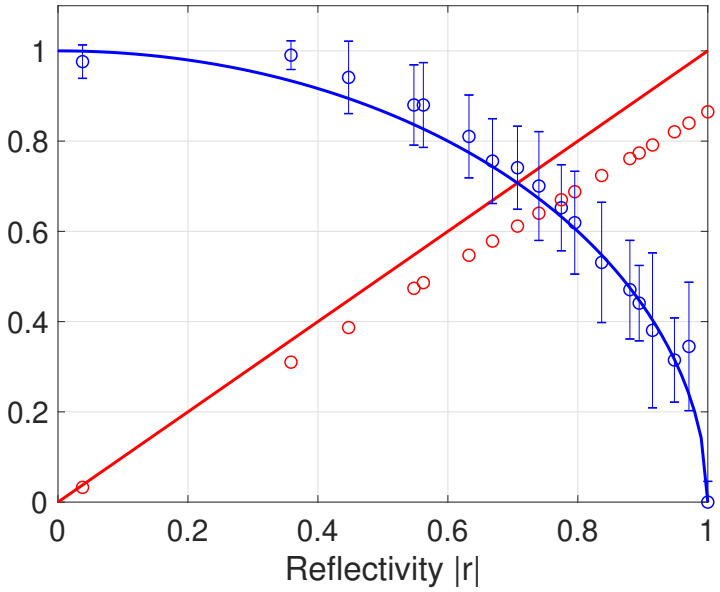

Figure 5.7: Experimental and theoretical relationship between the interference pattern visibility and the proposed distinguishability with the reflectivity. (BLUE) Distinguishability. Circles: experimental data; Solid line: theoretical prediction given by Eq. (5.13). (RED) Visibility of the interference fringes. Circles: experimental data; Solid line: theoretical prediction given by Eq. (5.9).

tons. This is valid for all regimes of parametric down-conversion. The result obtained constitute a beautiful bridge between two fundamental aspects on quantum optics: coherence and correlations.

CHAPTER

SIX

INDUCED COHERENCE: STIMULATED EMISSION VS QUANTUM DISTINGUISHABILITY

In this chapter we consider the role of two explanations of the origin of induced coherence: stimulated emission and quantum distinguishability. There is an ongoing discussion about what is the *true role* of both explanations [19, 20]. We present experiments that show that quantum erasure of distinguishing information in a nonlinear interferometer based on the induced coherence effect can produce interference between signal photons, independently if there is stimulated emission or not. However, we need to consider coincidence measurements. In the last section we present some calculations that seem to suggest that stimulated emission should be present to observe induced coherence, even in the low parametric gain regime.

6.1 Introduction

In 1991 Zou, Wang and Mandel [9] demonstrated the effect of induced coherence between two signal photons, s_1 and s_2, that originate in different second-order nonlinear crystals. They claimed [91] that their experiments demonstrated that was possible to induce coherence that was not accompanied by induced emission. In current words, the induced coherence between s_1 and s_2 photons took place even though there was no stimulated emission on the second nonlinear crystal.

The observation of induced coherence was attributed to the lack of distinguishing information concerning in which crystal the signal photons are generated. If the idler photons that accompany signal photons s_1 and s_2 are made indistinguishable, we have no information on the origin of the signal photons and therefore they show first-order coherence. As we have demonstrated in the previous chapter, this kind of explanation can be summarized elegantly by means of a complementarity relation between first-order coherence and path distinguishability.

In an analysis of 2015 [19], it is said that interferometers based on induced coherence *rely on stimulated, rather than spontaneous, emissions from the wavelength-converting phase conjugator*. When one analyzes induced coherence from the viewpoint of the Heisenberg approach, this seems to be an evident consequence. In the analysis, as shown in Chapter 2, one needs to consider parametric amplification, or stimulated emission, in the second nonlinear optical crystal. However, from the viewpoint of Schrödinger's approach, in the low parametric gain regime one can analyze the induced coherence phenomenon without considering the existence of stimulated emission.

It might be possible that stimulated emission in the second nonlinear crystal, and quantum distinguishability of the origin of signal photons are just two complementary explanations for the same physical effects. In other words, we need stimulated emission to observe quantum distinguishabilty, and thus first-order coherence. The presence of both effects might be inseparable. Research in the group of

Prof. Anton Zeilinger [20] does not follow this line of thinking. They consider that quantum distinguishability is the key element required to observe stimulated emission, and they claim that stimulated emission is not responsible of the induce of mutual coherence between the signal photons.

Here we want to contribute to this debate by showing that we can observe mutual coherence between the signal photons eliminating the possibility of having stimulated emission in the second nonlinear crystal. We will show that if we erase the distinguishability on the origin of the signal photons introduced by the idler photons, we induce mutual coherence. However, we should consider coincidence signal-idler measurements to achieve this, instead of measuring only signal photons, a highly relevant characteristic of induced coherence experiments. This is an important drawback towards resolving the debate. However, we still think our experiments can illuminate some aspects of the debate.

6.2 Mathematical analysis in the Schrödinger picture

Figure 6.1 shows a simplified sketch of the experimental setup. The aim is to investigate the second-order correlation function $g^{(2)}$ between the signal and idler photons as a function of the idler i_1 polarization state, and the losses it suffers. To do so we rotate, with the help of a polarizer, the polarization of the idler photon i_1 an angle α. Losses (value of transmissivity t) are introduced with a neutral density filter (NDF). Signal-idler coincidence measurements are performed to study the visibility of the interference pattern depending on the angle α and the value of t.

The polarizer located in the idler i_1 path rotates its linear polarization an angle α. This means that the polarization remains unchanged for $\alpha = 0°$ and is rotated to an orthogonal state for $\alpha = 90°$. The PDC process is Type-0, the pump, signal and idler all have the

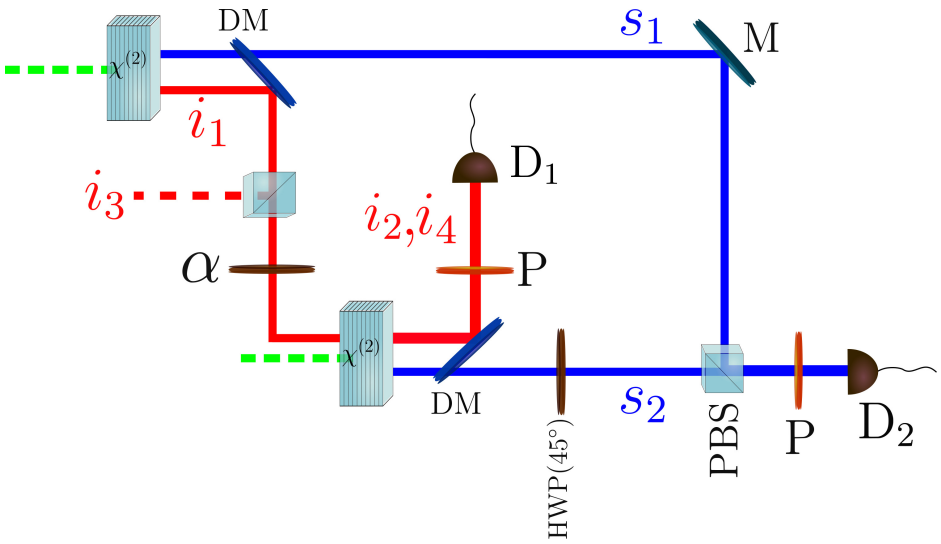

Figure 6.1: Simplified sketch of the experimental setup. The signal and idler beams are represented by the blue and red solid lines, respectively. α: angle of polarization rotation; NDF: gradual neutral density filter; DM: dichroic mirror; HWP: half-wave plate; P: polarizer; D_1: near infrared detector; D_2: visible detector; PBS: polarizing beam splitter; M: mirror.

same vertical polarization. As a result $\alpha = 0°$ leaves the vertical polarization of i_1 invariant, while $\alpha = 90°$ rotates its polarization to horizontal.

The polarizers P located in front of the detectors $D_{1,2}$ project both signal and idler photons to a diagonal or anti-diagonal polarization state. The half-wave plate located in the path of the signal photon generated in the second nonlinear crystal rotates its polarization to horizontal, allowing its transmission through the final polarizing beam splitter (PBS).

6.2.1 Case I: induced coherence with stimulated emission

The polarization of the idler i_1 after the polarizer is $\alpha = 0°$, the polarizer does not change the polarization of the idler photons. This case is equivalent to a *standard* induced coherence scheme. We use the Schrödinger approach in the low parametric gain regime to analyze the experiment. The quantum state of signal-idler pairs is

$$\begin{aligned}|\Psi\rangle = \frac{1}{\sqrt{2}}\Big\{ & t|1\rangle_{s_1}|0\rangle_{s_2}|1\rangle_{i_2}|0\rangle_{i_3}\exp\Big(i\varphi_{s_1}+i\varphi_{i_1}\Big)+ \\ & +r|1\rangle_{s_1}|0\rangle_{s_2}|0\rangle_{i_2}|1\rangle_{i_3}\exp\Big(i\varphi_{s_1}+i\varphi_{i_3}\Big)\Big] \\ & +|0\rangle_{s_1}|1\rangle_{s_2}|1\rangle_{i_2}|0\rangle_{i_3}\exp\Big(i\varphi_{s_2}+i\varphi_{i_2}\Big)\Big\}\end{aligned} \tag{6.1}$$

where r and t are the reflection and transmission coefficients associated to the losses in the idler path, and φ_{s_1}, φ_{s_2}, φ_{i_1}, φ_{i_2} and φ_{i_3} are the phases acquired by photons during propagation.

Photons s_1 and s_2 show orthogonal polarization. We project the signal photons into diagonal ($|1\rangle_{D_s} = [|1\rangle_{H_s} + |1\rangle_{V_s}]/\sqrt{2}$) and anti-diagonal ($|1\rangle_{A_s} = [|1\rangle_{H_s} - |1\rangle_{V_s}]/\sqrt{2}$) polarization states. We project the idler photons into an equivalent basis. We have

$$\begin{aligned}|\Psi\rangle = & \frac{1}{2\sqrt{2}}\Big[t\exp\Big(i\varphi_{s_1}+i\varphi_{i_1}\Big)+\exp\Big(i\varphi_{s_2}+i\varphi_{i_2}\Big)\Big]|1\rangle_{D_s}|1\rangle_{D_i}|0\rangle_{i_3} \\ & +\frac{1}{2\sqrt{2}}\Big[t\exp\Big(i\varphi_{s_1}+i\varphi_{i_1}\Big)-\exp\Big(i\varphi_{s_2}+i\varphi_{i_2}\Big)\Big]|1\rangle_{A_s}|1\rangle_{A_i}|0\rangle_{i_3}+ \\ & +\frac{1}{2\sqrt{2}}\Big[t\exp\Big(i\varphi_{s_1}+i\varphi_{i_1}\Big)+\exp\Big(i\varphi_{s_2}+i\varphi_{i_2}\Big)\Big]|1\rangle_{D_s}|1\rangle_{A_i}|0\rangle_{i_3}+ \\ & +\frac{1}{2\sqrt{2}}\Big[t\exp\Big(i\varphi_{s_1}+i\varphi_{i_1}\Big)-\exp\Big(i\varphi_{s_2}+i\varphi_{i_2}\Big)\Big]|1\rangle_{A_s}|1\rangle_{D_i}|0\rangle_{i_3}+ \\ & +\frac{r}{\sqrt{2}}\exp\Big(i\varphi_{s_1}+i\varphi_{i_3}\Big)|1\rangle_{s_1}|0\rangle_{i_2}|1\rangle_{i_3}.\end{aligned} \tag{6.2}$$

The probability to measure a coincidence between a signal photon with diagonal polarization, or anti-diagonal polarization, and an idler

photon with diagonal or anti-diagonal polarization, is

$$P_{D_s,D_i} = \frac{1}{8}\Big[1 + |t|^2 + 2|t|\cos\Big(\Delta\varphi_s + \Delta\varphi_i + \varphi_t\Big)\Big], \quad (6.3)$$

$$P_{A_s,A_i} = \frac{1}{8}\Big[1 + |t|^2 - 2|t|\cos\Big(\Delta\varphi_s + \Delta\varphi_i + \varphi_t\Big)\Big], \quad (6.4)$$

$$P_{D_s,A_i} = \frac{1}{8}\Big[1 + |t|^2 + 2|t|\cos\Big(\Delta\varphi_s + \Delta\varphi_i + \varphi_t\Big)\Big], \quad (6.5)$$

$$P_{A_s,D_i} = \frac{1}{8}\Big[1 + |t|^2 - 2|t|\cos\Big(\Delta\varphi_s + \Delta\varphi_i + \varphi_t\Big)\Big], \quad (6.6)$$

where the transmissivity is $t = |t|\exp(i\varphi_t)$, $\Delta\varphi_s = \varphi_{s_1} - \varphi_{s_2}$ and $\Delta\varphi_i = \varphi_{i_1} - \varphi_{i_2}$. The visibility of the interference pattern of coincidence measurements as a function of $\Delta\varphi_s$ is

$$V = \frac{P^{max}_{D_s,Di} - P^{min}_{D_s,D_i}}{P^{max}_{D_s,D_i} + P^{min}_{D_s,D_i}} = \frac{2|t|}{1 + |t|^2}, \quad (6.7)$$

similarly for all other cases. On the other hand, the probability to detect signal photons with diagonal polarization is

$$P_{D_s} = P_{D_s,A_s} + P_{D_s,A_i} + \frac{|r|^2}{4} =$$
$$= \frac{1}{4}\Big[1 + |t|^2 + 2|t|\cos\Big(\Delta\varphi_s + \Delta\varphi_i + \varphi_t\Big)\Big] + \frac{|r|^2}{4}. \quad (6.8)$$

The visibility V_s of the interference fringes is

$$V_s = |t|, \quad (6.9)$$

which corresponds to the well-known induced coherence effect.

6.2.2 Case II: induced coherence without stimulated emission

The polarization of the idler i_1 is rotated from vertical to horizontal with a half-wave plate (HWP). In this way, there is no stimulated

emission at the second nonlinear crystal. Note that the parametric down-conversion process is Type-0, requiring vertical polarizations of all waves for the process to occur, so that a photon with horizontal polarization passes through the crystal without participating in the down-conversion process.

The quantum state of signal-idler pairs is now

$$\begin{aligned}|\Psi\rangle = \frac{1}{\sqrt{2}}\Big\{ & t|1\rangle_{s_1}|0\rangle_{s_2}|0\rangle_{i_2}\,|1\rangle_{i_4}|0\rangle_{i_3}\exp\Big(i\varphi_{s_1}+i\varphi_{i_1}\Big)+\\ & +r|1\rangle_{s_1}|0\rangle_{s_2}|0\rangle_{i_2}|0\rangle_{i_4}|1\rangle_{i_3}\exp\Big(i\varphi_{s_1}+i\varphi_{i_3}\Big)+\\ & +|0\rangle_{s_1}|1\rangle_{s_2}|1\rangle_{i_2}|0\rangle_{i_4}|0\rangle_{i_3}\exp\Big(i\varphi_{s_2}+i\varphi_{i_2}\Big)\Big\}.\end{aligned} \tag{6.10}$$

We project the signal and idler photons into diagonal and anti-diagonal polarization states. We have

$$\begin{aligned}|\Psi\rangle = & \frac{1}{2\sqrt{2}}\Big[t\exp\Big(i\varphi_{s_1}+i\varphi_{i_1}\Big)+\exp\Big(i\varphi_{s_2}+i\varphi_{i_2}\Big)\Big]|1\rangle_{D_s}|1\rangle_{D_i}|0\rangle_{i_3}\\ & -\frac{1}{2\sqrt{2}}\Big[t\exp\Big(i\varphi_{s_1}+i\varphi_{i_1}\Big)+\exp\Big(i\varphi_{s_2}+i\varphi_{i_2}\Big)\Big]|1\rangle_{A_s}|1\rangle_{A_i}|0\rangle_{i_3}\\ & -\frac{1}{2\sqrt{2}}\Big[t\exp\Big(i\varphi_{s_1}+i\varphi_{i_1}\Big)-\exp\Big(i\varphi_{s_2}+i\varphi_{i_2}\Big)\Big]|1\rangle_{D_s}|1\rangle_{A_i}|0\rangle_{i_3}\\ & +\frac{1}{2\sqrt{2}}\Big[t\exp\Big(i\varphi_{s_1}+i\varphi_{i_1}\Big)-\exp\Big(i\varphi_{s_2}+i\varphi_{i_2}\Big)\Big]|1\rangle_{A_s}|1\rangle_{D_i}|0\rangle_{i_3}\\ & +\frac{r}{\sqrt{2}}\,|1\rangle_{s_1}|0\rangle_{i_2}|1\rangle_{i_3}\exp\Big(i\varphi_{s_1}+i\varphi_{i_3}\Big)\Big].\end{aligned} \tag{6.11}$$

The visibility of the interference pattern of coincidence measurements as a function of $\Delta\varphi_s$ is again

$$V=\frac{P^{max}_{D_s,Di}-P^{min}_{D_s,D_i}}{P^{max}_{D_s,D_i}+P^{min}_{D_s,D_i}}=\frac{2|t|}{1+|t|^2}, \tag{6.12}$$

similarly for all other cases.

On the other hand, the probability to detect signal photons with diagonal polarization is

$$P_{D_s} = P_{D_s,A_s} + P_{D_s,A_i} + \frac{|r|^2}{4} = \frac{1}{2}. \tag{6.13}$$

The visibility V_s of the interference fringes is $V_s = 0$. There is no induced coherence effect.

6.3 Experimental setup

The experimental setup is depicted in Fig. 6.2. It is essentially the same setup described in detail in Chapters 3 and 5, with some subtle differences regarding idler i_1 and the experimental arrangement to measure coincidences.

A CW pump laser Verdi V10 (Coherent) with central wavelength $\lambda_p = 532$ nm illuminates two identical 20-mm-long PPLN crystals. Signal and idler photons are generated with central wavelengths $\lambda_s = 810$ nm and $\lambda_i = 1550$ nm, respectively. The signal photons are detected by a silicon-based APD SPCM-AQRH-14-FC (Perkin-Elmer). The idler photons are detected by an indium gallium arsenide (InGaAs) avalanche photodiode id201 (idQuantique). The polarizer located in the idler i_1 path allows to rotate its polarization with an angle α. The gradual neutral density filter (NDF) introduces losses, characterized by a certain transmissivity t. The polarizers P placed in front of the single-photon detectors $D_{1,2}$ project the photons into diagonal or anti-diagonal polarization states.

The method for measuring coincidences between signal and idler photons is different from the one described in Chapter 5. This time, we use a coincidence counter Abacus AB1004 (Tausand). It is an electronic coincidence unit with four BNC type inputs to which up to four distinct detectors' electronic output TTL signals can be directly attached. The coincidences are counted by means of edge detection, i.e. reading the instant where a rising edge of an electronic input arrives within the coincidence window. As a result, duplicate counting

6.3 Experimental setup

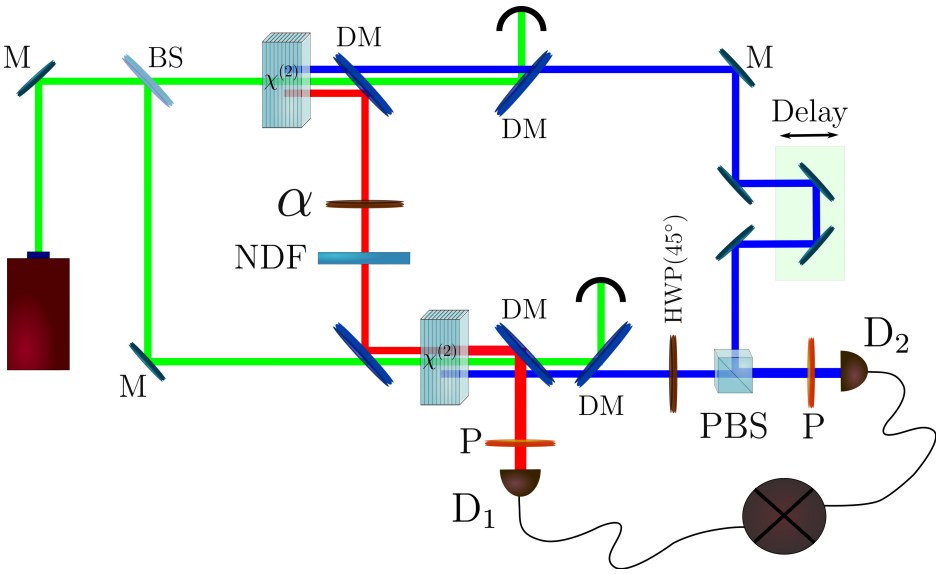

Figure 6.2: Experimental setup proposal for measuring the visibility of the signal-idler coincidences. M: mirror; BS: beam splitter; DM: dichroic mirror; α: rotation angle introduced by a polarizer; NDF: gradual neutral density filter; P: polarizer; PBS: polarizing beam splitter; $HWP(45°)$: half-wave plate at 45 ° to rotate the polarization of signal s_2 from linear vertical to horizontal; D_1: id201 idQuantique; D_2: SPCM-AQRH-14-FC Perkin-Elmer.

coincidences caused by differing electronic pulse widths emitted by various detectors are avoided. Furthermore, this device can measure coincidences with 5 ns resolution and includes a variety of adjustable settings to maximize coincidence detections, such as sampling time, sleep time, delays, etc.

The parameters that characterize our experiment are set to be:

- Coincidence window width: $T_R = 5$ ns.
- Signals flux rate: $R_{s_1} = R_{s_2} = 180$ kHz.
- Idler flux rate: $R_{i_1} = R_{i_2} = 20$ kHz.

To enhance coincidences, the Abacus device permits a time delay sweep between electronic pulses from -100 ns to 100 ns. As a result, the length of the fibers is not crucial in this scenario, as it can be readily rectified by adjusting the delay. In the experimental data reported in the following section, the delay between the electronic pulses is set to the value that offers the largest number of coincidences.

The ultimate goal of the experimental measurements is to investigate the visibility of the coincidence fringes. To do this, it is necessary to scan the phase of one of the two arms of the interferometer. That is why two mirrors located in the signal s_1 path are mounted on top of a Thorlabs Z806 translation stage, which allows to perform steps of 30 nm along 6 mm.

6.4 Experimental results

The objective of this section is to present the main results of the visibility of the coincidence fringes for the two cases of interest explained in Section 6.2: $\alpha = 0°$ and $\alpha = 90°$. In addition, we show the visibility results of the singles for both cases.

First, we characterize the spectra of the signal photons generated from both crystals to ensure that their emission is as close to equal in terms of central wavelength and intensity as possible. The spectra of both signal photons were measured using the Horiba Jobin Yvon MicroHR monochromator, as shown in Fig. 6.3. Both emissions have the same amplitude and are centered at 809.6 nm.

The spectra of the idler photons could not be characterized due to the lack of a spectrometer for such wavelength range or an optical spectrum analyzer. Despite this, we can guarantee that both idler photons are coupled to single mode fiber with the same single counts and that they will be centered at 1552.3 nm due to energy and momentum conservation with the signal and pump waves.

The polarization of the idler i_1 generated in the first nonlinear crystal is linear and vertical. The cases of interest that concern us

6.4 Experimental results

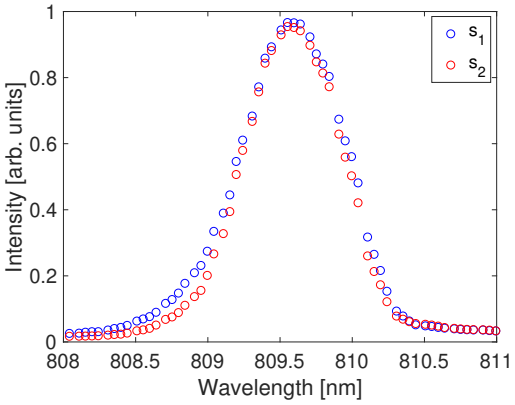

Figure 6.3: Measured spectrum of the signal s_1 and s_2 photons. The spectra are centered at 809.6 nm with a bandwidth of 0.8 nm at full width at half maximum (FWHM).

involve rotating this polarization with an angle α. Experimentally we do this with a half-wave plate set at angle θ, so that $\alpha = 2\theta$. So that, if we want to rotate the polarization of idler i_1 by $\alpha = 90°$, the HWP will be set at $\theta = 45°$.

Both signal and idler photons are projected onto a diagonal polarization state before detection. For the sake of simplicity, in the experimental setup (Fig. 6.2) description we exemplify it with a polarizer P. But actually this diagonal polarization projection is done by a half-wave plate at 22.5° followed by a polarizing beam splitter. In the same way, if the desired polarization projection is anti-diagonal, the half-wave plate is at -22.5°. The results presented below are projecting both signal and idler photons into a diagonal polarization state.

6.4.1 Case I: induced coherence with stimulated emission

This scenario corresponds to the usual induced coherence case. The half-wave plate located in the idler i_1 path is set at $\theta = 0°$, so that its polarization is unchanged. To verify that we are indeed observing the induced coherence effect, we will first look at whether we observe the linear dependence of the visibility of the singles with the losses introduced by the neutral density filter t. To do so, we use the Perkin-Elmer to measure singles while scanning the phase of one arm of the interferometer in 60-nm steps.

Figure 6.4(a) depicts the experimental relationship of the signals interference pattern and the transmissivity of the neutral density filter located in the idler i_1 path. The insets show some examples of the interference pattern measured by scanning the phase in a small region (~ 4 μm) around the point of maximum visibility. The maximum visibility observed is $V = 83\%$.

Figure 6.4(b) depicts the experimental relationship of the coincidence fringes and the transmissivity of the neutral density filter located in the idler i_1 path. The insets show some examples of the coincidences fringes measured by scanning the phase in a small region ($\sim$4 μm) around the point of maximum visibility. The coincidence window set at the coincidence counter Abacus AB1004 is $T_R = 5$ ns, and the total temporal window detection is $T_0 = 3$ s. The maximum visibility observed is $V = 92\%$.

6.4.2 Case II: induced coherence without stimulated emission

The polarization of idler i_1 is rotated to horizontal polarization. The half-wave plate located in its path is set at $\theta = 45°$, converting its polarization to linear horizontal. In this case the signal photons show no induced coherence, thus the visibility of the interference fringes is null for each value t of the NDF transmissivity.

6.4 Experimental results

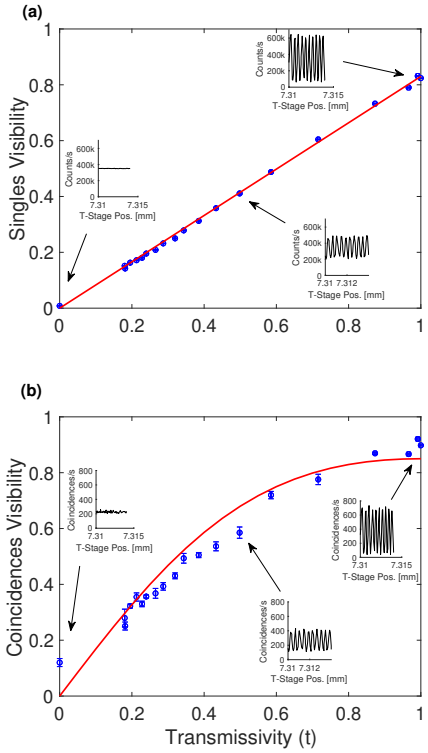

Figure 6.4: (a) Experimental relation between the singles visibility of the interference pattern and the transmissivity of the simulated sample t. (b) Experimental relation between the visibility of the coincidence fringes and the transmissivity of the simulated sample t. Blue dots correspond to the experimental measurements, while the red solid curve are the theoretical predictions [Eqs. (6.9) and (6.7)] for our particular visibility conditions, considering the characterized transmission values of our neutral density filter.

Figure 6.5(a) shows such experimental dependency. It can be clearly seen that, effectively, the visibility of the singles is null for any value of transmissivity of the NDF. This is exactly what the theory

predicts. The insets show some examples of the singles measured while scanning the phase in a small region ($\sim 4\ \mu$m).

On the other hand, Fig. 6.5(b) depicts the experimental relationship of the visibility of the coincidence fringes with the transmissivity of the NDF, t. The expected nonlinear relationship is shown in Eq. (6.12). The coincidence window width is set to be $T_R = 5$ ns, and the total temporal window detection is $T_0 = 3$ s. The insets show some examples of the coincidence fringes while scanning the phase of the interferometer, for three different values of the transmissivity. The maximum visibility observed is $V = 55\%$.

6.5 Second-order correlation function between signal photons

The aim of this section is to calculate the second-order correlation function $g^{(2)}_{s_1,s_2}$ between signal photons, s_1 and s_2, generated in the two spatially separated down-converters. In [20], they calculated the second-order correlation function of signal photons s_1 and s_2 using the Schrödinger picture under certain approximations. This calculation can be made much simpler using the Heisenberg picture. Moreover our approach provides much more information since it does not make use of the same approximations used in [20]. For the sake of simplicity, we consider the single-mode approximation, that gives the main features of $g^{(2)}_{s_1,s_2}$.

The Bogoliubov transformations in the first nonlinear crystal are

$$\begin{aligned} \hat{a}_{s_1} &= U_{s_1}\,\hat{b}_s + V_{s_1}\,\hat{b}_i^\dagger, \\ \hat{a}_{i_1} &= U_{i_1}\,\hat{b}_i + V_{i_1}\,\hat{b}_s^\dagger, \end{aligned} \tag{6.14}$$

where the functions U_{s_1} and V_{s_1} fulfill $|U_{s_1}|^2 - |V_{s_1}|^2 = 1$. Similarly for U_{i_1} and V_{i_1}. The expressions for the functions U_{s_1,i_1} and V_{s_1,i_1} are the ones shown in Eqs. (2.23) and (2.24) with $\Omega \longrightarrow 0$. The

6.5 Second-order correlation function of signal photons

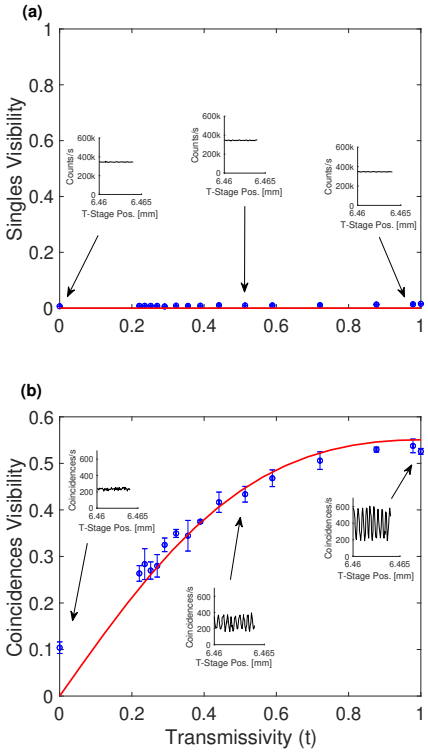

Figure 6.5: (a) Experimental relation between the singles visibility of the interference pattern and the transmissivity of the simulated sample t. (b) Experimental relation between the visibility of the coincidence fringes and the transmissivity of the simulated sample t. Blue dots correspond to the experimental measurements, while the red solid curve is the theoretical prediction [Eq. (6.12)] for our particular visibility conditions, considering the characterized transmission values of our neutral density filter.

transformation for the operator $\hat{a}_{i_1}$ accounting for losses is

$$\begin{aligned} \hat{a}_{i_1} &\Longrightarrow t\hat{a}_{i_1} + \hat{f} \\ &= tU_{i_1}\hat{b}_i + tV_{i_1}\hat{b}_s^\dagger + \hat{f} \end{aligned} \tag{6.15}$$

where $\hat{f}$ is an operator that fulfills the commutation relation $[\hat{f}, \hat{f}^\dagger] = 1 - |t|^2$. The linear polarization of idler i_1 is rotated an angle α. The annihilation operator associated to the vertical component of the idler i_1, that participates in the PDC process in the second nonlinear crystal can be written as

$$t\cos\alpha\, U_{i_1}\hat{b}_i + t\cos\alpha\, V_{i_1}\hat{b}_s^\dagger + \cos\alpha\,\hat{f} + \sin\alpha\,\hat{c}_i, \tag{6.16}$$

where $\hat{c}_i$ is the annihilation operator associated to the orthogonal polarization to the idler i_1 after rotation angle α. The Bogoliubov transformation in the second nonlinear crystal reads

$$\begin{aligned}
&\hat{a}_{s_2} = U_{s_2}\hat{c}_s + \\
&+V_{s_2}\Big[t\cos\alpha\, U_{i_1}\hat{b}_i + t\cos\alpha\, V_{i_1}\hat{b}_s^\dagger + \cos\alpha\,\hat{f} + \sin\alpha\,\hat{c}_i\Big]^\dagger = \\
&= U_{s_2}\hat{c}_s + t^*\cos\alpha\, U_{i_1}^*\hat{b}_i^\dagger + t^*\cos\alpha\, V_{i_1}^*\hat{b}_s + \\
&+\cos\alpha\,\hat{f}^\dagger + \sin\alpha\,\hat{c}_i^\dagger.
\end{aligned} \tag{6.17}$$

The number of signal photons s_1 generated is

$$N_{s_1} = \langle \hat{a}_{s_1}^\dagger \hat{a}_{s_1}\rangle = |V_{s_1}|^2. \tag{6.18}$$

The number of signal photons s_2 generated is

$$N_{s_2} = \langle \hat{a}_{s_2}^\dagger \hat{a}_{s_2}\rangle = |V_{s_2}|^2\Big[1 + |t|^2\,\cos^2\alpha\,|V_{i_1}|^2\Big]. \tag{6.19}$$

The normalized second-order correlation function $g^{(2)}_{s_1,s_2}$ between the signal photons generated in both nonlinear crystals is

$$g^{(2)}_{s_1,s_2} = \frac{\langle \hat{a}_{s_1}^\dagger \hat{a}_{s_2}^\dagger \hat{a}_{s_2}\hat{a}_{s_1}\rangle}{\langle \hat{a}_{s_1}^\dagger \hat{a}_{s_1}\rangle\langle \hat{a}_{s_2}^\dagger \hat{a}_{s_2}\rangle}. \tag{6.20}$$

We have

$$\begin{aligned}
&\langle \hat{a}_{s_1}^\dagger \hat{a}_{s_2}^\dagger \hat{a}_{s_2}\hat{a}_{s_1}\rangle = |V_{s_1}|^2|V_{s_2}|^2\big[1 + |t|^2\,\cos^2\alpha + \\
&+2|t|^2\cos^2\alpha\,|V_{i_1}|^2\big].
\end{aligned} \tag{6.21}$$

Substituting this expression, and Eqs. (6.18) and (6.19) into Eq. (6.20), we obtain

$$g^{(2)}_{s_1,s_2} = \frac{1+|t|^2\cos^2\alpha+2|t|^2\cos^2\alpha\,|V_{i_1}|^2}{1+|t|^2\,\cos^2\alpha\,\,|V_{i_1}|^2} = \\ = 1+|t|^2\,\cos^2\alpha\frac{1+|V_{i_1}|^2}{1+|t|^2\,\cos^2\alpha\,|V_{i_1}|^2}. \tag{6.22}$$

If the idler i_1 is blocked, then $t = 0$ and $g^{(2)}_{s_1,s_2} = 1$. This means that the emission of both nonlinear crystals is independent, they are uncorrelated. If the idler photon i_1 is rotated an angle of 90°, so there is no stimulated emission in the second nonlinear crystal, we obtain again $g^{(2)}_{s_1,s_2} = 1$, the signal photons s_1 and s_2 are uncorrelated.

For $\alpha = 0°$, in the high parametric gain ($|V_{i_1}|^2 \gg 1$), we have $g^{(2)}_{s_1,s_2} = 2$. This bunching effect can be attributed to the presence of an intense flux rate of idler photons i_1 coming from the first nonlinear crystal that generates stimulated emission of signal photons s_2 in the second nonlinear crystal. The value of 2 is independent of the values of t.

What is somehow surprisingly is that in the low parametric gain regime, where $|V| \ll 1$, and paired photons are assumed to be generated in only one of the nonlinear crystals, being the probability to generate them simultaneously in both nonlinear crystals negligible. We can write

$$g^{(2)}_{s_1,s_2} = 1+|t|^2\,\cos^2\alpha. \tag{6.23}$$

If the idler is not blocked ($t = 1$), the second-order correlation function is $g^{(2)}_{s_1,s_2} = 1$ if $\alpha = 90°$ (no stimulated emission), while it is $g^{(2)}_{s_1,s_2} = 2$ if $\alpha = 0°$ (there is stimulated emission). We cannot longer say that the emission of signal photons from the two nonlinear crystals is uncorrelated. This seems to suggest that stimulated emission plays a role in the induced coherence effect. This bunching effect can be attributed to the presence of the idler photon i_2 generated in the first nonlinear crystal that stimulates the generation of signal s_2 in the second nonlinear crystal.

CHAPTER

SEVEN

SPATIAL SPECTROSCOPY WITH A NONLINEAR INTERFEROMETER

Spectroscopy aims at unveiling characteristics of an object as its chemical composition by studying the interaction between electromagnetic radiation and matter as a function of the wavelength of the radiation. In the special case of Hyperspectral Imaging, tens and even hundreds of different wavelength are considered. Spatial spectroscopy designates any imaging or sensing scheme aimed at retrieving the shape of an object, its transverse spatial features, using spatial modes of light. Similarly to the case of Hyperspectral Imaging, we might consider many spatial modes.

In this chapter we put forward a scheme to do spatial spectroscopy with a nonlinear interferometer. In the first section we describe what are the spatial modes of light, highlighting some of the most widely used. This leads us to introduce the concept of orbital angular momentum (OAM) and how to generate experimentally light with OAM. We propose an scheme for doing spatial spectroscopy and we show the

main equations that demonstrate the validity of this novel approach. Finally, for the sake of example, we apply the technique proposed to the case of a simple cliff-like structure, a phase object, to illustrate that the spatial spectroscopy scheme would work effectively.

7.1 Spatial modes of light

Light beams are described by a set of variables that will determine its usefulness for different applications: its central wavelength, bandwidth, and state of polarization. Light beams can also have spatial shape, a degree of freedom that is being extensively explored for new applications in the last few decades [92, 93].

In general, Maxwell equations dictate that all the degrees of freedom that characterize a light beam are linked, especially in extreme cases, such as highly focused beams or with a large bandwidth. However, under the paraxial approximation, when the effective size of the beam (w_0) is much larger than the wavelength (λ_0), the spatial shape $f(x, y)$ of the beam can be considered separately from its polarization and frequency. Under these circumstances, one can decompose the spatial shape as

$$f(x, y) = \sum_n c_n U_n(x, y), \tag{7.1}$$

where $U_n(x, y)$ are light beams with a specific spatial shape and c_n are the complex coefficients that determine the mode decomposition. We refer to the set U_n as spatial modes of light.

There is a great freedom for selecting one particular basis of spatial modes, and the choice generally depends on what is more convenient in the specific problem that one wants to address. The Hermite-Gaussian (HG) modes are a common choice in cartesian coordinates. They are of special interest since they emerge naturally from a laser cavity. Two sets of spatial modes emerge in cylindrical coordinates: the Laguerre-Gaussian (LG) modes and the Bessel (BB) modes. These are good examples of ring-shaped beams which carry

orbital angular momentum (OAM) [94].

The angular momentum (AM) of a light beam contains two contributions: one associated to its polarization state (spin angular momentum) and the other associated to its spatial shape, especially the spatial distribution of the phase of the light beam (orbital angular momentum).

There are different ways to experimentally generate beams carrying OAM. One of the most popular makes use of spatial light modulators (SLMs) [95, 96]. These are computer-controlled pixelated liquid crystal devices whose operating principle is based on displaying an interference pattern that introduces the desired spatial phase distribution on the impinging beam. Its main advantage is that the encoded information in the phase pattern can be changed with frequencies up to 60 Hz. Other methods to generate beams with OAM are Digital Micromirror Devices (DMDs) and q-plates.

Figure 7.1(a) shows an example of a forked hologram produced by the superposition of a blazed grating and the spiraling phase aimed at generating a concrete Laguerre-Gaussian mode (Fig. 7.1(b)). This kind of interference pattern are the ones displayed, for instance, in the liquid-crystal display of an SLM. The use of fork holograms produces several diffracted orders, so experimentally one needs to select the desired one.

Spatial modes of light and beams with OAM have experienced a surge of interest in recent years and have found numerous applications. They have been used for phase estimation [97–100] and to characterize entanglement [101, 102]. Furthermore, new topological states of light have been demonstrated experimentally [103].

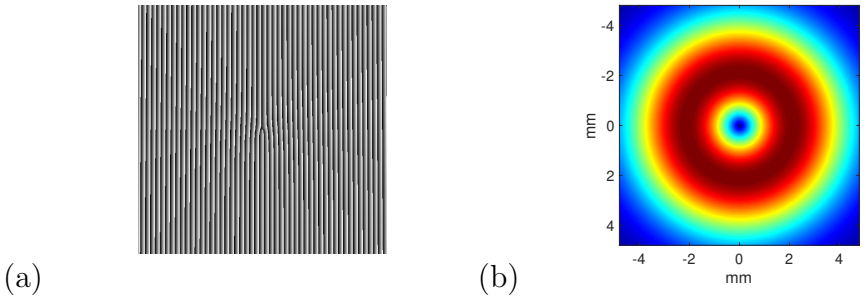

Figure 7.1: (a) Fork hologram encoded in an SLM to create a LG mode of light. (b) Example of a LG mode generated with the hologram shown in (a).

7.2 Spatial spectroscopy

In order to obtain transverse spatial information of an object, such as its shape or its phase gradient, all imaging schemes based on nonlinear interferometers need to scan the sample in the transverse plane (perpendicularly to the direction of propagation of the light beam that illuminates the sample). Here we put forward the possibility to obtain spatial information of a phase object, based on the proper selection and projection in concrete spatial modes of light at the detection stage.

Figure 7.2 illustrates a simplified sketch of the setup aimed at doing spatial spectroscopy with a nonlinear interferometer. The phase object located in the idler i_1 path changes the spatial mode decomposition of the idler photon i_1. The aim is to demonstrate that the visibility of the interference of signal photons can assess spatial properties of the object.

We analyze parametric down-conversion in the Schrödinger picture. Concerning the spatial shape degree of freedom of the pairs of signal-idler photons generated in a nonlinear crystal, its quantum

7.2 Spatial spectroscopy

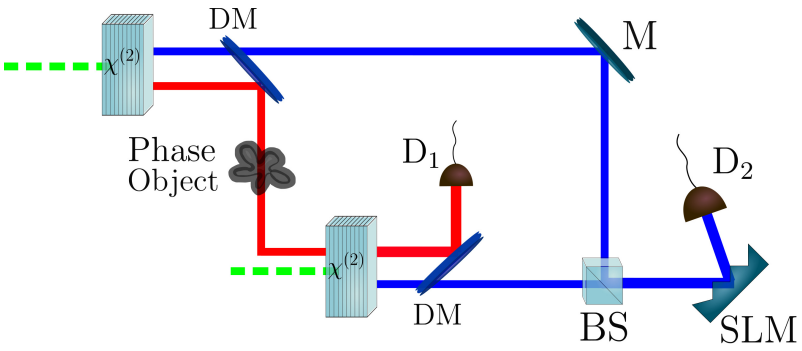

Figure 7.2: Simplified sketch of the spatial spectroscopy setup. The signal and idler beams are represented by the blue and red solid lines, respectively. *DM*: dichroic mirror; D_1: near infrared detector; D_2: visible detector; *BS*: beam splitter; *M*: mirror; *SLM*: spatial light modulator.

state can be written as [104]

$$|\Psi_{12}\rangle = \int d\mathbf{x}_1 d\mathbf{x}_2 \Psi(\mathbf{x}_1, \mathbf{x}_2) \hat{a_s}^\dagger(\mathbf{x}_1) \hat{a_i}^\dagger(\mathbf{x}_2) \, |vac\rangle \,, \tag{7.2}$$

where $\mathbf{x}_1 = (x_1, y_1)$ are transverse coordinates for the signal photon and $\mathbf{x}_2 = (x_2, y_2)$ are transverse coordinates for the idler photons. The function $\Psi(\mathbf{x}_1, \mathbf{x}_2)$ is the mode function that characterizes the quantum state of signal-idler photons. If $\Psi(\mathbf{x}_1, \mathbf{x}_2) = \Psi_s(\mathbf{x}_1) \times \Psi_i(\mathbf{x}_2)$, the quantum state is separable. In general, the quantum state can always be decomposed as the so-called Schmidt decomposition [102]

$$|\Psi\rangle = \sum_k \lambda_k \, |u_k\rangle \, |v_k\rangle \,, \tag{7.3}$$

where $\{|u_k\rangle \,, |v_k\rangle\}$ are basis in the Hilbert spaces of the signal and idler modes, respectively. The coefficients λ_k are the Schmidt coefficients, and if the state is normalized they fulfill $\sum_k \lambda_k^2 = 1$. The

quantum states $\{|u_k\rangle, |v_k\rangle\}$ can be writen as

$$|u_k\rangle = \int d\mathbf{x} f_k(\mathbf{x}) \hat{a_s}^\dagger(\mathbf{x}) |vac\rangle ,$$
$$|v_k\rangle = \int d\mathbf{x} g_k(\mathbf{x}) \hat{a_i}^\dagger(\mathbf{x}) |vac\rangle . \tag{7.4}$$

Let us consider that in the idler i_1 path there is a phase object that introduces a spatially-dependent phase change $\varphi(\mathbf{x})$ to the spatial shape of the input photons. The transformation of Schmidt modes that describes the interaction with the phase object is

$$|v_k\rangle \Longrightarrow |w_k\rangle , \tag{7.5}$$

where

$$|w_k\rangle = \int d\mathbf{x}\, g_k(\mathbf{x}) \exp\left[i\varphi(\mathbf{x})\right] \hat{a_i}^\dagger(\mathbf{x}) |vac\rangle . \tag{7.6}$$

Using this formalism, the quantum state $|\Psi_1\rangle$ before the last beam splitter shown in Fig. 7.2 can be written as

$$|\Psi_1\rangle = \frac{1}{\sqrt{2}} \sum_n \lambda_n \Big[|u_n\rangle_{s_1} |w_n\rangle_{i_2} + |u_n\rangle_{s_2} |v_n\rangle_{i_2} \Big]. \tag{7.7}$$

The beam splitter have reflection coefficient r and transmission coefficient t. At the two output ports of the BS, we have signal photons s_3 and s_4. The quantum state $|\Psi_{34}\rangle$ at the output ports of the beam splitter is

$$|\Psi_{34}\rangle = |\Psi_3\rangle + |\Psi_4\rangle = \frac{1}{\sqrt{2}} \sum_n \lambda_n \Big\{ |u_n\rangle_{s_3} \Big[r |w_n\rangle_{i_2} + t |v_n\rangle_{i_2} \Big] +$$
$$+ |u_n\rangle_{s_4} \Big[t |w_n\rangle_{i_2} + r |v_n\rangle_{i_2} \Big] \Big\}, \tag{7.8}$$

the sub-indexes $s_{1,2}$ stand for the signal photons generated in the first and the second nonlinear crystal, respectively. i_2 is the idler beam, constituted by the indistinguishable idler photons generated in both nonlinear crystals.

7.2 Spatial spectroscopy

At the detection state, we project signal photon s_3 onto the mode $|u_k\rangle_{s_3}$ and the idler photon i_2 onto the mode $|v_l\rangle_{i_2}$. The probability to detect a coincidence as a function of the phase difference θ is

$$\begin{aligned} P_{lk} &= \frac{\lambda_k^2}{2}\Big|r\langle v_l|w_k\rangle + t\,\exp(i\theta)\delta_{kl}\Big|^2 = \\ &= \frac{\lambda_k^2}{2}\Big[|r|^2\langle w_k|v_l\rangle\langle v_l|w_k\rangle + |t|^2\delta_{kl} + \\ &+rt^*\exp(-i\theta)\langle v_l|w_k\rangle\,\delta_{kl} + r^*t\,\exp(i\theta)\langle w_k|v_l\rangle\,\delta_{kl}\Big]. \end{aligned} \tag{7.9}$$

Finally we sum over all l modes to obtain the probability to detect a signal photon in mode k. We obtain

$$\begin{aligned} P_k &= \sum_l P_{kl} = \frac{\lambda_k^2}{2}\Big[|r|^2 + |t|^2 + \\ &+rt^*\exp(-i\theta)\langle v_k|w_k\rangle + r^*t\exp(i\theta)\langle w_k|v_k\rangle\Big] = \\ &= \frac{\lambda_k^2}{2}\Big[1 + |\langle w_k|v_k\rangle|\sin\varphi\Big]. \end{aligned} \tag{7.10}$$

We have made use of $r = i/\sqrt{2}$, $t = 1/\sqrt{2}$ and $\sum_l |v_l\rangle\langle v_l| = I$. The maximum P_k^{max} and minimum P_k^{min} values of P_k are

$$P_k^{max} = \frac{\lambda_k^2}{2}\Big[1 + |\langle w_k|v_k\rangle|\Big], \tag{7.11}$$

$$P_k^{min} = \frac{\lambda_k^2}{2}\Big[1 - |\langle w_k|v_k\rangle|\Big]. \tag{7.12}$$

The visibility V is the interference fringes that appear as function of θ is

$$V = \frac{P_k^{max} - P_k^{min}}{P_k^{max} + P_k^{min}} = |\langle w_k|v_k\rangle|. \tag{7.13}$$

The visibility of the interference pattern of signal photons depends on how the object changes the spatial properties of the idler photon i_1, introducing a spatially dependent phase $\varphi(\mathbf{x})$. The shape of the object can be reconstructed by projecting the signal photons in appropriately selected spatial modes without the need to scan spatially the object.

Example: estimation of the height of the step of a cliff-like structure

For the sake of example, let us consider a simple object located in the idler i_1 path. It is a cliff-like structure [105, 106] and the parameter to be estimated is the height d of the step and its position x_0 (see Fig. 7.3).

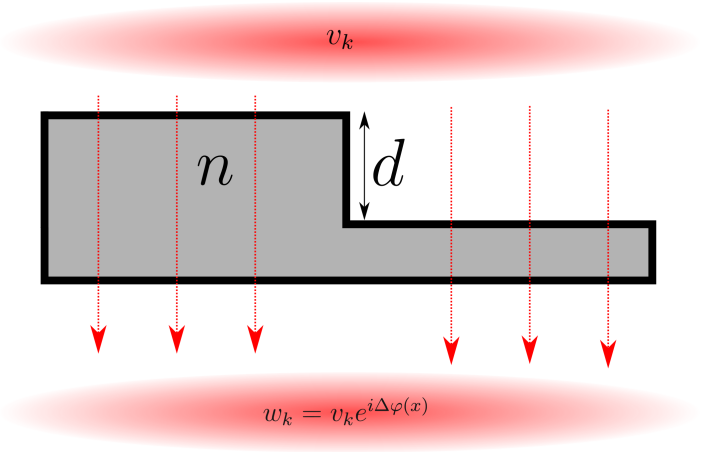

Figure 7.3: Sketch of a phase object. A cliff-like structure with step height d. The beam that illuminates the sample is shown in red.

We assume that the Schmidt decomposition is of the form

$$|\Psi\rangle = \lambda_0 |u_0\rangle |v_0\rangle + \sum_{k\neq 0} \lambda_k |u_k\rangle |v_k\rangle , \tag{7.14}$$

where the spatial shape of $|u_0\rangle$ and $|v_0\rangle$ are described by Gaussian modes of the form

$$g_0(\mathbf{x}) = \frac{1}{(\pi w_0^2)^{1/2}} \exp\Big[-\frac{|\mathbf{x}|^2}{2w_0^2}\Big], \tag{7.15}$$

where $\mathbf{x}$ is the spatial coordinate and w_0 is the beam width. If the transmissivity of the object is high ($|t| \sim 1$ and $|r| \sim 0$), we can

7.2 Spatial spectroscopy

neglect reflections at the facets of the object. The spatially-varying phase $\varphi(x)$ introduced by the object is

$$\varphi(x) = \frac{\Delta}{2}\Big[1 + \tanh\alpha(x - x_0)\Big], \tag{7.16}$$

where $\Delta = k_0 d(n-1)$, k_0 is the central wavenumber, d the height of the step, n the refractive index of the material, α is a measure of the steepness of the step that we assume here to be large, and x_0 is the position of the step.

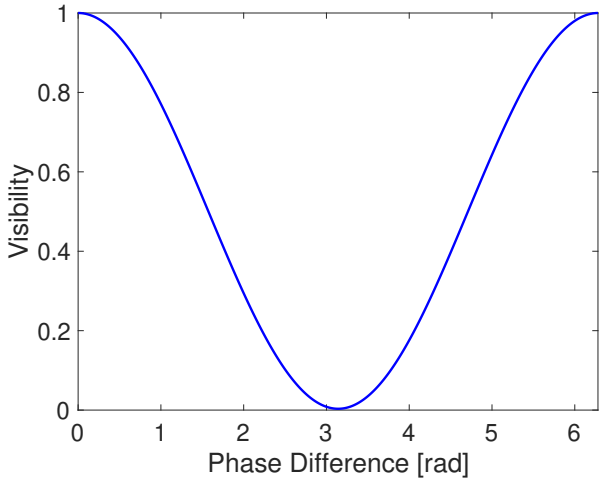

Figure 7.4: Visibility of the interference fringes as function of the phase difference $\Delta = k_0 d(n-1)$. The step is located at $x_0 = 0$ and the beam width of the mode is $w_0 = 100$ μm.

The input gaussian mode v_k is transformed by the object to a new spatial mode w_k

$$g_0(\mathbf{x}) = \frac{1}{(\pi w_0^2)^{1/2}} \exp\Big[-\frac{|\mathbf{x}|^2}{2w_0^2}\Big] \exp[i\varphi(x)]. \tag{7.17}$$

The overlap between spatial modes before and after the object is

$$\langle w_k | v_k \rangle = \frac{1}{(\pi w_0^2)^{1/2}} \int dx \exp\Big[-\frac{x^2}{w_0^2} - i\varphi(x)\Big]. \tag{7.18}$$

The height d of the step can be determined from the dependence of the visibility with the phase difference Δ. If we consider a sample with $n = 1.5$, the phase difference is $\Delta = \pi(d/\lambda)$. Figure 7.4 shows the visibility of the interference fringes induced by the presence of the phase object. When $d = \lambda$, $\Delta = \pi$ and we observe no fringes (zero visibility).

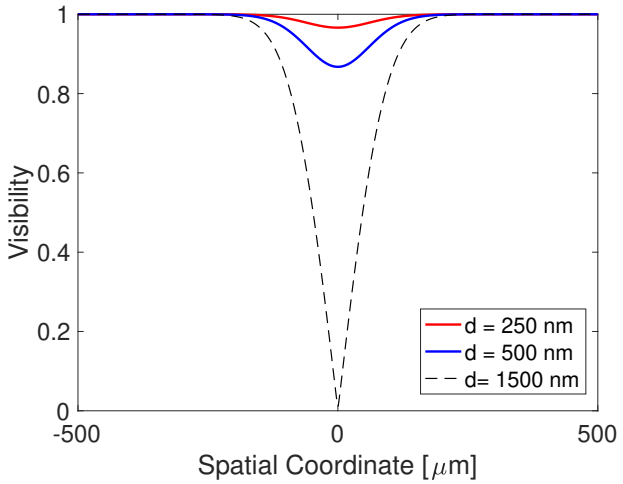

Figure 7.5: Visibility of the interference fringes for a three different cliff-like structures with heights: $d = 250$ nm (red solid line); $d = 500$ nm (blue solid line) and $d = \lambda = 1500$ nm (dashed line). The visibility is zero for $d = \lambda$.

Figure 7.5 shows the visibility introduced by the presence of three different cliff-like structures with heights $d = 250$ nm, $d = 500$ nm and $d = \lambda = 1500$ nm, as a function of x_0. If we have a priori information about the value of d, Fig. 7.5 allows us to determine the position of the step x_0.

CHAPTER

EIGHT

CONCLUSIONS

In this thesis we have introduced and demonstrated two novel optical coherence tomography (OCT) schemes based on the use of nonlinear interferometers. One scheme works in the low parametric gain regime of parametric amplifiers and is based on the concept of induced coherence [56]. The other scheme is an SU(1,1) interferometer that works in the high parametric gain regime [51]. We have characterized, experimentally and theoretically [61, 62], how these systems work and its main advantages and limitations. We should mention that our work is the first demonstration of OCT based on nonlinear interferometers.

We have derived and demonstrated a complementarity relationship between quantum distinguishability and first-order coherence that explains the trade-off between both quantities in a general case, including the extreme cases of low and high parametric gain regime[1]. This is one rare case of complementarity relationship that does not apply only in the single-photon regime, as it is the case of most of the other relationships of this type.

[1]We are currently writing three scientific papers that cover some of the topics discussed here and not yet published.

Conclusions

We have investigated the role of fundamental concepts such as stimulated emission and quantum distinguishability in the explanation of why and how induced coherence takes place. There is an ongoing *dispute* on this topic [19,20], that has not been resolved yet, about what is the *true* explanation of the concept of induced coherence. We have derived results that show that even in the low parametric gain regime the signal photons generated in spatially separated nonlinear crystals are not uncorrelated, even though one generally assumes that in this regime stimulated emission does not play any role to generate induced coherence.

We have introduced a scheme based on a nonlinear interferometer to obtain transverse spatial information of a phase object (spatial spectroscopy). The basic ingredient of this new scheme is the use of projection onto selected spatial modes in the detection stage, avoiding in this way the need to use spatial scans of the sample. Most schemes based on a nonlinear interferometer perform spatial scans of the sample with a focused beam to retrieve spatial information of the object under investigation.

APPENDIX **A**

ORIGIN OF THE TERM SU(1,1) INTERFEROMETER

Classical interferometers such as Michelson and Mach-Zehnder configurations, that make use of beam splitters (BS), are also called SU(2) interferometers. The presence of beam splitters, whose transformation matrices belong to the special unitary SU(2) group, give them their name. In Yurke-type nonlinear interferometers [8] the beam splitters are substituted by parametric down-conversion sources, whose transformation matrices belong to the special unitary SU(1,1) group. Hence its name. Let us analyze both cases separately.

The beam splitter

Signals with electric fields E_1 and E_2 enter the input ports 1 and 2 of the BS, respectively (see Fig. A.1). The output electric fields E_3 and E_4 can be written as function of the input fields as

$$E_3 = rE_1 + tE_2, \tag{A.1}$$

$$E_4 = tE_1 + rE_2, \tag{A.2}$$

where r and t are the reflection and transmission coefficients of the beam splitter. In a symmetric lossless beam splitter, the reflection

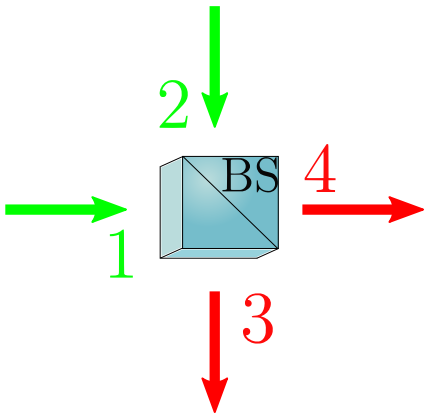

Figure A.1: Schematic illustration of a beam splitter. Input ports (green): 1 & 2. Output ports (red): 3 & 4.

and transmission coefficients fulfil the relations $|r|^2 + |t|^2 = 1$ and $rt^* + r^*t = 0$.

Equations (A.1) and (A.2) can be written in matrix form as

$$\mathbf{E_{out}} = \begin{pmatrix} E_3 \\ E_4 \end{pmatrix} = \begin{pmatrix} r & t \\ t & r \end{pmatrix} \begin{pmatrix} E_1 \\ E_2 \end{pmatrix} = \mathcal{T}\mathbf{E_{in}}, \tag{A.3}$$

where $\mathcal{T}$ is the transformation matrix. $\mathcal{T}$ is unitary, i.e. $\mathcal{T}^{-1} = \mathcal{T}^\dagger$, so

$$\begin{pmatrix} r & t \\ t & r \end{pmatrix} \begin{pmatrix} r^* & t^* \\ t^* & r^* \end{pmatrix} = \begin{pmatrix} 1 & 0 \\ 0 & 1 \end{pmatrix}. \tag{A.4}$$

The determinant is 1. These matrices are said to belong to the special unitary SU(2) Lie group, since they are 2×2 matrices, they are unitary and they have unit determinant.

The reflection and transmission coefficients are complex numbers, i.e. $r = |r|\exp(i\alpha)$ and $t = |t|\exp(i\beta)$. As example we can write $|r| = \cos\phi$, $|t| = \sin\phi$, $\alpha = 0$ and $\beta = \pi/2$. Hence the matrix $\mathcal{T}$ becomes

$$\mathcal{T} = \begin{pmatrix} \cos(\phi) & i\sin(\phi) \\ i\sin(\phi) & \cos(\phi) \end{pmatrix}. \tag{A.5}$$

Appendix A

A parametric down-conversion source

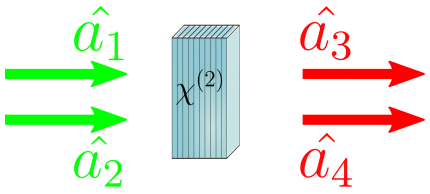

Figure A.2: Schematic illustration of a PDC source. Input operators (green): $\hat{a}_1$ and $\hat{a}_2$. Output operators (red): $\hat{a}_3$ and $\hat{a}_4$.

The input-output operators relations (so-called Bogoliubov transformations) can be written in its simplest form as:

$$\hat{a}_3 = U\hat{a}_1 + V\hat{a}_2^\dagger, \tag{A.6}$$

$$\hat{a}_4 = U\hat{a}_2 + V\hat{a}_1^\dagger, \tag{A.7}$$

where U and V are complex functions. Equations (A.6) and (A.7) can be written in matrix form as

$$\begin{pmatrix} \hat{a}_3 \\ \hat{a}_4^\dagger \end{pmatrix} = \mathcal{T} \begin{pmatrix} \hat{a}_1 \\ \hat{a}_2^\dagger \end{pmatrix} = \begin{pmatrix} U & V \\ V^* & U^* \end{pmatrix} \begin{pmatrix} \hat{a}_1 \\ \hat{a}_2^\dagger \end{pmatrix}. \tag{A.8}$$

Definition: A matrix $\mathcal{U}$ is said to belong to the special unitary SU(m,n) group if it leaves invariant the Hermitian form $\mathcal{U}A\mathcal{U}^\dagger = A$, where

$$A_{ij} = a_i\delta_{ij} \begin{cases} a_i = 1 & 1 \le i \le m \\ a_i = -1 & m+1 \le i \le m+n \end{cases} \tag{A.9}$$

The SU(1,1) group consists of 2×2 complex matrices $\mathcal{U}$ that satisfy the relation $\mathcal{U}A\mathcal{U}^\dagger = A$, with

$$A = \begin{pmatrix} 1 & 0 \\ 0 & -1 \end{pmatrix}. \tag{A.10}$$

It can be easily checked that this is only satisfied by matrices $\mathcal{U}$ of the form

$$\mathcal{U} = \begin{pmatrix} \alpha & \beta \\ \beta^* & \alpha^* \end{pmatrix}. \tag{A.11}$$

with $|\alpha|^2 - |\beta|^2 = 1$. The matrix $\mathcal{T}$ presented in Eq. (A.8) that characterizes a PDC source is equivalent to the matrix $\mathcal{U}$ [Eq. (A.11)] with $\alpha = U$ and $\beta = V$. $\mathcal{T}$ also fulfills the relation

$$\begin{aligned} &\mathcal{T} A \mathcal{T}^\dagger = \\ &= \begin{pmatrix} U & V \\ V^* & U^* \end{pmatrix} \begin{pmatrix} 1 & 0 \\ 0 & -1 \end{pmatrix} \begin{pmatrix} U^* & V \\ V^* & U \end{pmatrix} = \begin{pmatrix} 1 & 0 \\ 0 & -1 \end{pmatrix} = A. \end{aligned} \tag{A.12}$$

The matrix $\mathcal{T}$ that characterizes the input-output relationship between operators of a PDC source belongs to the so-called *SU(1,1) group*, giving name to this *Yurke-type* nonlinear interferometer.

Recently it has been shown the possibility of mixing both classes of interferometers [107, 108].

APPENDIX **B**

MATERIAL PROPERTIES OF LITHIUM NIOBATE

This appendix compiles the fundamental properties of lithium niobate, the material from which the nonlinear crystals used in this thesis are composed. Specifically, we have used periodically poled lithium niobate crystals (PPLN) from Covesion, with lengths of $L = 1$ mm and $L = 20$ mm.

- *Sellmeier equation:*

$$\begin{aligned} n^2 &= 5.756 + 2.86 \times 10^{-6} f + \\ &+ \frac{0.0983 + 4.7 \times 10^{-8} f}{\lambda^2 - (0.2020 + 6.113 \times 10^{-8} f)^2} + \\ &+ \frac{189.32 + 1.516 \times 10^{-4} f}{\lambda^2 - 12.52^2} - 1.32 \times 10^{-2} \lambda^2, \end{aligned} \tag{B.1}$$

  where $f = (T - 24.5)(T + 570.82)$, with T in $°C$. Expression extracted from[1].

[1] https://www.covesion.com/en/resource/material-properties-of-lithium-niobate/

- *Second-order nonlinear susceptibility:* $\chi^{(2)} = 14$ pm/V.
- *Refractive index:* For $T = 123$ °C.

PPLN refractive index	
Wavelength [nm]	n
532	2.2569
810	2.1975
1550	2.1608

- *Inverse Group Velocity:* For $T = 123$ °C.

PPLN Inverse Group Velocity	
Wavelength [nm]	D [ns/m]
810	7.3250
1550	7.2027

APPENDIX C

QUANTUM ANALYSIS OF ATTENUATION

The action of an attenuator can be modeled as a beam splitter with transmission t and reflection coefficient r. The input ports are labeled as 1 and 2, with associated operators $\hat{a}_1$ and $\hat{a}_2$. The output ports are labeled as 3 and 4, with operators $\hat{a}_3$ and $\hat{a}_4$. Light reflected through output port 4 is considered *lost*. The relationships between input and output operators are

$$\hat{a}_3 = t\hat{a}_1 + r\hat{a}_2, \tag{C.1}$$

$$\hat{a}_4 = r\hat{a}_1 + t\hat{a}_2. \tag{C.2}$$

All the input and output operators must fulfill the usual commutation relations

$$[\hat{a}_1, \hat{a}_1^\dagger] = [\hat{a}_2, \hat{a}_2^\dagger] = [\hat{a}_3, \hat{a}_3^\dagger] = [\hat{a}_4, \hat{a}_4^\dagger] = 1, \tag{C.3}$$

$$[\hat{a}_1, \hat{a}_1] = [\hat{a}_2, \hat{a}_2] = [\hat{a}_3, \hat{a}_3] = [\hat{a}_4, \hat{a}_4] = 1, \tag{C.4}$$

$$[\hat{a}_1, \hat{a}_2] = [\hat{a}_3, \hat{a}_4] = 0. \tag{C.5}$$

Notice that this is indeed happening. For instance, we have

$$\begin{aligned}[\hat{a}_3, \hat{a}_3^\dagger] &= [t\hat{a}_1 + r\hat{a}_2, t^*\hat{a}_1^\dagger + r^*\hat{a}_2^\dagger] \\ &= |t|^2[\hat{a}_1, \hat{a}_1^\dagger] + |r|^2[\hat{a}_2, \hat{a}_2^\dagger] = |r|^2 + |t|^2 = 1.\end{aligned} \tag{C.6}$$

We can write that the operator associated to a photon that propagates through a lossy medium transforms as [49, 50]

$$\hat{a}_1 \longrightarrow t\hat{a}_1 + \hat{f}, \tag{C.7}$$

where the operator $\hat{f}$ is $\hat{f} = r\hat{a}_2$. The operator $\hat{f}$ fulfils the commutation relation

$$[\hat{f}, \hat{f}^\dagger] = [r\hat{a}_2, r^*\hat{a}_2^\dagger] = |r|^2\,[\hat{a}_2, \hat{a}_2^\dagger] = |r|^2 = 1 - |t|^2. \tag{C.8}$$

APPENDIX **D**

RELATIONSHIP BETWEEN FIRST-ORDER CORRELATION AND INTERFERENCE VISIBILITY

Consider an optical signal labeled 3, with associated quantum operator $\hat{a}_3$, that is the superposition of two signals with associated operators $\hat{a}_1$ and $\hat{a}_2$:

$$\hat{a}_3 = \hat{a}_1 \exp(i\varphi_1) + \hat{a}_2 \exp(i\varphi_2), \tag{D.1}$$

$\varphi_{1,2}$ are phases acquired by signals 1 and 2 during propagation that can change. The number of photons of signal 3 is:

$$\begin{aligned}
&N_3 = \langle \hat{a}_3^\dagger \hat{a}_3 \rangle = \\
&= \langle \left[\hat{a}_1^\dagger \exp(-i\varphi_1) + \hat{a}_2^\dagger \exp(-i\varphi_2)\right] \left[\hat{a}_1 \exp(i\varphi_1) + \hat{a}_2 \exp(i\varphi_2)\right] = \\
&= \langle \hat{a}_1^\dagger \hat{a}_1 \rangle + \langle \hat{a}_2^\dagger \hat{a}_2 \rangle + \langle \hat{a}_1^\dagger \hat{a}_2 \rangle \exp(-i\varphi_1 + i\varphi_2) \\
&+ \langle \hat{a}_2^\dagger \hat{a}_1 \rangle \exp(i\varphi_1 - i\varphi_2) = \\
&= N_1 + N_2 + 2N_1^{1/2} N_2^{1/2} \left| g_{12}^{(2)} \right| \cos(\varphi_2 - \varphi_1 + \varphi_g),
\end{aligned} \tag{D.2}$$

where $g_{12}^{(1)} = |g_{12}^{(1)}| \exp(i\varphi_g) = \langle \hat{a}_1^\dagger \hat{a}_2 \rangle / (N_1^{1/2} N_2^{1/2})$ is the normalized first-order correlation function between signals 1 and 2.

As a function of the phase difference $\Delta\varphi = \varphi_2 - \varphi_1$ the value of N_3 oscillate between the maximum

$$N_3^{max} = N_1 + N_2 + 2N_1^{1/2} N_2^{1/2} |g_{12}^{(2)}|, \tag{D.3}$$

and the minimum

$$N_3^{min} = N_1 + N_2 - 2N_1^{1/2} N_2^{1/2} |g_{12}^{(2)}|. \tag{D.4}$$

The visibility of the interference fringes is

$$V = \frac{N_3^{max} - N_3^{min}}{N_3^{max} + N_3^{min}} = \frac{2N_1^{1/2} N_2^{1/2}}{N_1 + N_2} |g_{12}^{(2)}|. \tag{D.5}$$

The signals 1 and 3 can bear different number of photons (energy). We define the distinguishability D as

$$D = \Big| \frac{\big|N_1 - N_2\big|}{N_1 + N_2} \Big|. \tag{D.6}$$

Taking into account that

$$1 - D^2 = \frac{2N_1 N_2}{(N_1 + N_2)^2}, \tag{D.7}$$

we can write

$$V = \sqrt{1 - D^2}\, |g_{12}^{(2)}|. \tag{D.8}$$

If $N_1 = N_2$, $D = 0$ and $V = |g_{12}^{(2)}|$. The value of the visibility of the interference fringes is the value of the first-order correlation function. However, when $N_1 \neq N_2$, the value of the first-order correlation function can be derived from the measurement of the visibility with the help of Eq. (D.8).

APPENDIX **E**

CALCULATION OF THE FIRST-ORDER CORRELATION FUNCTION IN A NONLINEAR INTERFEROMETER BASED ON INDUCED COHERENCE

In this Appendix we calculate the value of the normalized first-order correlation function $g^{(1)}_{s_1,s_2}$ between signal photons s_1 and s_2 that are generated in different nonlinear crystals. The experimental scheme is depicted in Fig. 3.7. Figure E.1 shows schematically the annihilation operators at different positions inside the experimental setup, as well as the main distances travelled by the photons.

We consider a pump laser that generates coherent light with a spectrum described by the function $F(\Omega_p)$. The frequency of the pump is $\omega_p = \omega_p^0 + \Omega_p$, with ω_p^0 being the central frequency and Ω_p the frequency deviation from the central frequency. A beam splitter

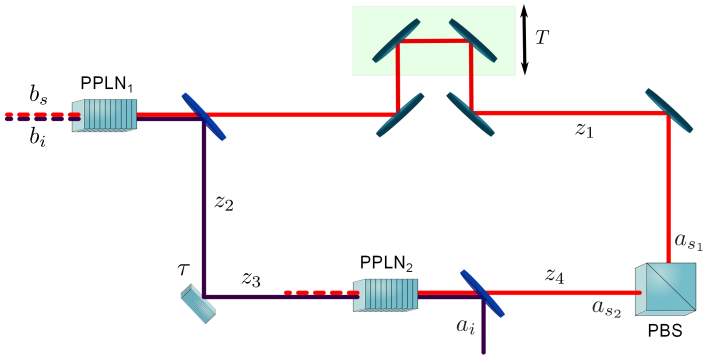

Figure E.1: Simple sketch of the experimental set-up that shows the name of the operators at different locations and main distances considered in the calculation.

divides the pump beam into two coherent sub-beams that pump the two nonlinear crystals. The two sub-beams travel distances z_{p_1} and z_{p_2} before reaching PPLN$_1$ and PPLN$_2$, respectively.

The two identical crystals have nonlinear susceptibility $\chi^{(2)}$ and length L. The nonlinear interaction generates signal and idler photons s_1 and i_1 in PPLN$_1$, and s_2 and i_2 in PPLN$_2$. The frequency of the signal and idler photons reads $\omega_s = \omega_s^0 + \Omega_s$ and $\omega_i = \omega_i^0 + \Omega_i$, where $\omega_{s,i}^0$ are central frequencies and $\Omega_{s,i}$ are frequency deviations from the corresponding central frequencies. The conditions $\omega_p^0 = \omega_s^0 + \omega_i^0$ and $\Omega_p = \Omega_s + \Omega_i$ are fulfilled.

The quantum operators $\hat{a}_{s_1,s_2}(\Omega_s)$ and $\hat{a}_{i_1,i_2}(\Omega_i)$ correspond to signal and idler modes at the output face of the corresponding nonlinear crystals. $\hat{b}_{s_1,s_2}(\Omega_s)$ and $\hat{b}_{i_1}(\Omega_i)$ designate the corresponding operators at the input face. In the low parametric gain regime, the Bogoliubov transformations that relate the input-output operators for PPLN$_1$ are [36, 44]:

$$\hat{a}_{s_1}(\Omega_s) = U_s(\Omega_s)\hat{b}_{s_1}(\Omega_s) + \int \mathrm{d}\Omega_i V_{s_1}(\Omega_s, \Omega_i)\hat{b}_{i_1}^\dagger(\Omega_i), \qquad \text{(E.1)}$$

$$\hat{a}_{i_1}(\Omega_i) = U_i(\Omega_i)\hat{b}_{i_1}(\Omega_i) + \int \mathrm{d}\Omega_s V_{i_1}(\Omega_s, \Omega_i)\hat{b}_{s_1}^\dagger(\Omega_s), \qquad \text{(E.2)}$$

Appendix E

where $U_s(\Omega_s) = \exp[ik_s(\Omega_s)L]$, $U_i(\Omega_i) = \exp[ik_i(\Omega_i)L]$ and

$$V_{s_1}(\Omega_s, \Omega_i) = i(\sigma L)F_{p_1}(\Omega_s + \Omega_i)\text{sinc}\left[\frac{\Delta kL}{2}\right] \times$$
$$\times \exp\left[i\frac{k_s(\Omega_s) - k_i(\Omega_i)}{2}L\right], \tag{E.3}$$
$$V_{i_1}(\Omega_s, \Omega_i) = i(\sigma L)F_{p_1}(\Omega_s + \Omega_i)\text{sinc}\left[\frac{\Delta kL}{2}\right] \times$$
$$\times \exp\left[i\frac{k_i(\Omega_i) - k_s(\Omega_s)}{2}L\right]. \tag{E.4}$$

The nonlinear coefficient σ is [36, 40, 44]

$$\sigma = \left[\frac{\hbar\omega_p^0\omega_s^0\omega_i^0[\chi^{(2)}]^2 N_0}{16\pi\epsilon_0 c^3 n_p n_s n_i A}\right]^{1/2}, \tag{E.5}$$

where N_0 is the number of photons per pulse of the pump beam, A is the effective area of interaction in the nonlinear crystal and $n_{p,s,i}$ are the refractive indexes at the central frequencies of all waves involved. The wave-vector phase mismatch is $\Delta k = k_p(\Omega_s+\Omega_i)-k_s(\Omega_s)-k_i(\Omega_i)$. If we expand in Taylor series to first order the wave-vectors as $k_i(\Omega) = k_i^0+N_i\Omega$ ($N_{p,s,i}$ are inverse group velocities) and assume perfect phase matching at the central frequencies ($k_p^0 = k_s^0 + k_i^0$), we obtain $\Delta k = D_+\Omega_p + D\Omega_-/2$, where $\Omega_- = \Omega_s - \Omega_i$, $D_+ = N_p - (N_s + N_i)/2$ and $D = N_i - N_s$.

The idler mode $\hat{a}_{i_1}$ traverses a distance z_2 before encountering a lossy sample characterized by reflectivity $r(\Omega_i)$. The quantum operator transformation that describes this process is [37, 49]

$$\hat{a}_{i_1}(\Omega_i) \longrightarrow r(\Omega_i)\hat{a}_{i_1}(\Omega_i)\exp[ik_i(\Omega_i)z_2] + \hat{f}(\Omega_i), \tag{E.6}$$

where the operator $\hat{f}$ fulfills the commutation relationship $[\hat{f}(\Omega), \hat{f}^\dagger(\Omega')] = (1 - |r(\Omega)|^2)\delta(\Omega - \Omega')$.

The idler beam is injected into PPLN_2 so that the operator $\hat{a}_{s_2}$ that describes signal beam s_2 at the output face of PPLN_2 is

$$\hat{a}_{s_2}(\Omega_s) = U_s(\Omega_s)\hat{b}_{s_2}(\Omega_s) + \int \mathrm{d}\Omega_i V_{s_2}(\Omega_s,\Omega_i)\hat{f}^\dagger(\Omega_i) \qquad \text{(E.7)}$$
$$+ \int \mathrm{d}\Omega_i r^*(\Omega_i) V_{s_2}(\Omega_s,\Omega_i) U_i^*(\Omega_i) \exp\left[-ik_i(\Omega_i)z_2\right] \hat{b}_i^\dagger(\Omega_i),$$

where only terms up to first order in σL have been considered and the only terms that give a non-zero contribution in the calculation of the first-order correlation function. The expression of the function V_{s_2} is analogous to the expression of V_{s_1} in Eq. (E.3) with $F_{p_2} = F_p(\Omega_p)\exp\left[ik_p(\Omega_p)z_{p_2}\right]$.

Signal photon s_1 traverses a distance z_1 before detection, and signal photon s_2 traverses a distance z_3. The number of down-converted signal photons generated per pulse, $N_{s_1} = \int \mathrm{d}\Omega\, \hat{a}_{s_1}^\dagger(\Omega)\hat{a}_{s_1}(\Omega)$ and $N_{s_2} = \int \mathrm{d}\Omega\, \hat{a}_{s_2}^\dagger(\Omega)\hat{a}_{s_2}(\Omega)$ are

$$N_{s_1} = N_{s_2} = 2\pi\frac{\sigma^2 L}{D}. \qquad \text{(E.8)}$$

It depends on the total number of pump photons per pulse, however it is independent of the shape of the pulse. This fact and that $N_{s_1} = N_{s_2}$ are characteristics of the low parametric gain regime.

We are interested in the normalized first-order correlation function $g^{(1)}_{s_1,s_2}$ between signal beams s_1 and s_2 that gives the visibility of the interference pattern detected after combining both signals in a beam splitter, i.e.,

$$g^{(1)}_{s_1,s_2} = \frac{1}{N_{s_1}^{1/2} N_{s_2}^{1/2}} \int \mathrm{d}\Omega\, \hat{a}_{s_1}^\dagger(\Omega)\hat{a}_{s_2}(\Omega). \qquad \text{(E.9)}$$

Let us first assume that there are no losses in the idler path ($r(\Omega_i) = 1$). Using Eqs. (E.1), (E.7) and (E.8) into Eq. (E.9) and taking into account the distances z_1 and z_3 that signal beams s_1 and s_2

Appendix E

propagate before combination in the beam splitter, the first-order correlation function can be written as

$$\left|g^{(1)}_{s_1,s_2}(T_1,T_2)\right| = \mathrm{tri}\left(\frac{T_1}{DL}\right) \times \exp\left[-\frac{1}{16T_0^2}\left[\left(1-\frac{2D_+}{D}\right)T_1+2T_2\right]^2\right], \tag{E.10}$$

where $\mathrm{tri}(\xi/2) = 1/\pi \int \mathrm{sinc}^2(x)\exp(i\xi x)\mathrm{d}x$ is the triangular function and

$$T_1 = \frac{z_3 - z_1 + z_2}{c} + N_i L, \tag{E.11}$$

$$T_2 = \frac{z_{p_2} - z_{p_1} - z_2}{c} - N_i L. \tag{E.12}$$

We assume that the condition $z_{p2} = z_{p1} + cN_iL + z_2$ if fulfilled, so that $T_2 = 0$. In order to optimize pulsed parametric amplification in $PPLN_2$ one needs to synchronize the time of arrival of pump and idler pulses to the nonlinear crystal [73].

APPENDIX **F**

ESTIMATION OF THE NUMBER OF PHOTONS PER MODE GENERATED IN A PARAMETRIC DOWN-CONVERSION PROCESS

The number of photons per mode generated in a parametric down-conversion process can be estimated by measuring the second-order correlation function $g^{(2)}$ [27] of the down-converted photons. For high signal-idler output flux, $g^{(2)}$ can be measured as a function of the PDC flux rate I as

$$g^{(2)} = \frac{\langle I^2 \rangle}{\langle I \rangle^2} = \frac{N \sum_{i=1}^{N} I_i^2}{\left(\sum_{i=1}^{N} I_i \right)^2}, \tag{F.1}$$

where N is the number of modes. For the number of idler photons generated in the experiment,

$$g^{(2)}_{idler} = \frac{\langle I^2_{idler}\rangle}{\langle I_{idler}\rangle^2} = 1.0006 \pm 0.0075, \tag{F.2}$$

where the error has been derived from the variance of the measured intensity σ_I^2 as

$$\sigma_g^2 = \sum_{i=1}^{N} \Big[\frac{\partial g^{(2)}}{\partial I_i}\Big]^2 \sigma_I^2 = \frac{4\sigma_I^2}{\langle I\rangle^2}\big(1 - g^{(2)}\big)^2. \tag{F.3}$$

The total number of modes (both spatial and temporal) $M = m_s m_t$ [75] is

$$M = \frac{g^{(2)}_s(0) - 1}{g^{(2)}_{meas}(0) - 1}, \tag{F.4}$$

where $g^{(2)}_s(0)$ is the normalised second-order correlation function for single mode PDC and $g^{(2)}_{meas}(0)$ is the measured second-order correlation function. By substituting the value of the second-order correlation function for single-mode PDC, $g^{(2)}_s(0) = 2$, the number of modes M in our experiment is estimated to be

$$M = \frac{1}{g^{(2)}_{idler} - 1} = 1774 \pm 178. \tag{F.5}$$

The total number of idler photons N_i generated in our experiment, taking into account a parametric gain value of $G = 1.7$, is

$$N_i = M \sinh^2(G) = M \sinh^2(1.7) \approx 13000. \tag{F.6}$$

The idler energy per pump pulse E_i and the mean power P_i of the idler photons can be calculated as

$$E_i = N_i \hbar \omega_i = 1.6\,\mathrm{fJ}, \tag{F.7}$$

and

$$P_i = E_i f_R = 1.6\,\mathrm{pW}, \tag{F.8}$$

where ω_i is the idler angular frequency and $f_R = 1\,\mathrm{kHz}$ is the frequency repetition rate of the pulsed pump laser. These are the values shown in Ref. [51].

APPENDIX **G**

FOURIER TRANSFORM ANALYSIS OF THE SIGNAL MEASURED IN FD-OCT

Here we explain in detail how to obtain the Fourier transform of the spectrum measured as a function of the wavelength of the signal beam, $S(\lambda)$. Figure G.1 depicts the step-by-step procedure.

Figure G.1(a) shows the spectrum $S(\lambda)$ measured with a spectrometer sensitive in the visible range. The spectrum is rewritten as function of the wavenumber $k = 2\pi/\lambda$. Considering the Jacobian of the transformation, the k-spectrum $S(k)$ is

$$S(k) = \frac{2\pi}{k^2} S(\lambda). \tag{G.1}$$

The spectrum is re-sampled to obtain a function $S(k)$ with equally-spaced k-values [Fig. G.1(b)]. The Fourier transform of the re-sampled spectrum is calculated as

$$\mathcal{F}[S(k)] = \int dk S(k) \exp(ikz). \tag{G.2}$$

This result is shown as a function of the axial position z in Fig.

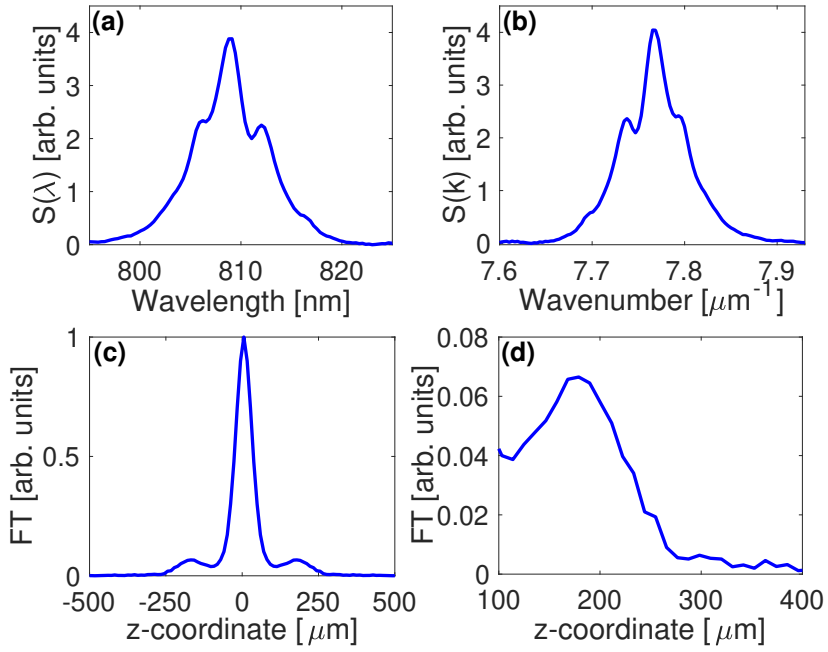

Figure G.1: Step-by-step procedure to obtain the depth profile of the OCT sample. **(a)** Spectrum measured with a visible spectrometer, $S(\lambda)$. **(b)** Spectrum re-sampled to wavenumbers, $S(k)$. **(c)** Fourier transform of the re-sampled spectrum. **(d)** Zoom of the Fourier transform showing the peak at a positive value of the z-coordinate.

G.1(c). Finally, we show a zoom of the FT showing only the peak of the FT at the positive value of the z-coordinate [Fig. G.1(d)].

APPENDIX **H**

THE SHAPE OF THE SIGNAL SPECTRUM AND ITS FOURIER TRANSFORM

In this Appendix we explain why the Fourier transform of the spectrum of the signal beam shown in Fig. 4.5 of the main text shows three peaks, and why the distance between peaks located at $z \neq 0$ is $2n_g d$, twice the optical length of the sample.

Let us define t as the distance from the first layer of the sample to the z-position with zero path length difference ($z_s = z_i$). If $t = 0$ the position of the first layer is such that $\Delta z_1 = 0$. If $t = n_g d$, the position of the second layer fulfills $\Delta z_2 = 0$. If $t < 0$ the position of zero path length difference is located before the first layer of the sample, and if $t > n_g d$ the position of zero path length difference is located beyond the second layer of the sample.

We assume that the shape of the spectrum in the low and high parametric gain regimes is qualitatively similar, while in the low parametric gain regime one can obtain useful analytical expressions of the spectrum $S(k)$ as a function of the wavenumber $k = \Omega/c$. The spec-

The shape of the signal spectrum and its Fourier transform

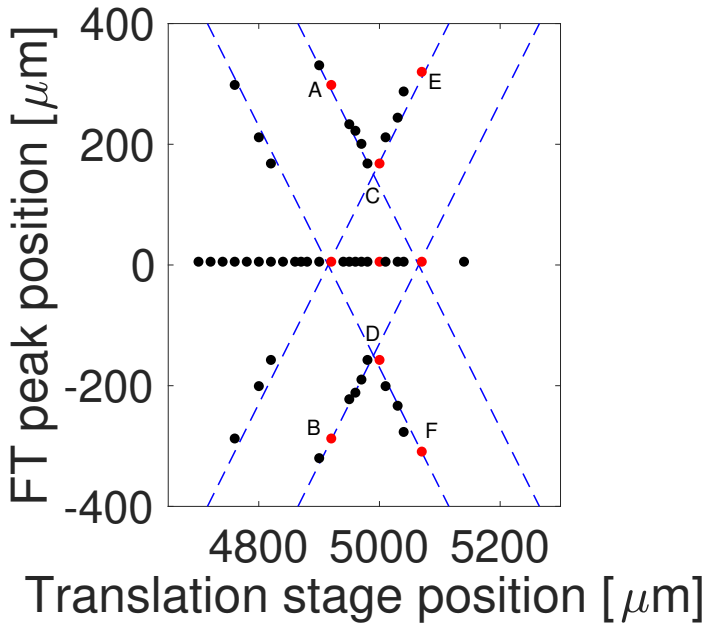

Figure H.1: Position of the peaks of the Fourier transform of the spectrum of the signal beam as a function of the position of the translation stage. Black dots represent experimental points. The dashed blue lines are theoretical lines based on Eq. (H.1) that best fit the experimental data. In this way, we can determine to which value of t corresponds each position of the translation stage. Points of interest are indicated as *A, B, C, D, E* and *F*, highlighted in red.

trum is

$$S(k) = 2\left|V_s(k)\right|^2 \{1 + r_1 \cos\left[\varphi_1 + k\left(cDL + 2t\right)\right] + r_2 \cos\left[\varphi_2 + k\left(cDL + 2t - 2n_g d\right)\right]\}. \tag{H.1}$$

The reflectivities of the first and second layers of the sample are $r_{1,2}$, $D = D_s - D_i$ where $D_{s,i}$ are inverse group velocities at the signal and idler central frequencies, n_g is the group index of the sample and $\varphi_{1,2}$

are constant phases given by

$$\varphi_1 = \frac{\omega_s}{c} n_s L + \frac{\omega_i}{c} n_i L + 2\frac{\omega_s}{c} z_s + 2\frac{\omega_i}{c} z_i,$$
$$\varphi_2 = \varphi_1 + 2\frac{\omega_i}{c}\, n_0 d. \tag{H.2}$$

L is the length of the nonlinear crystal, n_0 is the refractive index of the sample, z_s is the distance from the nonlinear crystal to the reference mirror located in the signal arm and z_i is the distance from the crystal to the first layer of the sample.

Let us first neglect the effect of the axial resolution for unveiling all peaks of the FT. The first term in Eq. (H.1) will produce a peak of the FT at $z = 0$. The second term would generate two symmetric peaks at $2t + cDL$ and $-2t - cDL$. Finally the third term would generate peaks at $2t+cDL-2n_g d$ and $-2t-cDL+2n_g d$. We show in Fig. H.1 the location of these peaks (dashed lines) and the positions of peaks obtained experimentally (dots). For $t < -cDL/2$ or $t > n_g d - cDL/2$, there will be always five FT peaks and the distance between the two peaks peaks at $z > 0$, or $z < 0$, will be $2n_g d$. If one now considers the effect of the axial resolution for distinguishing the FT peaks, the ideal scenario for OCT is $t \ll -cDL/2$ or $t \gg n_g d - cDL/2$. Unfortunately the sensitivity of the spectrometer used in our experiments impedes us to work in this regime and the axial resolution (~ 60 μm) makes the observation of the FT peaks close to the central peak troublesome.

However, for $-cDL/2 < t < n_g d - cDL/2$ we still can determine the distance between layers. In this scenario the number of FT peaks and the distance between them might change. We focus on three cases that correspond to three values of t where only two FT peaks at $z \neq 0$ are expected. In Fig. H.1 these points are the ones where the theoretical lines intersect. The first case is for $t = -cDL/2$ (points A and B) and the separation between these peaks is $4n_g d$. The second case is for $t = n_g d - cDL/2$ (points E and F) and the separation between the peaks is the same. Figure 4.5 of the main text corresponds to the third case, that is $t = (n_g L - cDL)/2$ (points C and D). The separation between these peaks is $2n_g d$.

The shape of the signal spectrum and its Fourier transform

APPENDIX I

ERROR PROPAGATION FOR VISIBILITY VS LOSSES CURVE

Error propagation is used to create the error bars displayed in Fig. 4.3 for the measured visibility of the interference fringes and for the idler reflectivity values. The flux rate of signal photons N_s, with variance $\sigma^2_{N_s}$, is the quantity used to calculate visibility by its definition

$$V = \frac{N_s^{max} - N_s^{min}}{N_s^{max} + N_s^{min}}. \tag{I.1}$$

Thus, the error of the visibility can be derived from the variance of the measured flux rates as

$$\sigma_V^2 = \left|\frac{\partial V}{\partial N_s^{max}}\right|^2 \sigma^2_{N_s^{max}} + \left|\frac{\partial V}{\partial N_s^{min}}\right|^2 \sigma^2_{N_s^{min}}. \tag{I.2}$$

If we calculate the partial derivatives, we obtain

$$\sigma_V^2 = \frac{4}{(N_s^{max} + N_s^{min})^4}\left\{\left[N_s^{min}\right]^2 \sigma^2_{N_s^{max}} + \left[N_s^{max}\right]^2 \sigma^2_{N_s^{min}}\right\}. \tag{I.3}$$

Error propagation for Visibility vs losses curve

The idler reflectivity r_i is varied with a gradual density filter and is measured as

$$r_i = \frac{I}{I_{max}}, \tag{I.4}$$

with I being the idler intensity for a concrete position of the density filter and I_{max} is the idler intensity for the maximum transmission of the density filter. The error of the reflectivity can be derived from the variance of both measured quantities as

$$\sigma_{r_i}^2 = \left|\frac{\partial r_i}{\partial I}\right|^2 \sigma_I^2 + \left|\frac{\partial r_i}{\partial I_{max}}\right|^2 \sigma_{I_{max}}^2. \tag{I.5}$$

If we calculate the partial derivatives, we obtain

$$\sigma_{r_i}^2 = \frac{\sigma_I^2}{I_{max}^2} + \left(\frac{I}{I_{max}^2}\right)^2 \sigma_{I_{max}}^2. \tag{I.6}$$

BIBLIOGRAPHY

[1] A. A. Michelson and E. W. Morley, "On the relative motion of the earth and the luminiferous ether," *American Journal of Science* ***34***, p. 333, 1887.

[2] D. Huang, E. A. Swanson, C. P. Lin, J. S. Schuman, W. G. Stinson, W. Chang, M. R. Hee, T. Flotte, K. Gregory, C. A. Puliafito, and J. G. Fujimoto, "Optical coherence tomography," *Science* ***254***, p. 1178, 1991.

[3] T. Dresel, G. Häusler, and H. Venzke, "Three-dimensional sensing of rough surfaces by coherence radar," *Appl. Opt.* ***31***, p. 919, 1992.

[4] W. Drexler and J. G. Fujimoto, *Optical Coherence Tomography: Technology and Applications*. Springer, Biological and Medical Physics series, 2008.

[5] D. C. Adler, J. Stenger, I. Gorczynska, H. Lie, T. Hensick, R. Spronk, S. Wolohojiana, N. Khandekar, J. Y. Jiang, S. Barry, A. E. Cable, R. Huber, and J. G. Fujimoto, "Comparison of three-dimensional optical coherence tomography and high resolution photography for art conservation studies," *Opt. Express* ***15***, p. 15972, 2007.

[6] H. Liang, B. Peric, M. Hughes, A. Podoleanu, M. Spring, and D. Saunders, "Optical coherence tomography for art conservation and archaeology," *Proc. SPIE* ***6618***, p. 661805, 2007.

[7] M. V. Chekhova and Z. Y. Ou, "Nonlinear interferometers in quantum optics," *Adv. Opt. Photonics* ***8***, p. 104, 2016.

[8] B. Yurke, S. L. McCall, and J. R. Klauder, "SU(2) and SU(1,1) interferometers," *Phys. Rev. A* ***33***, p. 4033, 1986.

[9] X. Y. Zou, L. J. Wang, and L. Mandel, "Induced coherence and indistinguishability in optical interference," *Phys. Rev. Lett.* ***67***, p. 318, 1991.

[10] G. B. Lemos, V. Borish, G. D. Cole, S. Ramelow, R. Lapkiewicz, and A. Zeilinger, "Quantum imaging with undetected photons," *Nature* ***512***, p. 409, 2014.

[11] A. C. Cardoso, L. P. Berruezo, D. F. Avila, G. B. Lemos, W. M. Pimenta, C. H. Monken, P. L. Saldanha, and S. Padua, "Clasical imaging with undetected light," *Phys. Rev. A* ***97***, p. 033827, 2018.

[12] M. Gilaberte Basset, A. Hochrainer, S. Töpfer, F. Riexinger, P. Bickert, J. R. León-Torres, F. Steinlechner, and M. Gräfe, "Video-rate imaging with undetected photons," *Laser Photonics Rev.* ***15***, p. 2000327, 2021.

[13] S. Töpfer, M. Gilaberte Basset, J. Fuenzalida, F. Steinlechner, J. P. Torres, and M. Gräfe, "Quantum holography with undetected light," *Science Advances* ***8***, p. eabl4301, 2022.

[14] M. Kutas, B. Haase, P. Bickert, F. Riexinger, D. Molter, and G. von Freymann, "Terahertz quantum sensing," *Sci. Adv.* ***6***, p. EAAZ8065, 2020.

Bibliography

[15] D. A. Kalashnikov, A. V. Paterova, S. P. Kulik, and L. A. Krivitsky, "Infrared spectroscopy with visible light," *Nature Photonics* ***10***, p. 98, 2016.

[16] A. V. Paterova, H. Yang, D. Kalashnikov, and L. A. Krivitsky, "Measurement of infrared optical constants with visible photons," *New J. Phys.* ***20***, p. 043015, 2018.

[17] I. Kviatkovsky, H. M. Chrzanowski, E. G. Avery, H. Bartolomaeus, and S. Ramelow, "Microscopy with undetected photons in the mid-infrared," *Sci. Adv.* ***6***, p. 42, 2020.

[18] A. V. Paterova, M. M. Sivakumar, H. Yang, G. Grenci, and L. A. Krivitsky, "Hyperspectral infrared microscopy with visible light," *Sci. Adv.* ***6***, p. 44, 2020.

[19] J. Shapiro, D. Venkatraman, and F. Wong, "Classical imaging with undetected photons," *Sci. Rep.* ***5***, p. 10329, 2015.

[20] M. Lahiri, A. Hochrainer, R. Lapkiewicz, G. B. Lemos, and A. Zeilinger, "Nonclassicality of induced coherence without induced emission," *Phys. Rev. A* ***100***, p. 053839, 2019.

[21] R. K. Chang, J. Ducuing, and N. Bloembergen, "Relative phase measurement between fundamental and second-harmonic light," *Phys. Rev. Lett.* ***15***, p. 6, 1965.

[22] X. Y. Zou, T. P. Grayson, and L. Mandel, "Observation of quantum interference effects in the frequency domain," *Phys. Rev. Lett.* ***69***, p. 3041, 1992.

[23] D. N. Klyshko, *Photons and Nonlinear Optics.* Gordon and Brech, 1988.

[24] D. N. Klyshko, "Combined EPR and two-slit experiments: interference of advanced waves," *Phys. Rev. Lett. A* ***132***, p. 299, 1988.

[25] J. Jing, C. Liu, Z. Zhou, Z. Y. Ou, and W. Zhang, "Realization of a nonlinear interferometer with parametric amplifiers," *Appl. Phys. Lett.* ***99***, p. 011110, 2011.

[26] F. Hudelist, J. Kong, C. Liu, J. Jing, Z. Y. Ou, and W. Zhang, "Quantum metrology with parametric amplifier-based photon correlation interferometers," *Nat. Commun.* ***5***, p. 3049, 2014.

[27] R. J. Glauber, "The quantum theory of optical coherence," *Phys. Rev.* ***130***, p. 2529, 1963.

[28] A. V. Belinsky and D. N. Klyshko, "Interference of classical and non-classical light," *Phys. Lett. A* ***166***, p. 303, 1992.

[29] H. M. Wiseman and K. Mølmer, "Induced coherence with and without induced emission," *Phys. Lett. A* ***270***, p. 245, 2000.

[30] A. Yariv, "Catching the wave," *IEEE Journal on Selected Topics in Quantum Electronics* ***6***, p. 1478, 2000.

[31] W. H. Louisell, A. Yariv, and A. E. Siegman, "Quantum fluctuations and noise in parametric processes," *Phys. Rev.* ***124***, p. 1646, 1961.

[32] D. N. Klyshko, "Coherent photon decay in a nonlinear medium," *JETP Letters* ***6***, p. 23, 1967.

[33] S. E. Harris, M. K. Oshman, and R. L. Byer, "Observation of tunable optical parametric fluorescence," *Phys. Rev. Lett.* ***18***, p. 732, 1967.

[34] D. Magde and H. Mahr, "Study in ammonium dihydrogen phosphate of spontaneous parametric interaction tunable from 4400 to 16 000 å," *Phys. Rev. Lett.* ***18***, p. 905, 1967.

[35] S. A. Akhmanov, V. V. Fadeev, R. V. Khokhlov, and O. N. Chunaev, "Quantum noise in parametric light amplifiers," *JETP Letters* ***6***, p. 85, 1967.

Bibliography

[36] J. P. Torres, K. Banaszek, and I. A. Walmsley, "Engineering nonlinear optic sources of photonic entanglement," *Prog. Optics* ***56***, p. 227, 2011.

[37] R. Boyd, *Nonlinear Optics*. Elsevier Science, 2008.

[38] N. Bloembergen, *Nonlinear Optics*. Singapore: World Scientific Publishing Company, 1964.

[39] R. Loudon, *The quantum theory of light (3rd ed.)*. Oxford University Press, 2000.

[40] B. Dayan, "Theory of two-photon interactions with broadband down-converted light and entangled photons," *Phys. Rev. A* ***76***, p. 043813, 2007.

[41] P. Navez, E. Brambilla, A. Gatti, and A. Lugiato, "Spatial entanglement of twin quantum images," *Phys. Rev. A* ***65***, p. 013813, 2001.

[42] E. Brambilla, A. Gatti, M. Bache, and A. Lugiato, "Simultaneous near-field and far-field spatial quantum correlations in the high-gain regime of parametric down-conversion," *Phys. Rev. A* ***69***, p. 023802, 2004.

[43] T. S. Iskhakov, A. M. Perez, K. Y. Spasibko, M. V. Chekhova, and G. Leuchs, "Superbunched bright squeezed vacuum state," *Opt. Lett.* ***37***, p. 1919, 2012.

[44] W. Wasilewski, A. I. Lvovsky, K. Banaszek, and C. Radzewicz, "Pulsed squeezed light: Simultaneous squeezing of multiple modes," *Phys. Rev. A* ***73***, p. 063819, 2006.

[45] P. Sharapova, A. M. Pérez, O. V. Tikhonova, and M. V. Chekhova, "Schmidt modes in the angular spectrum of bright squeezed vacuum," *Phys. Rev. A* ***91***, p. 043816, 2015.

[46] B. Dayan, A. Pe'er, A. A. Friesem, and Y. Silberberg, "Nonlinear interactions with an ultrahigh flux of broadband entangled photons," *Phys. Rev. Lett.* ***94***, p. 043602, 2005.

[47] K. Y. Spasibko, T. S. Iskhakov, and M. V. Chekhova, "Spectral properties of high-gain parametric down-conversion," *Opt. Express* ***20***, p. 7507, 2012.

[48] G. Frascella, E. E. Mikhailov, N. Takanashi, R. V. Zakharov, O. V. Tikhonova, and M. V. Chekhova, "Wide-field SU(1,1) interferometer," *Optica* ***6***, p. 1233, 2019.

[49] H. A. Haus, *Electromagnetic Noise and Quantum Optical Measurements*. Springer-Verlag, Berlin, 2000.

[50] R. W. Boyd, G. S. Agarwal, K. W. C. Chan, A. K. Jha, and M. N. Sullivan, "Propagation of quantum states of light through absorbing and amplifying media," *Opt. Commun.* ***281***, p. 3732, 2008.

[51] G. J. Machado, G. Frascella, J. P. Torres, and M. V. Chekhova, "Optical coherence tomography with a nonlinear interferometer in the high parametric gain regime," *Appl. Phys. Lett.* ***117***, p. 094002, 2020.

[52] A. V. Belinsky and D. N. Klyshko, "Interference of classical and non-classical light," *Phys. Lett. A* ***166***, p. 303, 1992.

[53] J. Rehacek and J. Perina, "Quantum statistics of two parametric processes with aligned idler beams," *Opt. Commun.* ***132***, p. 549, 1996.

[54] A. Luis and J. Perina, "SU(2) coherent states in parametric down-conversion," *Phys. Rev. A* ***53***, p. 1886, 1996.

[55] C. Simon and D. Bouwmeester, "Theory of an entanglement laser," *Phys. Rev. Lett.* ***91***, p. 053601, 2003.

Bibliography

[56] A. Vallés, G. Jiménez, L. J. Salazar-Serrano, and J. P. Torres, "Optical sectioning in induced coherence tomography with frequency-entangled photons," *Phys. Rev. A* ***97***, p. 023824, 2018.

[57] C. Akcay, P. Parrein, and J. P. Rolland, "Estimation of longitudinal resolution in optical coherence imaging," *Appl. Opt.* ***41***, p. 5256, 2002.

[58] A. Fercher, C. Hitzenberger, G. Kamp, and S. Elzaiat, "Measurement of intraocular distances by backscattering spectral interferometry," *Opt. Commun.* ***117***, p. 43, 1995.

[59] M. A. Choma, M. Sarunic, C. Yang, and J. Izatt, "Sensitivity advantage of swept source and fourier domain optical coherence tomography," *Opt. Express* ***11***, p. 2183, 2003.

[60] S. R. Chinn, E. A. Swanson, and J. G. Fujimoto, "Optical coherence tomography using a frequency tunable optical source," *Opt. Lett.* ***22***, p. 340, 1997.

[61] A. Rojas-Santana, G. J. Machado, M. V. Chekhova, D. Lopez-Mago, and J. P. Torres, "Analysis of the signal measured in spectral-domain optical coherence tomography based on nonlinear interferometers," *Phys. Rev. A* ***106***, p. 033702, 2022.

[62] A. Rojas-Santana, G. J. Machado, D. Lopez-Mago, and J. P. Torres, "Frequency-correlation requirements on the biphoton wave function in an induced-coherence experiment between separate sources," *Phys. Rev. A* ***102***, p. 053711, 2020.

[63] S. Parker, S. Bose, and M. B. Plenio, "Entanglement quantification and purification in continuous-variable systems," *Phys. Rev. A* ***61***, p. 032305, 2000.

[64] M. Hendrych, X. Shi, A. Valencia, and J. P. Torres, "Broadening the bandwidth of entangled photons: A step towards the

generation of extremely short biphotons," *Phys. Rev. A* ***79***, p. 023817, 2009.

[65] C. I. Osorio, A. Valencia, and J. P. Torres, "Spatiotemporal correlations in entangled photons generated by spontaneous parametric down conversion," *New J. Phys.* ***10***, p. 113012, 2008.

[66] K. Kitaeva, V. V. Kornienko, K. A. Kuznetsov, I. V. Pentin, K. V. Smirnov, and Y. B. Vakhtomin, "Direct detection of the idler thz radiation generated by spontaneous parametric down-conversion," *Opt. Lett.* ***44***, p. 1198, 2019.

[67] P. Abolghasem, M. Hendrych, X. Shi, J. P. Torres, and A. S. Helmy, "Bandwidth control of paired photons generated in monolithic bragg reflection waveguides," *Opt. Lett.* ***34***, p. 2000, 2009.

[68] A. Vanselow, P. Kaufmann, H. M. Chrzanowski, and S. Ramelow, "Ultra-broadband spdc for spectrally far separated photon pairs," *Opt. Lett.* ***44***, p. 4638, 2019.

[69] M. Kolobov, E. Giese, S. Lemieux, R. Fickler, and R. W. Boyd, "Controlling induced coherence for quantum imaging," *J. Opt.* ***19***, p. 054003, 2017.

[70] P. H. Souto Ribeiro, S. Padua, and C. H. Monken, "Image and coherence transfer in the stimulated down-conversion process," *Phys. Rev. A* ***60***, p. 5074, 1999.

[71] A. Vanselow, P. Kaufman, I. Zorin, B. Heise, H. M. Chrzanowski, and S. Ramelow, "Frequency-domain optical coherence tomography with undetected mid-infrared photons," *Optica* ***7***, p. 1729, 2020.

[72] M. V. Chekhova, S. Germanskiy, D. B. Horoshko, G. H. Kitaeva, M. I. Kolobov, G. Leuchs, C. R. Phillips, and P. A.

Prudkovskii, "Broadband bright twin beams and their upconversion," *Opt. Lett.* ***43***, p. 375, 2018.

[73] J. Le Gouet, D. Venkatraman, F. N. C. Wong, and J. H. Shapiro, "Classical low-coherence interferometry based on broadband parametric fluorescence and amplification," *Opt. Express* ***17***, p. 17874, 2009.

[74] X. Y. Zou, T. P. Grayson, and L. Mandel, "Observation of quantum interference effects in the frequency domain," *Phys. Rev. Lett.* ***69***, p. 3041, 1992.

[75] O. A. Ivanova, T. S. Iskhakov, A. N. Penin, and M. V. Chekhova, "Multiphoton correlations in parametric down-conversion and their measurement in the pulsed regime," *Quantum Electron.* ***36***, p. 951, 2006.

[76] A. Heuer, R. Menzel, and P. W. Milonni, "Complementarity in biphoton generation with stimulated or induced coherence," *Phys. Rev. A* ***92***, p. 033834, 2015.

[77] M. B. Nasr, B. E. A. Carrasco, S. Saleh, A. V. Sergienko, J. P. Torres, L. Torner, D. S. Hum, and M. M. Fejer, "Ultrabroadband biphotons generated via chirped quasi-phase-matched optical parametric down-conversion," *Phys. Rev. Lett.* ***100***, p. 183601, 2008.

[78] R. Tripathi, J. S. Nassif, N. Nelson, and J. F. Park, B. H. de Boer, "Spectral shaping for non-gaussian source spectra in optical coherence tomography," *Opt. Lett.* ***27***, p. 406, 2002.

[79] R. P. Feynman, R. B. Leighton and M. Sands, *The Feynman Lectures on Physics.* Addison-Wesley, Vol. 3, 1964.

[80] E. C. G. Sudarshan and T. Rothman, "Coherence and indistinguishability," *Opt. Lett.* ***16***, p. 1882, 1991.

[81] E. C. G. Sudarshan and T. Rothman, "The two-slit interferometer reexamined," *Am. J. Phys.* ***59***, p. 592, 1991.

[82] D. M. Greenberger and A. Yasin, "Simultaneous wave and particle knowledge in a neutron interferometer," *Phys. Lett.* ***128***, p. 391, 1988.

[83] G. Jaeger, A. Shimony, and L. Vaidman, "Two interferometric complementarities," *Phys. Rev. A* ***51***, p. 54, 1995.

[84] B. G. Englert, "Fringe visibility and which-way information: An inequality," *Phys. Rev. Lett.* ***77***, p. 2154, 1996.

[85] S. Durr, T. Nonn, and G. Rempe, "Origin of quantum-mechanical complementarity probed by a 'which-way' experiment," *Nature* ***395***, p. 33, 1998.

[86] S. Durr, T. Nonn, and G. Rempe, "Fringe visibility and which-way information in an atom interferometer," *Phys. Rev. Lett.* ***81***, p. 5705, 1998.

[87] S. Durr and G. Rempe, "Complementarity and quantum erasure in an atom interferometer," *Opt. Comm.* ***179***, p. 323, 2000.

[88] Y. H. Kim, R. Yu, S. P. Kulik, Y. Shih, and M. O. Scully, "Delayed choice quantum eraser," *Phys. Rev. Lett.* ***84***, p. 1, 2000.

[89] V. Balic, D. Brage, P. Kolchin, G. Y. Yin, and S. E. Harris, "Generation of paired photons with controllable waveforms," *Phys. Rev. Lett.* ***94***, p. 183601, 2005.

[90] E. Wolf and L. Mandel, *Optical Coherence and Quantum Optics*. Cambridge University Press, 1995.

[91] L. J. Wang, X. Y. Zou, and L. Mandel, "Induced coherence without induced emission," *Phys. Rev. A* ***44***, p. 4614, 1991.

Bibliography

[92] H. Rubinsztein-Dunlop *et al.*, "Roadmap on structured light," *Journal of Optics* ***19***, p. 013001, 2016.

[93] G. Molina-Terriza, J. P. Torres, and L. Torner, "Twisted photons," *Nature Physics* ***3***, p. 305, 2007.

[94] L. Allen, M. W. Beijersbergen, R. J. C. Spreeuw, and J. P. Woerdman, "Orbital angular momentum of light and the transformation of laguerre-gaussian laser modes," *Phys. Rev. A* ***45***, p. 8185, 1992.

[95] C. Rosales-Guzmán and A. Forbes, *How to Shape Light with Spatial Light Modulators*. SPIE Press, 2017.

[96] M. Mirhosseini, O. S. Magaña Loaiza, C. Chen, B. Rodenburg, M. Malik, and R. W. Boyd, "Rapid generation of light beams carrying orbital angular momentum," *Opt. Express* ***21***, p. 30196, 2013.

[97] M. Tsang, R. Nair, and X. M. Lu, "Quantum theory of superresolution for two incoherent optical point sources," *Phys. Rev. X* ***6***, p. 031033, 2016.

[98] V. Delaubert, N. Treps, M. Lassen, C. C. Harb, C. Fabre, P. K. Lam, and H. A. Bachor, "tem_{10} homodyne detection as an optimal small-displacement and tilt-measurement scheme," *Phys. Rev. A* ***74***, p. 053823, 2006.

[99] M. Paúr, B. Stoklasa, Z. Hradil, L. L. Sánchez-Soto, and J. Rehacek, "Achieving the ultimate optical resolution," *Optica* ***3***, p. 1144, 2016.

[100] L. Pezzè, M. A. Ciampini, N. Spagnolo, P. C. Humphreys, A. Datta, I. A. Walmsley, M. Barbieri, F. Sciarrino, and A. Smerzi, "Optimal measurements for simultaneous quantum estimation of multiple phases," *Phys. Rev. Lett.* ***119***, p. 130504, 2017.

[101] J. H. Eberly, "Schmidt analysis of pure-state entanglement," *Laser Phys.* ***16***, p. 921, 2006.

[102] A. Ekert and P. L. Knight, "Entangled quantum systems and the schmidt decomposition," *American Journal of Phys.* ***63***, p. 415, 1995.

[103] E. Pisanty, G. J. Machado, V. V. Hernández, A. Picón, A. Celi, J. P. Torres, and M. Lewenstein, "Knotting fractional-order knots with the polarization state of light," *Nature Photonics* ***13***, p. 569, 2019.

[104] C. K. Law and J. H. Eberly, "Analysis and interpretation of high transverse entanglement in optical parametric down-conversion," *Phys. Rev. Lett.* ***92***, p. 127903, 2004.

[105] L. Cisotto and H. P. Urbach, "Amplitude and phase beam shaping for highest sensitivity in sidewall angle detection," *J. Opt. Soc. Am. A* ***34***, p. 52, 2017.

[106] L. Cisotto, S. F. Pereira, and H. P. Urbach, "Analytical calculation on the determination of steep side wall angles from far field measurements," *J. Opt. 20* ***20***, p. 065601, 2018.

[107] S. Zuo, Z. Yan, Y. Feng, J. Ma, X. Jia, C. Xie, and K. Peng, "Quantum interferometer combining squeezing and parametric amplification," *Phys. Rev. Lett.* ***124***, p. 173602, 2020.

[108] W. Du, J. Kong, G. Bao, P. Yang, J. Jia, S. Ming, C.-H. Yuan, J. F. Chen, Z. Y. Ou, M. W. Mitchell, and W. Zhang, "SU(2)-in-SU(1,1) nested interferometer for high sensitivity, loss-tolerant quantum metrology," *Phys. Rev. Lett.* ***128***, p. 033601, 2022.